博　士　論　文

Fracture behaviors and design optimization of chopped carbon fiber tape reinforced thermoplastics structures

（炭素繊維テープ強化熱可塑性複合材料部材の破壊挙動と設計最適化）

郭　啓濤

Abstract

Carbon fiber reinforced plastics (CFRP) are increasingly used in the primary structural components of vehicles and aircraft due to exhibiting high specific moduli and strength. However, the applications of conventional continuous fiber composites are limited by the high manufacturing costs and complex shape formability issues of these materials. In contrast, discontinuous carbon fiber reinforced thermoplastics (DCFRTP) are well suited for high-cycle and complex shape molding, being viewed as favorable materials for mass-produced vehicles. Consequently, chopped carbon fiber tape reinforced thermoplastics, one kind of randomly oriented strands (ROS) composites, have recently attracted increased attention.

Complex-shaped structures (e.g., L-shaped or hat-shaped ones) are frequently encountered in aeronautical and automotive applications. The curved sections of these structures are considered to be their weakest points due to the out-of-plane stresses induced by external loadings. Therefore, with the emergence of ROS as structural materials of mass-produced automobiles, studies on delamination behavior in ROS should be conducted. Besides, hat-shaped hollow beam, one of the main frame structural members of automobiles, requires high stiffness for vehicle maneuverability and high energy absorption for collision safety. This work aims to characterize fracture behaviors and design optimization of complex structures made from ultra-thin chopped carbon fiber tape reinforced thermoplastics (UT-CTT).

The interlaminar fracture toughness and interlaminar tensile strength of UT-CTT were theoretically, experimentally and numerically determined. Double cantilever beam (DCB, mode I) and end notched flexure (ENF, mode II) were studied to experimentally determine the interlaminar fracture toughness, while interlaminar tensile strength was determined using L-shaped specimen under four-point bending test. Furthermore, numerical analysis utilizing the surface-based cohesive zone model based on the triangular traction–separation law was used to predict the delamination behavior in UT-CTT. The numerically predicted load-displacement curves showed good correlation with the theoretical and experimental results.

Comprehensive experiments and fracture simulation method were proposed to study fracture mechanisms characteristics of UT-CTT hat-shaped hollow beam under transverse static and

impact loadings. The numerical model was to incorporate some hypothetical inter-layers in UT-CTT and assign them with the failure model as cohesive zone model, which can perform non-linear characteristics with failure criterion for representing delamination failure. The dynamic material parameters for the impact model were theoretically predicted with consideration of strain-rate dependency. It shows that the proposed modelling approach for interacting damage modes can serve as a benchmark for modelling damage coupling in composite materials.

Strength-based optimization and lightweight optimization of complex structures under single flexural loading and multi-loadings were studied to show potential applications of UT-CTT for mass-produced vehicles by taking full advantage of the merit “thickness variation”.

Contents

List of Figures

List of Tables

List of Equations

List of Abbreviations

Abbreviations	Definition
Al	Aluminum
CFRP	Carbon fiber reinforced plastics
CFRTP	Carbon fiber reinforced thermoplastics
CFRTS	Carbon fiber reinforced thermosets
CLT	Classical laminate theory
CMT	Carbon fiber mat reinforced thermoplastics
CNTs	Carbon nanotubes
CO_2	Carbon dioxide
CP	Cross-ply
CTT	Chopped carbon fiber tape reinforced thermoplastics
CZM	Cohesive zone model
DCB	Double cantilever beam
DCFRTP	Discontinuous carbon fiber reinforced thermoplastics
ECZM	Element based cohesive zone model
ELS	End loaded split
ENF	End notched flexure
FEM	Finite element model
GFRP	Glass fiber reinforced polymer
ISVC	Interstrand void content
ONF	Over notched flexure
PA6	Polyamide 6
PEEK	Polyether ether ketone
PI	Polyimide
PP	Polypropylene
PPS	Polyphenylene sulfide
PTFE	Polytetrafluoroethylene
ROS	Randomly oriented strands
SHS	Square hollow section
TTSP	Time-temperature superposition principle
UD	Unidirectional
UT-CTT	Ultra-thin chopped carbon fiber tape reinforced thermoplastics
XFEM	Extended finite element method

1. Introduction

1.1 Motivation

Structures with complex shapes such as L-shaped and hat-shaped, which are frequently encountered in aerospace and automotive applications, are usually used as load assembly and contribute to high stiffness and crashworthiness ability of the whole airplanes or vehicles. The requirements of engineering design for such structures should not only provide the structural functions but also be lightest which helps greatly in increasing fuel economy, vehicle safety, vehicle dynamics and reducing CO2 emission. Several strategies for lightweight structures including the use of alternate lightweight materials, structural design optimization and new design as shown in Figure 1-1. Structural design optimization techniques designed to reduce the weight have also attempted to improve or obtain the optimized structures which are limited by constraints of costs, geometries, and structural performance, et al. New design for certain structures could achieve the most lightweight structures, however, the cost and time period is also the highest and longest comparing with other lightweight methods.

Composite materials that possess high specific strength properties have increasingly utilized in recent years. As shown in Figure 1-2 [1], the development of multi-material (including aluminum, steel, magnesium and carbon fiber reinforced polymer (CFRP)) spaceframe of Audi new A8 aiming to decrease weight, increase torsional rigidity, and offer greater performance, efficiency and safety, has shown the potential application of mass-production of composite material structures. As shown in Figure 1-3 [2], CFRTP automotive model can achieve 30% weight reduction compared with a conventional car for the part replacement case. In this case, Discontinuous CFRTP can be used for the panels and modules, while continuous CFRTP can be used for load bearing structures.

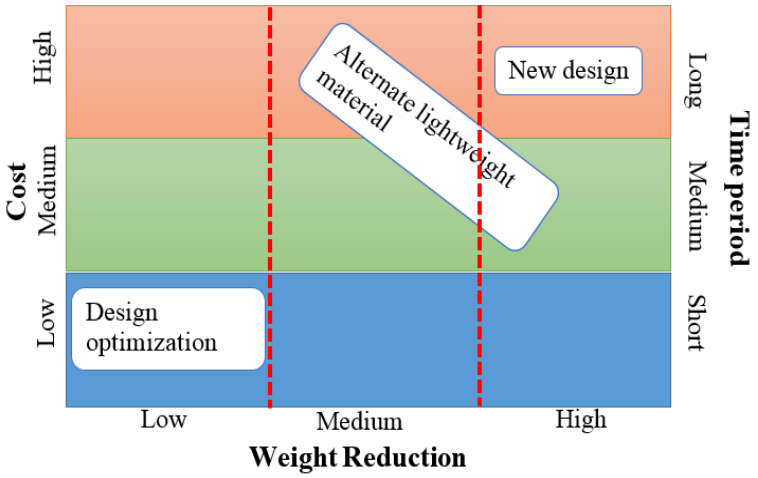

Figure 1-1 Strategies to lightweight vehicles

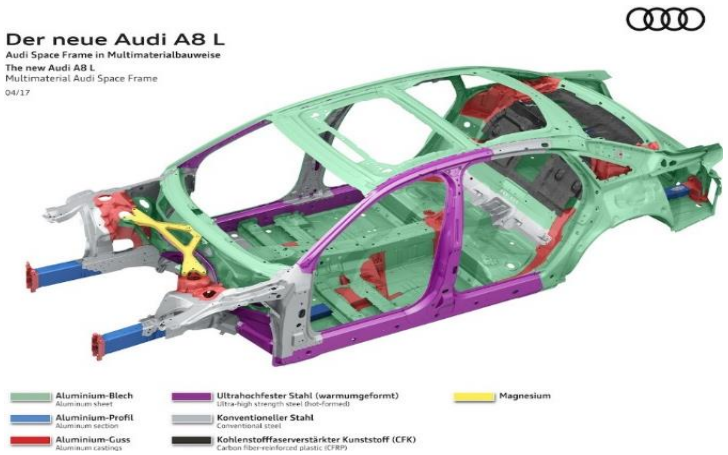

Figure 1-2 Multi-material application in Audi New A8 [1]

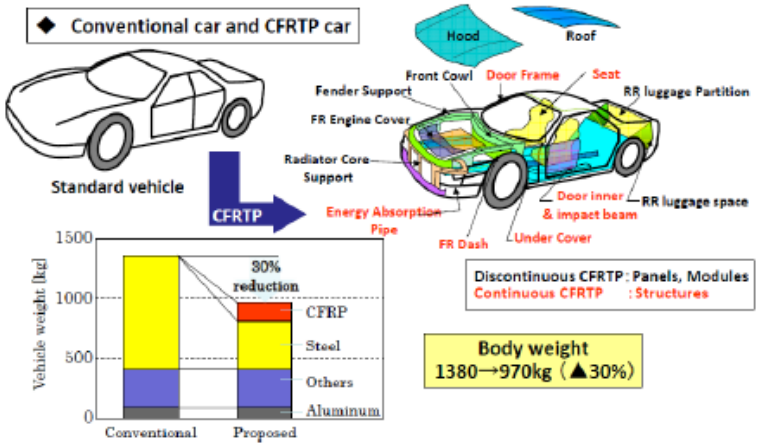

Figure 1-3 The lightweight CFRTP automotive model for the part replacement case [2]

1.2 Literature review

The subjective of this study is to investigate fracture behaviors and design optimization of chopped carbon fiber tape reinforced thermoplastics structures. Therefore, the literature review is split into three sections: development of CFRP, fracture behavior of CFRP and design optimization of CFRP structures.

1.2.1 Development of CFRP

High-tensile steel, aluminum alloy, and composite as new lightweight materials have been developed rapidly these days. As an effective way for weight reduction, application of composite material to mass production automotive bodies have been widely used.

A composite material consists of two or more different materials with different physical and/or chemical properties. The properties of a composite are mostly in contrast with the properties of the single components. A composite contains a reinforcement material which is surrounded by a matrix material. The matrix material supports the reinforcement and gives the composite its shape. Load subjected to the matrix is transferred to the reinforcement, of which purpose is to improve stiffness, strength and toughness of the composite. The mechanical properties of the composite are to a large extent depending on the configuration (the typology) of the reinforcement constituent. In a fibrous reinforcement, the aspect ratio of the fibers is an important factor. The aspect ratio is seen as the ratio between the length and the width of the cross-section of the fibers. If the composite contains long fibers with a high aspect ratio, it is classified as continuous, and if the fibers are short with low aspect ratios, it is defined as discontinuous. Another important factor is the orientations of the fibers; they can either be aligned or randomly oriented. For example, continuous aligned fibers can be unidirectional or bi-directional (woven). An illustration of different composite typologies is shown in Figure 1-4 [3].

As one kind of composite materials, carbon fiber reinforced plastics (CFRP) are increasingly used in primary structural components of automobiles and aircraft because of their high specific modulus and strength. There are two kinds of CFRP: Carbon fiber reinforced thermosetting resins (CFRTS) and Carbon fiber reinforced thermoplastics (CFRTP). Figure 1-5 [4] shows the comparison of specific flexural rigidity and specific tensile strength of typical structural materials.

Compared with metallic materials, CFRTS is excellent in both specific flexural rigidity and specific tensile strength, and CFRTP is excellent in specific flexural rigidity even if fiber volume fraction is small. Then, CFRTS is good at weight-lightening of strength members such as chassis and frame of automobile, pressure vessel, etc. On the other hand, CFRTP is good at weight-lightening of rigid members such as roof, wall and door of an automobile, etc. Considering that most of the weight of structures, except for pressure vessel and airplane, is the weight of rigid members, the technical development of CFRTP will contribute well to reduce structural weight drastically.

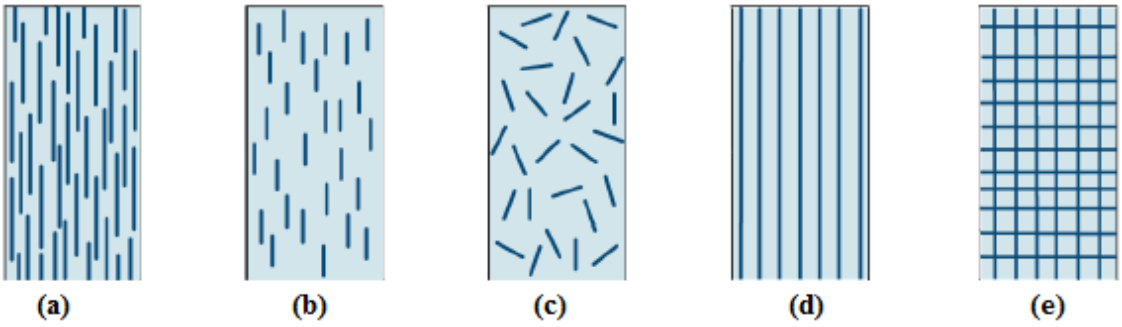

Figure 1-4 Fiber-reinforced materials types: (a) continuous aligned (b) discontinuous aligned (c) discontinuous random-oriented (d) continuous aligned, unidirectional (e) continuous aligned, woven [3]

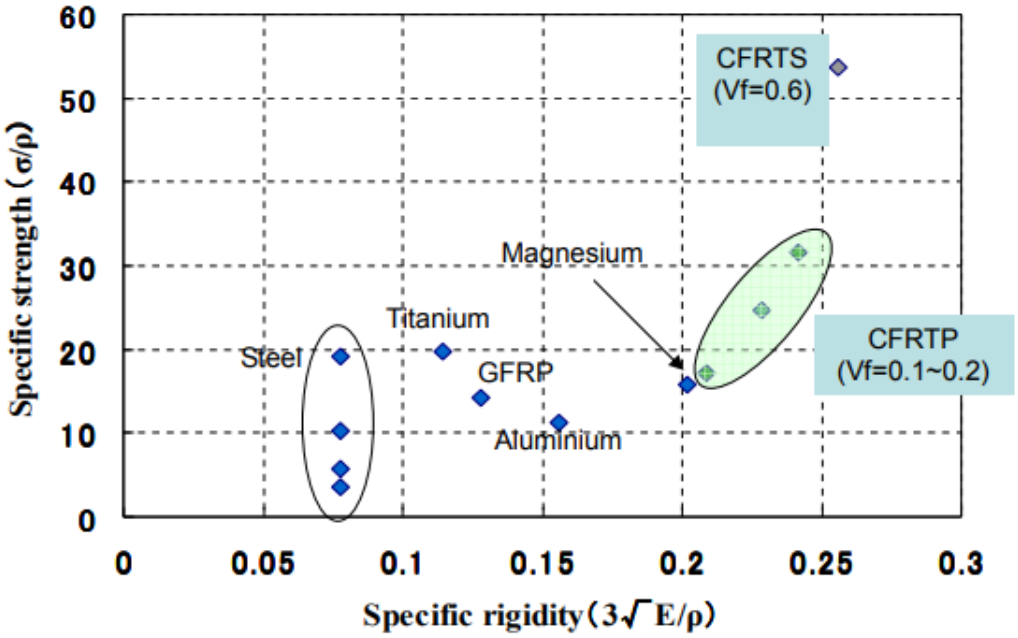

Figure 1-5 Specific flexural rigidity and specific tensile strength [4]

1. Introduction

It is well known that CFRTS are extensively used in many industrial areas, on account of their high specific modulus and strength. Different from traditional unidirectional CFRTS (UD-CFRTS), discontinuous CFRTS are the superiority of outstanding molding performance and flexible designability for complex structures. In recent decades, many researchers are engaged in reducing the weight of automobiles by using discontinuous CFRTS [5-8]. Comparing with CFRTS, significant advantages of short molding time, low processing cost and excellent recyclability make CFRTP attract many researchers and industrial engineers. However, the application of conventionally used continuous fiber composites in mass-produced devices has been limited by high manufacturing costs and their low formability to complex shapes. Discontinuous carbon fiber reinforced thermoplastics (DCFRTP) are considered to be more suitable for mass production automotive because of their relatively high applicability in high-cycle molding and complex-shape molding [9].

Several discontinuous fibers material systems are developed in recent years. Among them, randomly oriented strand (ROS) composites have been studied on the manufacturing process and the measurement of mechanical properties. Authors [10] introduced a 2D Finite Element model to predict the squeeze flow of ROS composites, in which Bingham fluid was used to represent the material, and an inverse method was used to determine the equivalent viscosity and yield stress of small, medium and large strand size. It showed that with the increase in strand length, the viscosity and yield stress also increase. As shown in Figure 1-6, the numerical simulation showed good agreement with experimental results in the case of Carbon/PEEK ROS samples. Ref. [11] described void formation during the manufacturing process of randomly oriented strand carbon/PEEK composites. Figure 1-7 and Figure 1-8 showed cross-sectional micrographs of the composites at different pressure and the effect of void contents on compressive strength. The results showed that the strength reduction may be caused by the high concentration of porosity near the surface. Ref. [12] developed a model to investigate the effect of the manufacturing process and material parameters on interstrand void content (ISVC) of ROS. The assumption of the model is that the gaps between strands can be filled due to the squeezing of every single strand.

Authors [13-16] conducted research on mechanical properties, numerical prediction of ROS in which the strands are unidirectional Carbon/ PEEK prepreg. The tensile, compressive, shear and

fatigue properties of ROS were measured by the standard experiments and several modelling methods for predicting damage evolution were discussed. The main achievements could be concluded as follows:

1) Tensile, compressive and shear properties (including modulus and strength) were highly dependent on the strand length (see in Figure 1-9), and tensile, compressive and shear strength had similar magnitudes which could be caused by the reason that loading-bearing mechanisms and fracture mechanics of ROS under these loadings are the same.

2) Two stochastic finite element techniques were established to estimate strength. The first method established the variability of the model based on the concept of ROS and investigated the strength prediction based on Hashin failure criteria and fracture energies; The second method predicted strands breakage based on classical laminate theory (CLT) and Hashin's criteria, and strands debonding was simulated using the interlaminar fracture model in which interlaminar strength and fracture toughness are used. The results show that the model matches the trends observed during experiments (see in Figure 1-10), which can be used to investigate the effect of strand size on mechanical properties and describe heterogeneous nature of ROS composites, and the ‘weakest-link’ principle results in lower strength of the material compared with that of continuous fiber laminates.

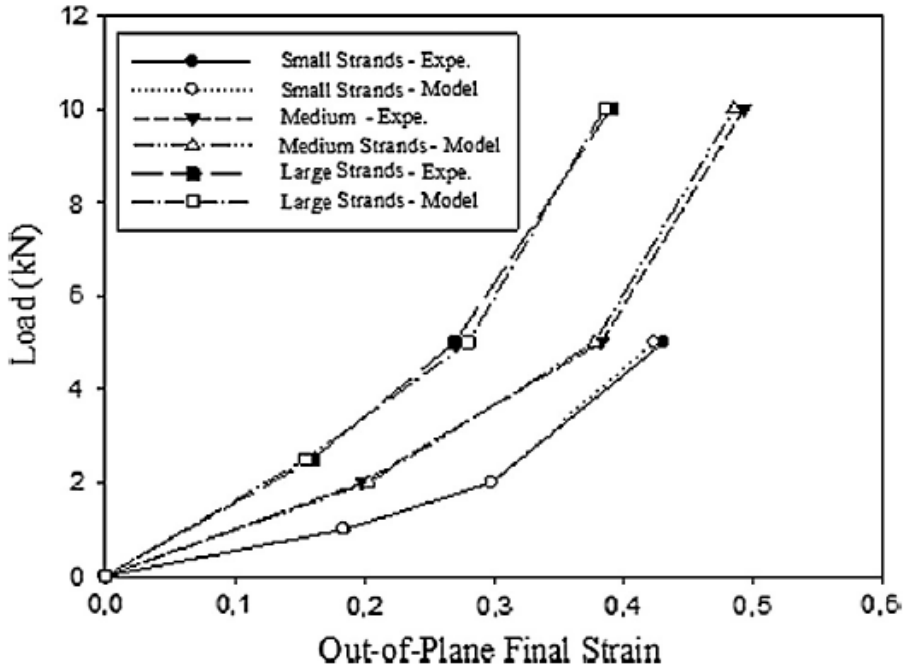

Figure 1-6 Load-strain curves of FEM and experiment [10]

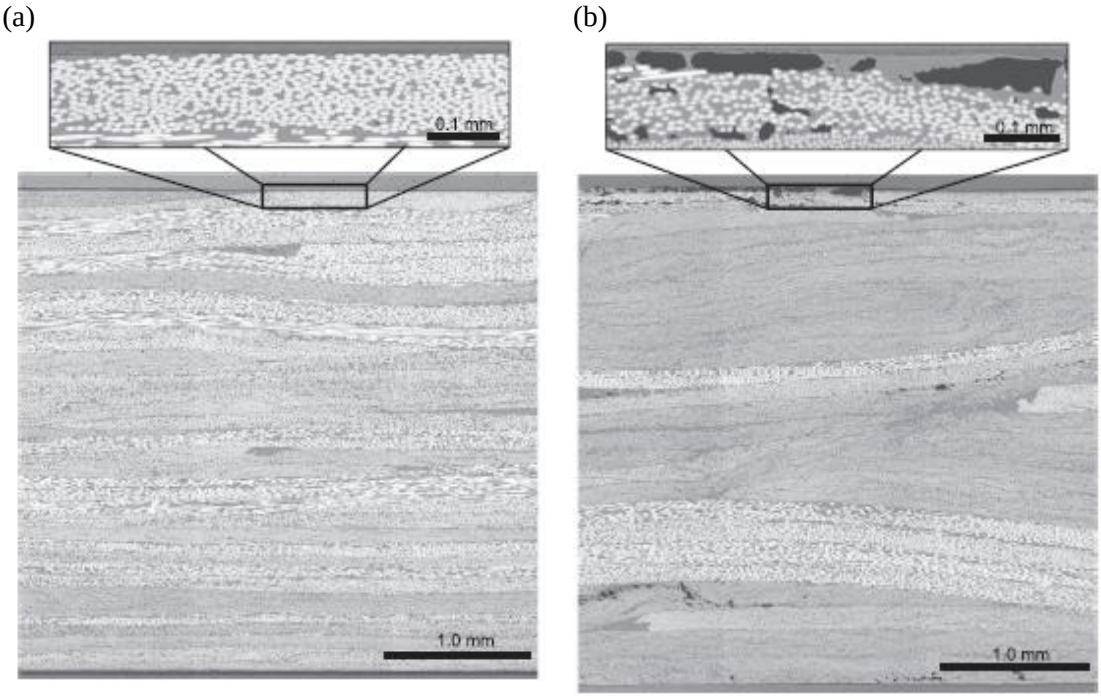

Figure 1-7 Representative cross-sectional micrographs of ROS composites cooled at different pressures: (a) 7 MPa– Case A (b) 1 MPa– Case B [11]

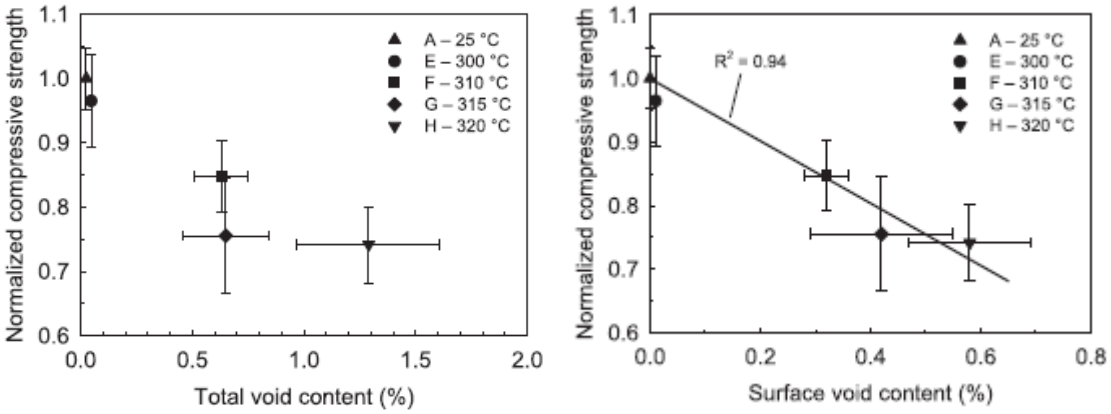

Figure 1-8 Relation between void content and normalized compressive strength [11]

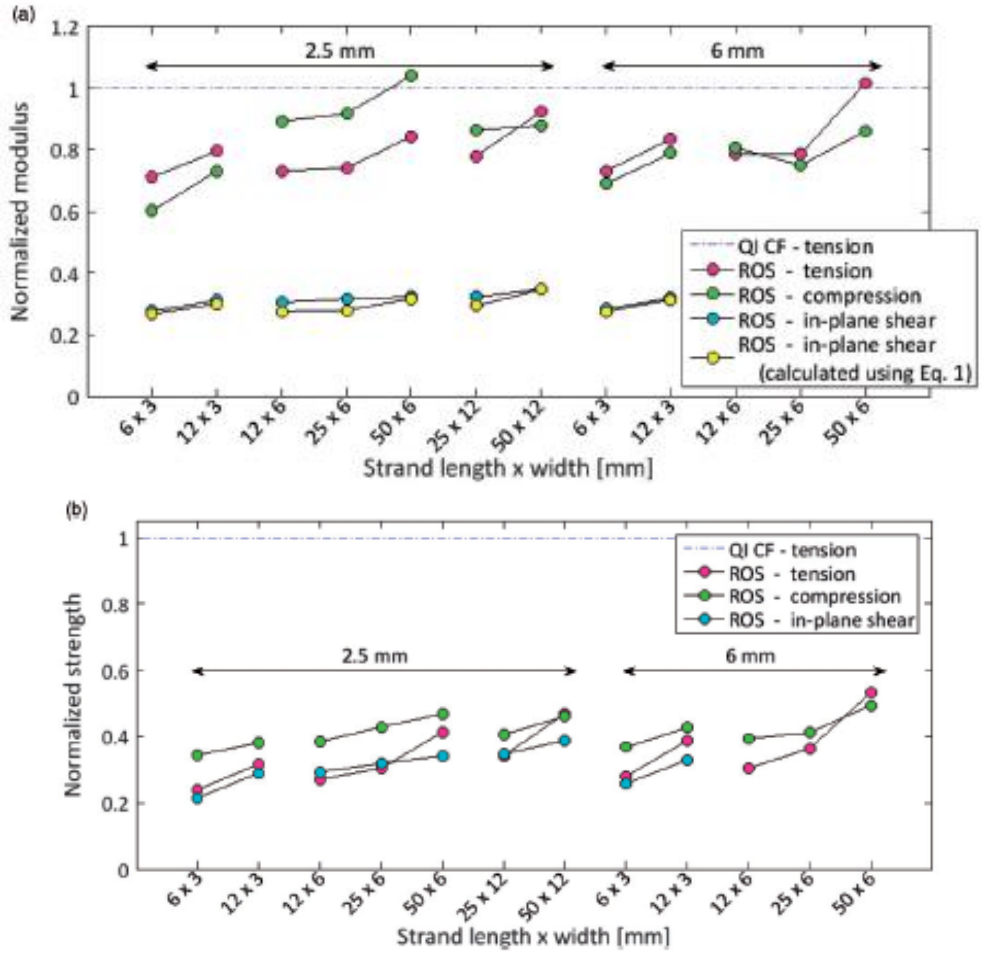

Figure 1-9 Effect of strand size on tensile, compressive and shear (a) modulus and (b) strength of ROS composites [13]

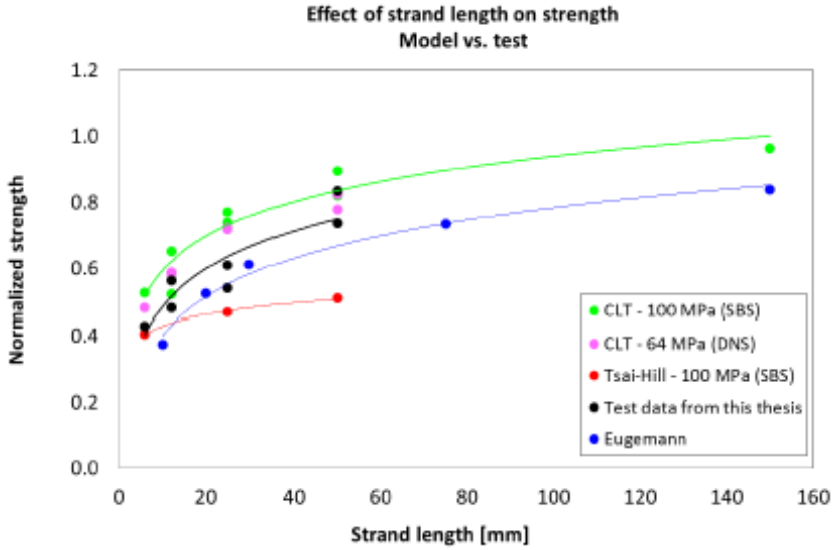

Figure 1-10 Comparison between two different FE modellings and experiments on effect of strand length on strength of ROS composites [16]

Also, some industrial applications of CFRTP have been found. As shown in Figure 1-11, Teijin built a 4 seated electric concept car with body structure constructed with chopped CFRTP fibers. The weight of this body is only 47 kilograms or roughly one fifth the weight of a conventional automobile body structure [17]. The fuel cell stack frame of the world's first fuel cell car "Toyota Mirai" (see in Figure 1-12) was manufactured using CFRTP [18]. The CFRTP is a combination of a thermoplastic matrix resin and a two-dimensional paper-like carbon fiber mat. Although the production rate of the stack frame is not as high as that of mass production automotive components of 100,000 units per year, the CFRTP developed by Toray and Toyota can realize about one-minute forming cycle resulting in the possibility of mass production in the future.

Figure 1-11 47 kg weight cell structure made by random chopped CFRTP [17]

Figure 1-12 CFRTP application in Toyota Mirai [18]

1.2.2 Fracture behavior of CFRP

1.2.2.1 Interlaminar behavior of CFRP

In industrial applications, automotive composite components are commonly designed only considering in-plane strength such as tensile or compressive strength. However, the differences of in- and out-of-plane strengths of these composites should be considered to avoid an unexpectedly low failure load of the curved section at small curvature radii because the failure of structures with curved shapes is mainly due to delamination resulting from the out-of-plane stresses.

There are three basic interlaminar fracture modes of the delamination process: mode I (opening mode), mode II (sliding mode) and mode III (tearing mode), illustrated in Figure 1-13. Considering about interlaminar fracture investigation, researches have focused on the measurement of interlaminar properties (including interlaminar fracture toughness and strength) and expression methods of interlaminar fracture behavior.

Contributions to interlaminar fracture toughness measurement have been made by a lot of researchers. I. D. Baere et al [19] experimentally investigated Mode I and Mode II interlaminar behavior of a 5-harness satin weave carbon fabric reinforced polyphenylene sulphide. An unstable crack propagation resulting in a saw-tooth like load-displacement curve in double cantilever beam (DCB) tests and stable crack propagation in end notched flexure (ENF) tests were observed as shown in Figure 1-14. Analytical methods based on linear elastic fracture mechanics and compliance-based beam methods were used to determine Mode I and Mode II critical energy release rate for both initiation and propagation. S. G. Ivanov et al [20] compared the interlaminar fracture toughness of textile composites in which the reinforcement is carbon fabric 5 harness satin and 3 different types of matrices PPS, PEEK, and PEEK+CNTs. Y. Ma et al [21] showed CF/PA6 laminates has high Mode II interlaminar fracture toughness, which means that the ability of CF/PA6 laminates to resist fracture is much better than CF/Epoxy laminates (see in Figure 1-15). Authors [22, 23] numerically and experimentally investigated the delamination behavior in the DCB and ENF specimen. It is noted that the plateau value of R-curve of non-zero interfaces is four times higher than the onset value in the DCB tests, and the value is almost the same as that of the zero interface, the reason of which could be explained by the deviation of the initial crack

from the original symmetrical crack plane as shown in Figure 1-16. Similarly, higher critical energy release rate of the non-zero interfaces was also caused by deviating from the symmetry plane for ENF specimen. W.X. Wang et al [24] described four kinds of test methods (Figure 1-17), including ENF test, ELS test, 4ENF test, and ONF test to measure the Mode II interlaminar fracture toughness, and the effect of friction between crack faces was also conducted. The less influence of friction in the 4ENF test evidenced that the 4ENF test is an effective experimental method to evaluate Mode II propagation interlaminar fracture toughness. Besides, the influence of loading rate, fiber orientation, fiber bridging and geometrical size on the interlaminar failure of woven composites and unidirectional composites have been investigated [25-30]. The studies showed that Mode I interlaminar fracture toughness will decrease with loading rate increasing. Fiber nesting leads to interlaminar fiber bridging, which can result in overestimation of the measured fracture energies. The specimen thickness showed the least efforts on interlaminar fracture toughness by using the corrected beam theory.

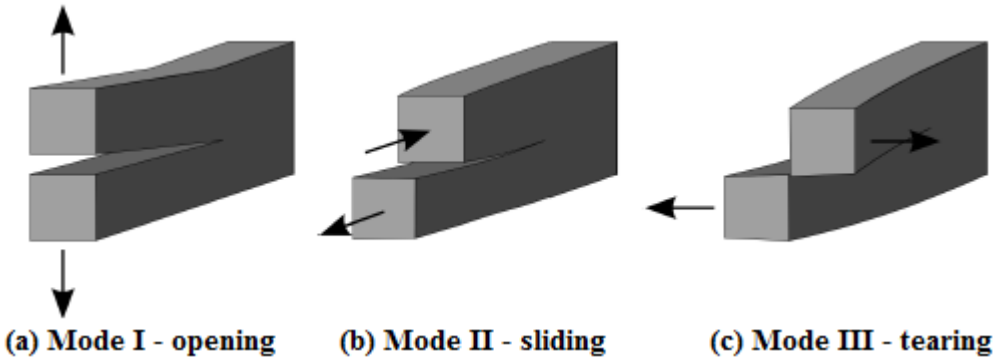

Figure 1-13 Types of interlaminar fracture modes

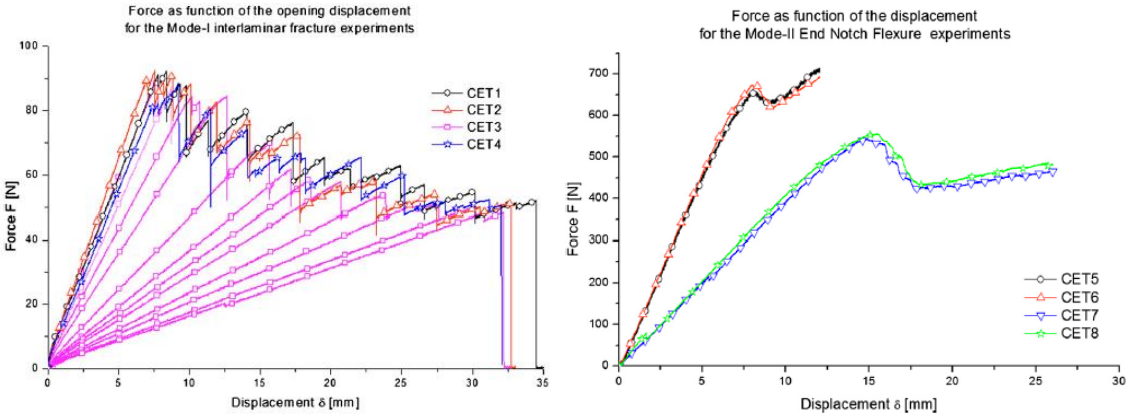

Figure 1-14 Load-displacement curves for DCB tests (left) and ENF tests (right) [19]

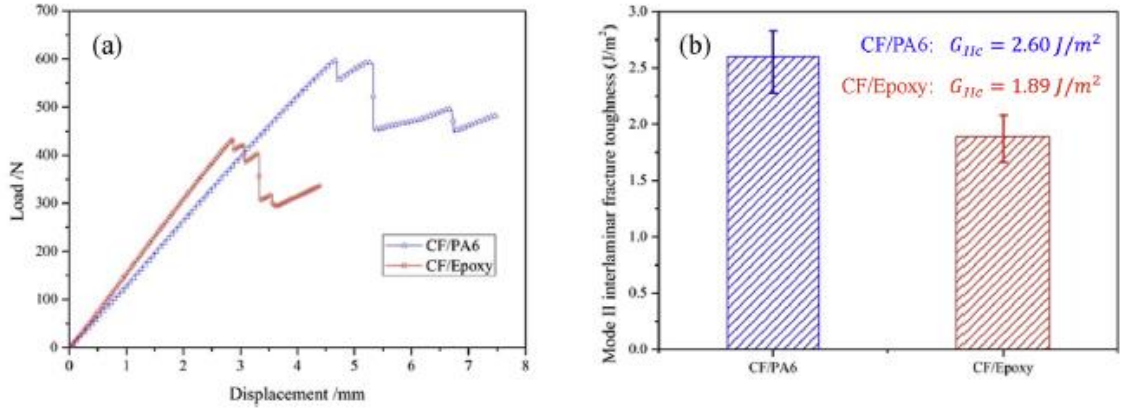

Figure 1-15 (a) Load-displacement curves and (b) Mode II interlaminar fracture toughness of CF/PA6 and CF/Epoxy [21]

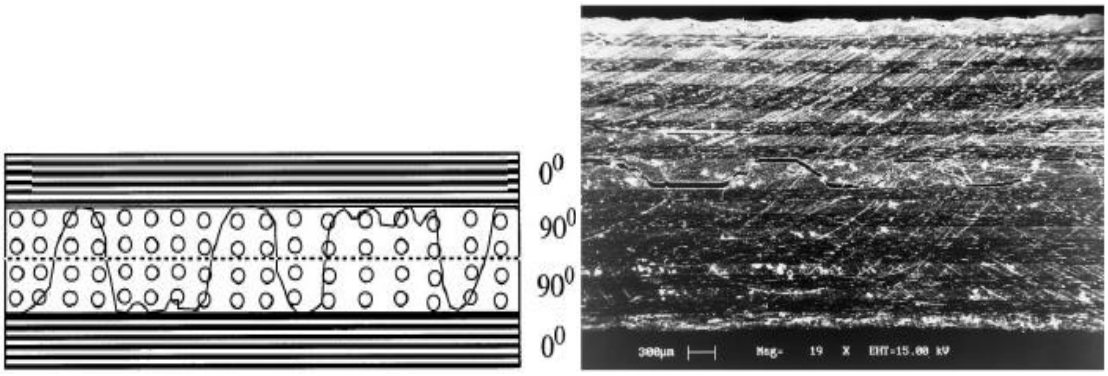

Figure 1-16 Crack growth at 90°/90°interface [22]

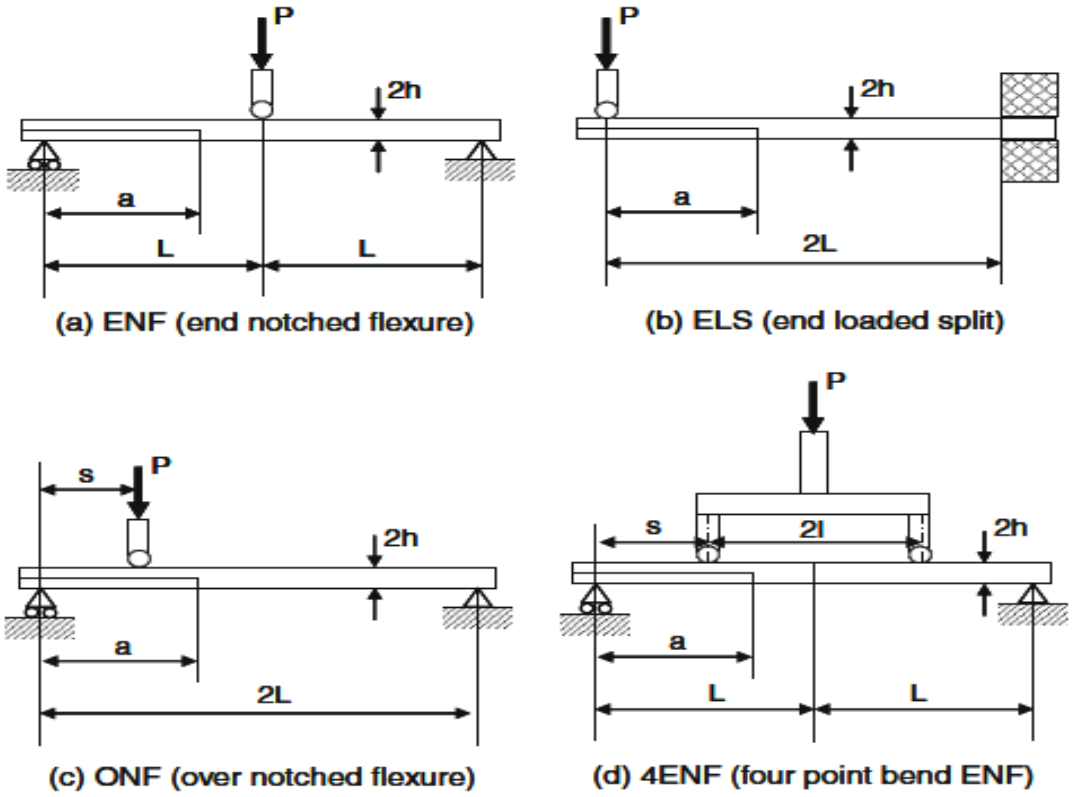

Figure 1-17 Test methods to measure the Mode II interlaminar fracture toughness [24]

Some researches considering about interlaminar strength determination of CFRP have been studied. G. Wimmer et al [31] noted that the load-displacement curve increases linearly until an abrupt drop appears as shown in Figure 1-18. The abrupt decrease in load indicates that unstable delamination occurs instantly, and then a second linear increase with a lower stiffness in the load-displacement curve can be observed after the crack stops growing. In other words, interlaminar failure causes a significant reduction in the load-carrying capacity, which attracts a lot of attention in the aerospace and automotive industries. Y. Wan et al [32] investigated the effect of curvature on the strength and damage modes of L-shaped structures using two different randomly oriented short fiber–reinforced polypropylenes, showing that tangential stress increased with increasing specimen radius, whereas interlaminar tensile stress showed an opposite trend as shown in Figure 1-19. T. Matsuo et al [33] proposed a modified theoretical method (shown in Figure 1-20, Equation 1-1and Equation 1-2) to analyze stress distribution in consideration of nonlinear geometric effects, demonstrating that thick specimens were prone to interlaminar fracture (see in Figure 1-21) whereas Raju et al [34] described the distributions of interlaminar tensile and shear stresses in composite top-hat stiffeners using experimental and numerical methods. Q. Liu et al

[35] showed that thickness is the most important parameter with consideration of the fracture behavior and energy absorption of double hat–shaped weave carbon fiber reinforced plastic tubes, and B.C. Jin et al [36] performed analytical and parametric studies of hat-stiffened composite panels, revealing that the height is an influential parameter.

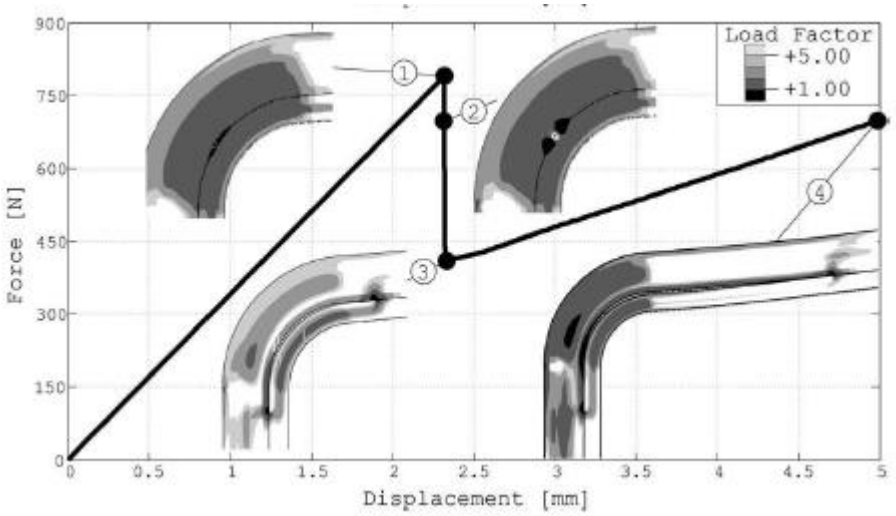

Figure 1-18 Predicted delamination process in the L-shaped laminate [31]

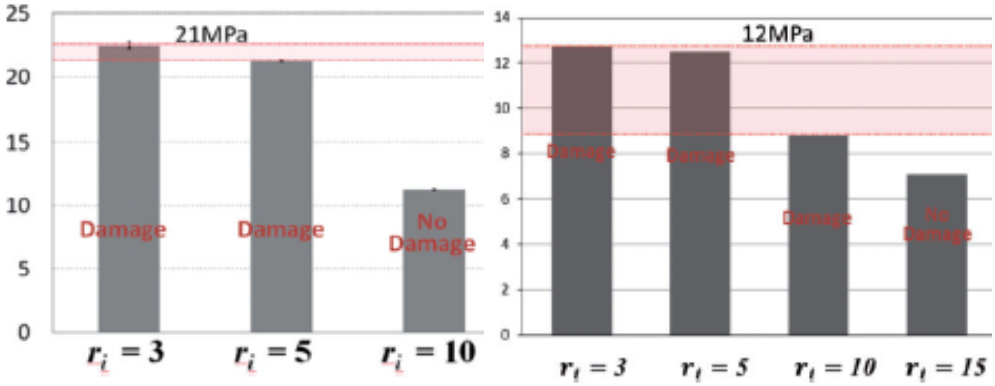

Figure 1-19 Interlaminar tensile strength of CMT (left) and CTT (right) [32]

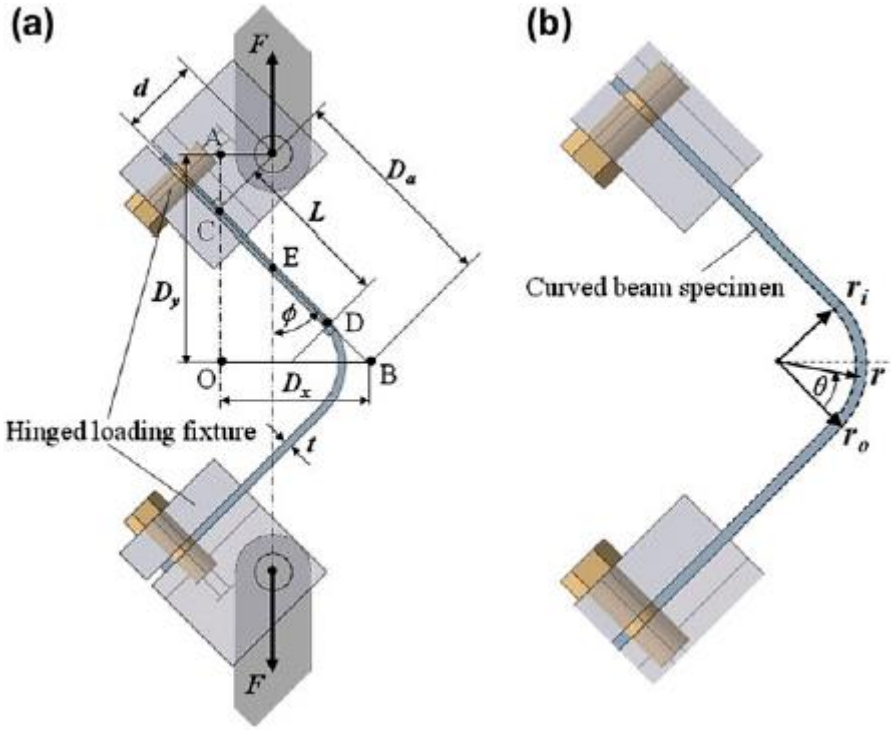

Figure 1-20 Experimental setup with parameters [33]

$$\sigma_r = -\frac{M_a}{r_0^2 * b * g_M}\left\{1-\frac{1-c^{k+1}}{1-c^{2k}}*\left(\frac{r}{r_0}\right)^{k-1}-\frac{1-c^{k-1}}{1-c^{2k}}*c^{k+1}*\left(\frac{r_0}{r}\right)^{k+1}\right\}+\frac{F}{b*g_F*r}\left\{\left(\frac{r}{r_0}\right)^{\beta}+c^{\beta}*\left(\frac{r_0}{r}\right)^{\beta}-1-c^{\beta}\right\}$$

Equation 1-1

$$\sigma_\theta = -\frac{M_a}{r_0^2 * b * g_M}\left\{1-\frac{1-c^{k+1}}{1-c^{2k}}*k*\left(\frac{r}{r_0}\right)^{k-1}+\frac{1-c^{k-1}}{1-c^{2k}}*k*c^{k+1}*\left(\frac{r_0}{r}\right)^{k+1}\right\}+\frac{F}{b*g_F*r}\left\{(1+\beta)*\left(\frac{r}{r_0}\right)^{\beta}+(1-\beta)*c^{\beta}*\left(\frac{r_0}{r}\right)^{\beta}-1-c^{\beta}\right\}$$

Equation 1-2

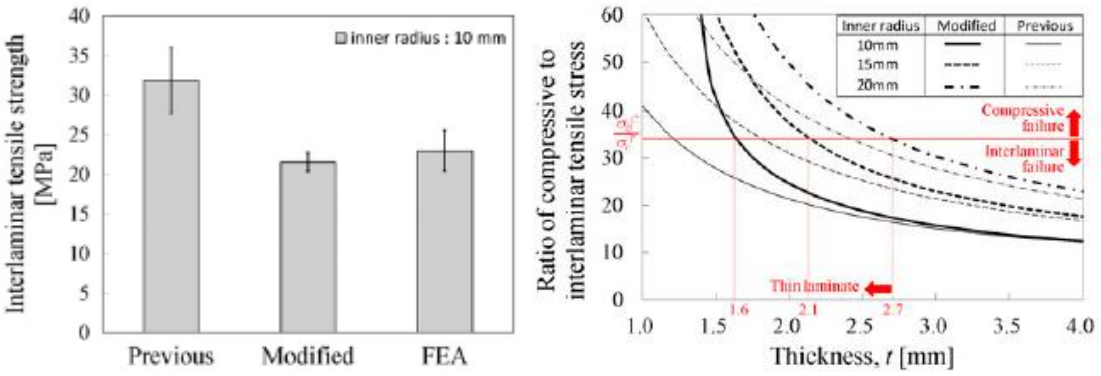

Figure 1-21 Determination of interlaminar tensile strength (left) and the effect of thickness on fracture behavior (right) [33]

Several numerical techniques have been presented to investigate the onset and propagation of delamination behavior of the composite material. Among them, the cohesive zone model (CZM) has been increasingly applied to simulate the delamination behavior and more general progressive damage in composite structures. Element-based cohesive zone model (ECZM) and surface-based cohesive zone model are common numerical techniques in CZM. M. Ramamurthi et al [37] compared the delamination behavior of bonded interface using ECZM and surface-based cohesive zone model. The results showed the surface-based cohesive zone model works well for prediction of delamination and the results showed good agreement with those obtained by the ECZM, whereas, the surface-based cohesive zone model shows the superiority in some aspects, such as modeling simply and computational time. D. Hu and C. Duan [38] applied the extended finite element method and surface-based cohesive behavior to predict the interfacial failure and matrix transverse cracking in carbon fiber reinforced composite. The surface-based cohesive behavior can be established readily by defining the contact pair and the interface properties are described by the contact property parameters. H. Wang et al [39] showed the cohesive element model, surface-based cohesive model and extended finite element method (XFEM) can successfully predict the damage initiation and propagation of Glass fiber reinforced polymer (GFRP). Besides, there are many studies based on CZMs in terms of interfacial stiffness, strength and the shape of traction–displacement curves, including curves described by bilinear, linear-parabolic, exponential, and trapezoidal laws. S. Jacques et al [40] investigated the effect of multiple parameters including stabilization method, output frequency, the friction, stiffness, strength and asymmetric thicknesses of specimen substrates on simulation results of the delamination behavior

for GF/Epoxy and CETEX CF/PPS composites. G. Alfano [41] showed that whether the shape of the softening curve is an important factor for numerical simulation results may rely on the ratio between the interlaminar toughness and the interfacial stiffness, which can be obtained by analyzing the effect of the interfacial shape on debonding by using CZM. E. Panettieri et al [42] proposed a sensitivity study for investigating the effects of the interfacial strength and cohesive mesh size in simulations of low-velocity impact. The results showed that the choice of the cohesive mesh size and the values of maximum traction had a significant impact on the computed performances. By studying the influence of the cohesive law on the simulation of ductile crack propagation, H. Yuan and X. Li [43] showed that the initial cohesive stiffness of the cohesive zone in compact tension specimens is insensitive to the results. P.F. Liu et al [44] studied the effect of cohesive law parameters on the post-buckling and delamination behavior under compression by three-dimensional (3D) finite element analysis. The results indicate that the fracture process zone is significantly influenced by the geometrically nonlinear deformation at the unstable delamination stage between the initial buckling and global buckling. Furthermore, R. Campilho et al [45] showed that the effect of the CZM law (see in Figure 1-22) on the iterative solving procedure and the computational time should be considered when using trapezoidal rather than triangular CZM law due to a sudden change in stiffness of cohesive elements during stress softening. M. Ridha et al [46] conducted research on parametric studies on fracture behavior of a bonded scarf repair and the results shown in Figure 1-23 indicate that the results obtained by the numerical model with exponential traction-separation law are insensitive to interfacial strength, whereas the results from the models with linear and trapezoidal laws depend on both interfacial strength and toughness.

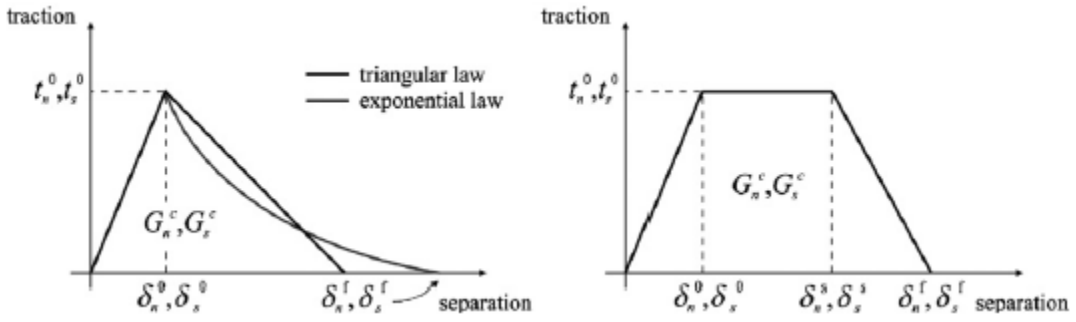

Figure 1-22 CZM laws with triangular, exponential and trapezoidal shapes [45]

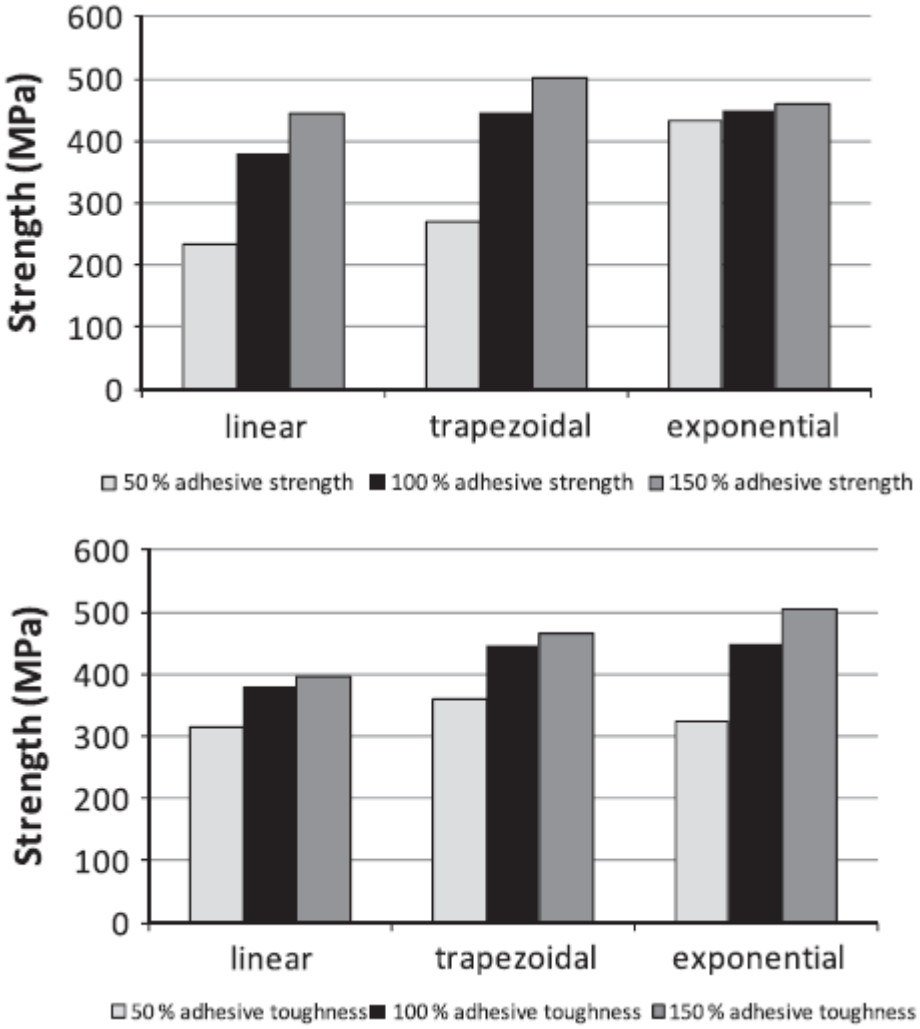

Figure 1-23 Strength of repaired models with different types of adhesive traction–separation law and variation in interfacial strength and toughness [46]

1.2.2.2 Flexure and impact behavior of CFRP

Some efforts have adopted fracture behavior of braided or fabric composites hollow beam and panel under flexural and impact loadings.

Q. Liu et al [35] explored fracture behavior and crashworthiness characteristics of double hat-shaped tubes made of weave CFRP subjected to transverse bending and quasi-static axial crushing. In the axial crushing tests, progressive end crushing, unstable local buckling and mid-length collapse were observed (see in Figure 1-24), while progressive failure process was observed in transverse bending tests (see in Figure 1-25). Besides, the load-bearing capabilities and energy

absorption of the CFRP double hat-shaped tubes subjected to transverse bending are much lower than those of the axially compressed tubes. T. Matsuo et al [47] numerically and experimentally investigated the fracture behavior of randomly oriented thermoplastic composite tubes under axial compressive impact as shown in Figure 1-26. The results show that the progressive crushing caused by delamination failure results in the high axial energy absorption performance, and finite element model should be established with consideration of the out-of-plane normal and tangential fracture behavior of the random-chopped composites. M. Meng et al [48] illustrated the significant effects of fiber layup on the flexural failure mechanisms by developing a 3D finite element model with the Tsai-Hill failure criterion. O.T. Topac et al [49] established FE model (see in Figure 1-27) in which intraply matrix damage was simulated base on LaRC04 initiation criterion and delamination was simulated by creating cohesive interface elements. J.K. Zhang and X. Zhang [50] developed a computationally efficient finite element model of CFRP laminates to predict fracture behavior under low-velocity impact loading using surface-based cohesive contact and quasi-static loading to represent the low-velocity impact loading as shown in Figure 1-28. It is concluded that the model can be efficiently used to simulate the delamination.

Also there are several studies on the bending fracture behavior of metal complex structures strengthened with CFRP. M. Yamashita and I. Yamamoto [51] experimentally studied the flexural behavior of aluminum (Al) hat-shaped tubular structure with CFRP sheet under quasi-static and impact loadings, and the effect of CFRP sheet position, the thickness of the sheet and the velocity on the flexural behavior. The results show that the positive strain-rate sensitivity of adhesive and CFRP sheet result in 10% greater of energy absorption in impact tests than that in quasi-static tests (Figure 1-29), and 40% and 10% greater of energy absorption performance can be achieved when the CFRP sheet was attached to both the hat top and the hat bottom, and the hat sides, respectively. H.C. Kim et al [52] investigated bending collapse behavior and energy absorption performance of Al/CFRP short square hollow section (SHS) beam under transverse quasi-static loading with consideration of different layup sequences and laminate thicknesses. The specific energy absorbed improvement of 29.6% can be achieved in hybrid specimen with a $[0°/+45°/90°/-45°]_n$ lay-up sequence and 8 plies of prepreg because the catastrophic fracture mode of CFRP was changed to the progressive failure mode which results from the formation of a plastic hinge (Figure 1-30). S.Y. Kim et al [53] compared collapse mechanisms and energy absorption

performance of the Al/CFRP SHS beam under transverse quasi-static and impact loading. Unlike that in quasi-static tests, the collapsed specimen under impact loading shows more severe damage such as delamination, debonding and fiber breakage as shown in Figure 1-31 and the delamination results from the formation of cracks in the epoxy matrix. D.K. Shin et al [54] established finite element model of Al/CFRP hollow beam by using Hashin's damage initiation criteria and energy based damage evolution for intralaminar damage, and cohesive zone model with the traction-separation law for interlaminar damage (Figure 1-32). The progressive damage processes are: damage of CFRP and delamination can be firstly observed, and then debonding between aluminum and CFRP occurred, finally plastic buckling of Al and bending collapse behavior of the hollow beam was observed.

Figure 1-24 Failure modes: (a) mode I: progressive end crushing, (b) mode II: unstable local buckling, (c) mode III: mid-length collapse [35]

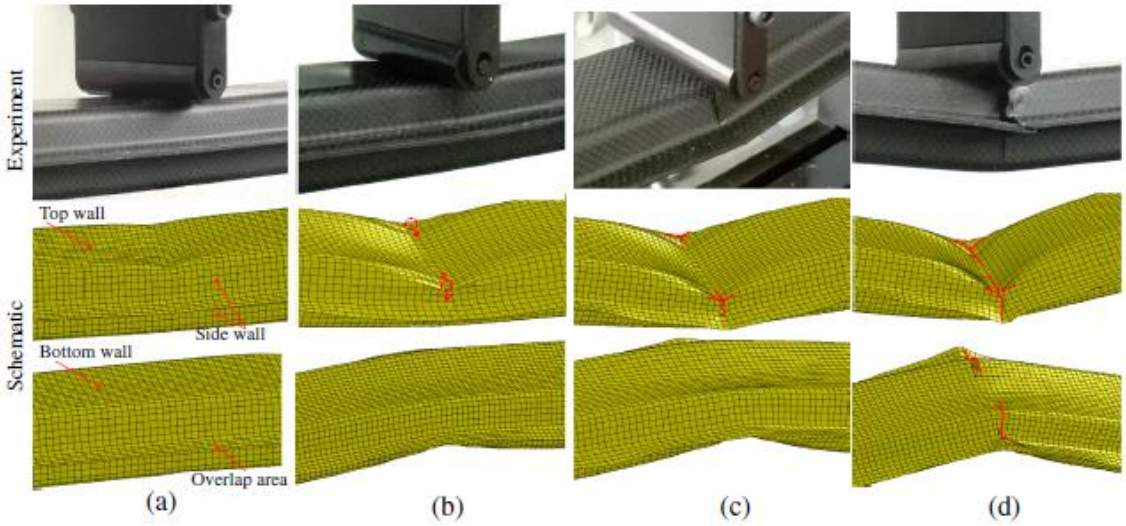

Figure 1-25 Progressive bending collapse process: (a) elastic bending, (b) crack initiation, (c) side wall rupture and (d) bottom wall rupture [35]

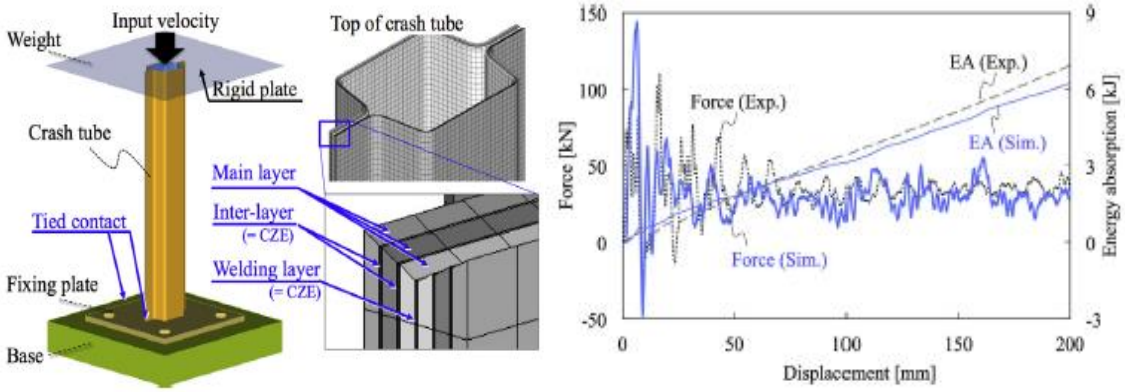

Figure 1-26 FE model of tubes (left) and the load-displacement curves (right) [47]

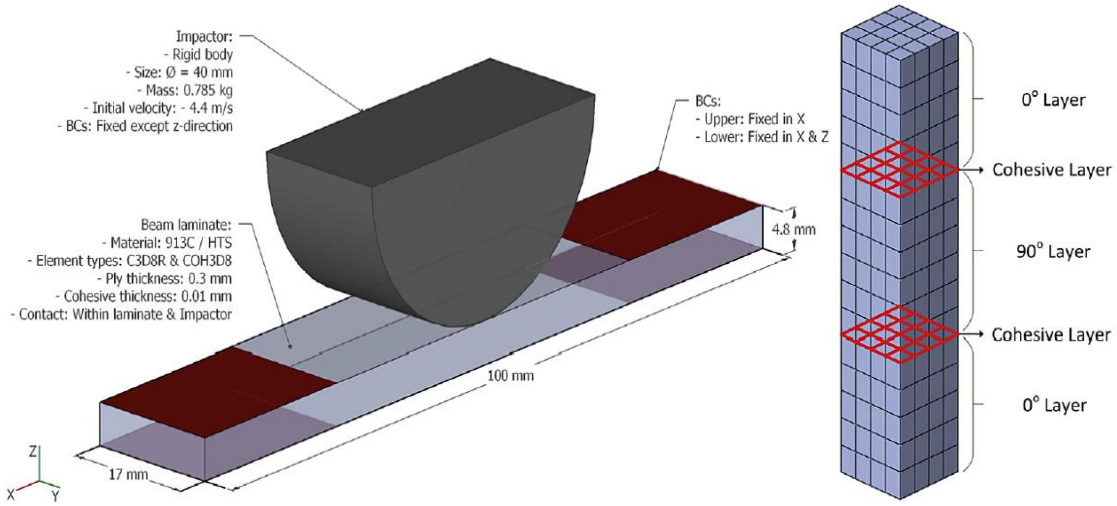

Figure 1-27 FEM of CFRP composite beams [49]

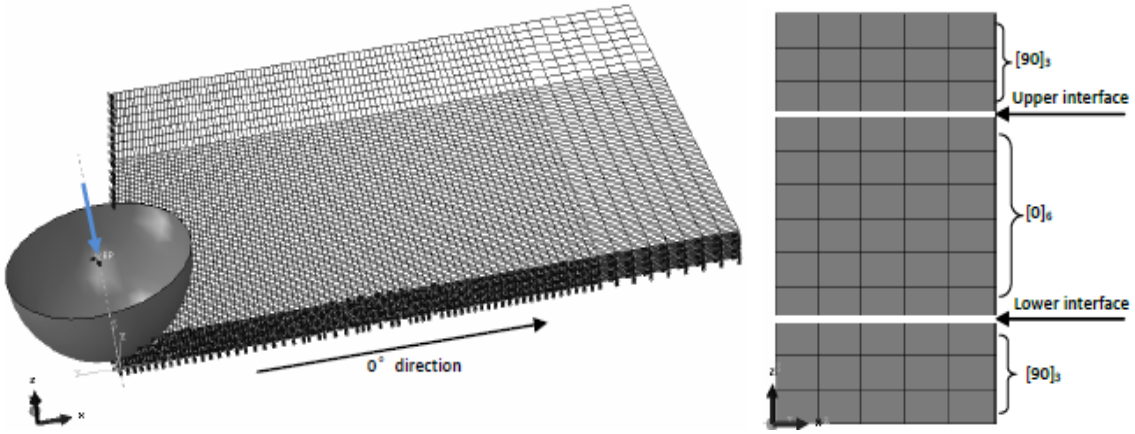

Figure 1-28 FEM of the rectangular specimen subjected to low-velocity impact loading [50]

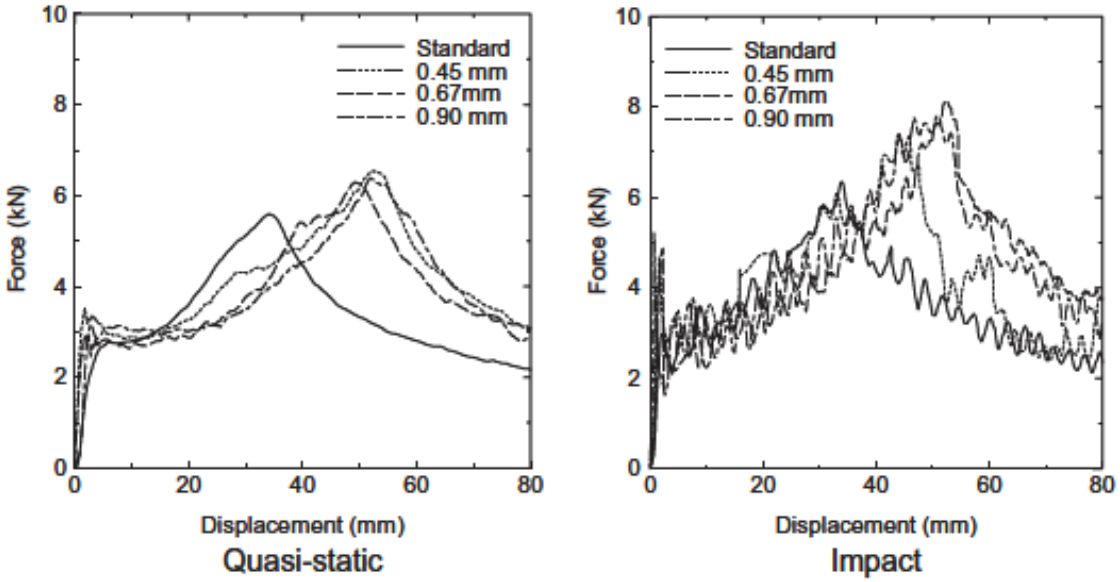

Figure 1-29 Load-displacement curves of aluminum structure with CFRP sheet attached to hat top under quasi-static (left) and impact loading (right) [51]

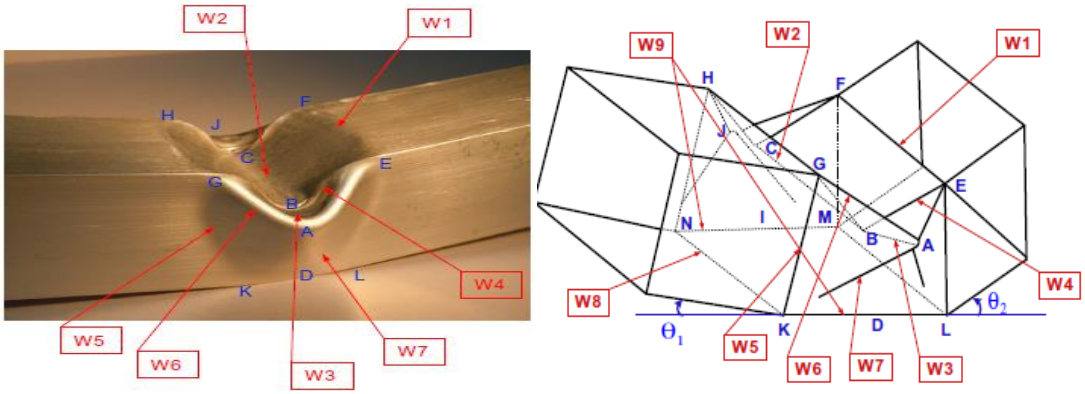

Figure 1-30 The photograph (left) and schematic diagram (right) of plastic hinge [52]

Figure 1-31 Comparison of collapsed specimen under quasi-static (left) and impact loading (right) [53]

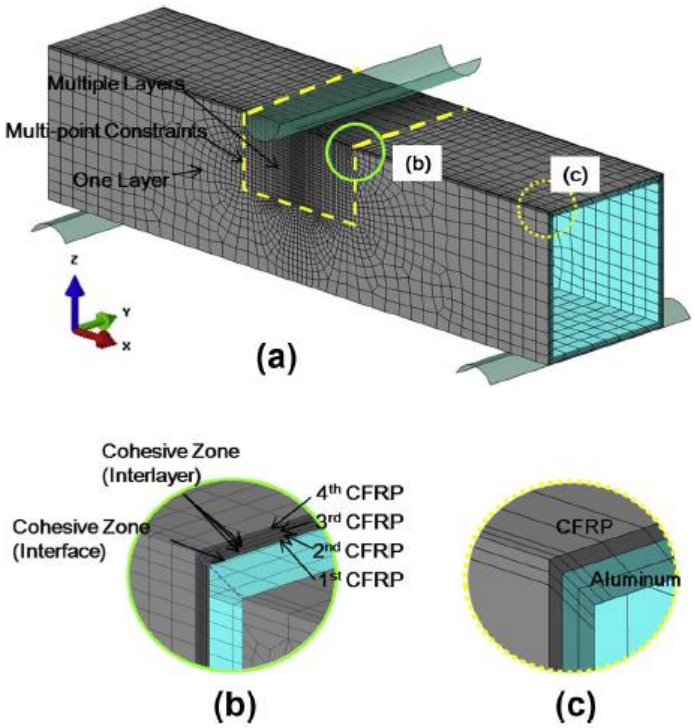

Figure 1-32 Finite element model of Al/CFRP hollow beam [54]

1.2.3 Design optimization of CFRP structures

Major studies in the field of composite design and optimization have focused on lightweight structure research and strength optimization.

T. Ohori et al [55] investigated the possibility of using topology, shape, and size optimization to fabricate more lightweight CFRTP S-crank frame structures, realizing a hybrid structure that was 60% lighter than a steel structure of the same stiffness. K. Ikeya et al [56] used the shape and thickness optimization under multi-boundary conditions to determine an optimal multi-objective free-form of a shell structure comprising orthotropic materials. J. Bös et al [57] developed user-written programs for optimizing the thickness distribution of 3D structures with consideration of vibrational and structural properties. D.H. Kim et al [58] used micro-genetic algorithm and eigenvalue buckling analysis to optimize the stacking sequence, and risks method to obtain the optimal CFRP lower arm with which failure load and stiffness became two times higher than a steel one while realizing weight reduction of 50%. X. Zhu et al [59] conducted multi-objective linear variable weights genetic algorithm to design optimal CFRP composite truss for minimizing the total weight, thermal expansion and maximizing buckling load, in which the design variable was the percentage of stacking sequence, satisfaction of the Tsai-Wu failure criterion as the constraint, and the weight of a structure and thermal expansion coefficient as the objective. J.G. Cho et al [60] described a lightweight design method for an EMU car body using material selection method and size optimization. As a result, a weight reduction of 29% was achieved by using CFRP-Al honeycomb sandwich composites and the size optimization method. X. Cui et al [61] used the multi-objective genetic algorithm to find the lightweight automotive body assemblies in which design variables are the material types and thickness of the panels. The conclusion is that the developed method with a combination of material selection and thickness determination is reasonable for the lightweight design. M.N. Velea et al [62] conducted research on single-objective and multi-objective optimization of an FRP sandwich body of an electric vehicle. The objective of the multi-objective optimization is reducing weight, reducing material cost and increasing the stiffness of local and global parts; the design variables are thickness and distribution of each layer while the constraints are the failure index which was determined by the Tsai-Hill criterion. The trade-off between two objectives, such as mass vs torsion stiffness, mass vs bending stiffness and mass vs material cost by defining Pareto front with consideration of the

weight of each objective can be achieved as shown in Figure 1-33.

Moreover, several studies have focused on strength optimization. M. Kalantari et al [63, 64] developed a model to predict the flexural properties of glass and carbon fiber reinforced epoxy hybrid laminates based on classical lamination theory. In the optimization problem, uncertain variables were the fiber angles and thicknesses of each lamina, and the objectives were to minimize the cost and weight, and the constraint was minimum specified flexural strength. Two kinds of multi-objective robust optimization methods were presented: 1) The weighted sum method (WSM) was utilized to find the optimal solution and the weighting factors were calculated from the analytical hierarchy process (AHP). 2) Hybrid multi-objective optimization evolutionary algorithm (MOEA) was developed which was modified based on an elitist non-dominated sorting genetic algorithm (NSGA-II) and combining it with the fractional factorial design method. L. Burns et al [65] optimized ply orientations to increase initiation peak load of the delamination in the carbon fiber/epoxy composite T-shaped structural joints while keeping their original stiffness and weight. F.R.S. da Cunha et al [66] developed a new robustness-based design strategy (see in Figure 1-34) to study design optimization of prepreg material IM7/8552 structures subjected to compressive loading, which simultaneously satisfies strength requirements and robustness requirements evaluated from the structural collapse energy. H.K. Ibrahim [67] investigated design optimization, which aims to maximize impact energy while maintaining its initial weight with gradient-based optimization algorithm, and also multi-objective optimization in which the objective is to minimize structural weight and maximize impact energy based on the Pareto front. Moreover, the material design optimization with genetic algorithm was used to find the optimal material types and thickness of each part, which aims to improve the crashworthiness performance. F.X. Irisarri et al [68] developed a multi-objective evolutionary algorithm to find the optimal composite stiffened panels in which the objective is the improvement of the first buckling load and ultimate collapse loads, and the stacking sequences are seen as the design variables. Meanwhile, radial basis functions under tension were used for reducing the calculation time. The optimization results show that 135% and 14% improvement on the first buckling load and ultimate collapse loads were achieved, respectively. L.P. Chaves and J. Cunha [69] optimized the distribution of the reinforcement of CFRP for minimizing the quantity of material using topology optimization (Figure 1-35). R.A. Raorane and N. Gilke [70] conducted research on stress analysis

of CFRP cylinder shell structures using classical laminate theory; moreover, the fiber orientation and ratio of longitudinal to transverse fibers based on the above analysis were optimized. The fiber orientation 55 degrees and the ratio between 0.3 and 0.6 can be found with consideration of the strength criteria. Y. Mo et al [71] explored the optimal cross-section of the composite hat-stringer-stiffened using Nonlinear Programming by Quadratic Lagrangian (NLPQL) algorithm in iSIGHT and MATLAB codes (Figure 1-36). R.H. Lopez et al [72] compared optimization results with consideration of different failure criterion including maximum stress, Tsai-Wu and the Puck failure criterion as constraints. In the optimization problem solved by the genetic algorithm, the weight and material costs are objectives and the ply orientations, the numbers of layers and the layer material are design variables. The comparison results show that the optimal design depends on the failure criterion, but there is no direct connection between optimal results and failure criterion.

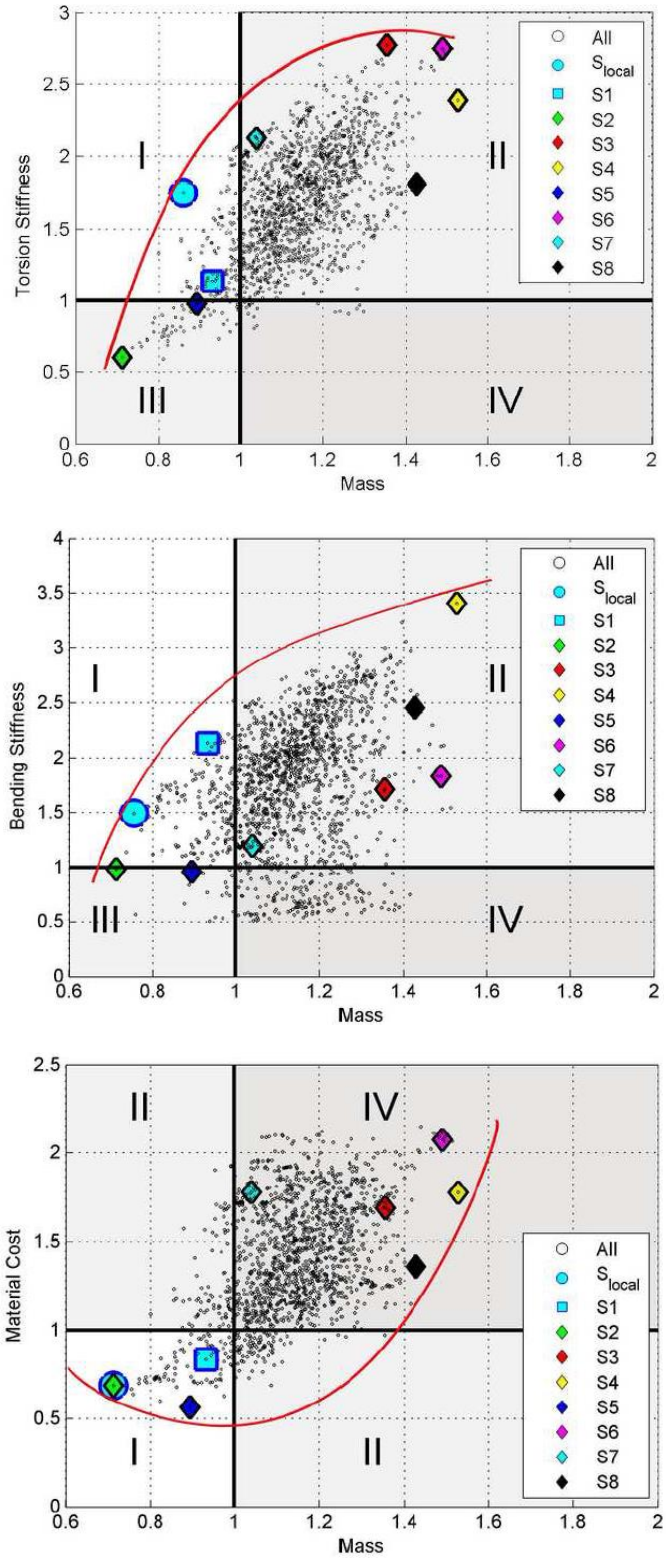

Figure 1-33 Trade-off between mass and torsion stiffness, bending stiffness, material cost [62]

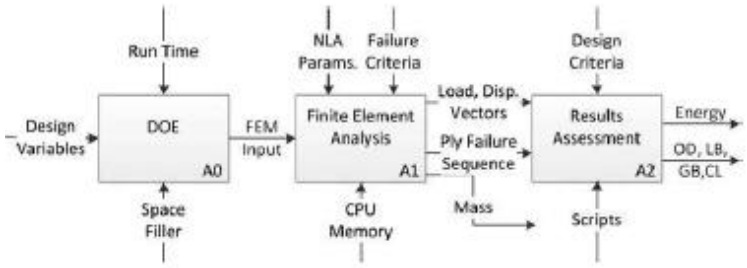

Figure 1-34 Simulation procedure [66]

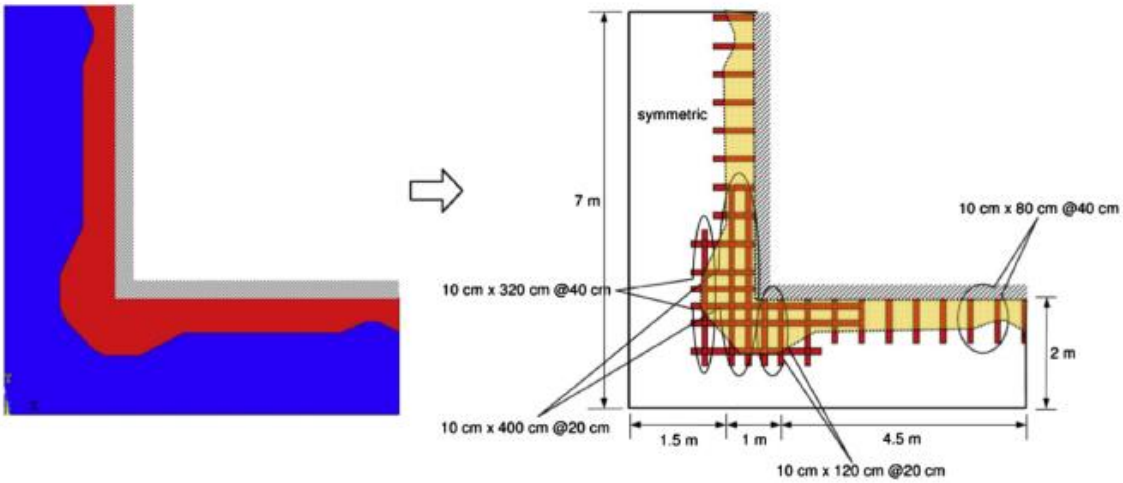

Figure 1-35 CFRP reinforcement region with topology optimization [69]

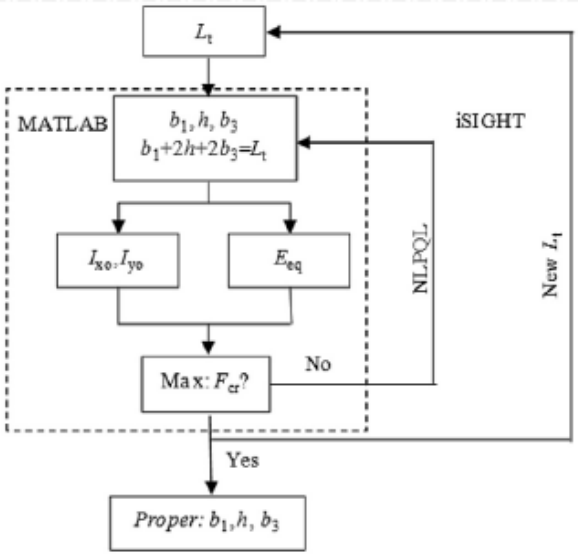

Figure 1-36 Optimization flow chart of NLPQL algorithm in iSIGHT and MATLAB codes [71]

1.3 Research objectives

In Japan, a long-term national project is being supported to carry out research about the weight reduction of mass production automobile by CFRTP with maintaining or improving the mechanical performance of the relevant structures [73-75]. For mass production applications of CFRTP, the following requirements should be satisfied such as high mechanical properties, low material cost, low manufacturing cost and high complex formability. One of several CFRTP material systems developed in the project namely CTT (Chopped carbon fiber tape reinforced thermoplastics), which shows the in-plane isotropic properties (see in Figure 1-37) [9, 76], was prepared from randomly oriented CF/PA6 ultra-thin unidirectional prepreg tapes. The advantages of CTT that carbon fiber volume fraction can reach over 50% and could be molded under relatively low pressure result in a mass application of vehicle structures. Researches on determination and impact factors of mechanical properties, functional properties, fracture behavior and structural optimization of CTT have been investigated [32, 76-85]. The comparison between different material systems has shown in Table 1-1.

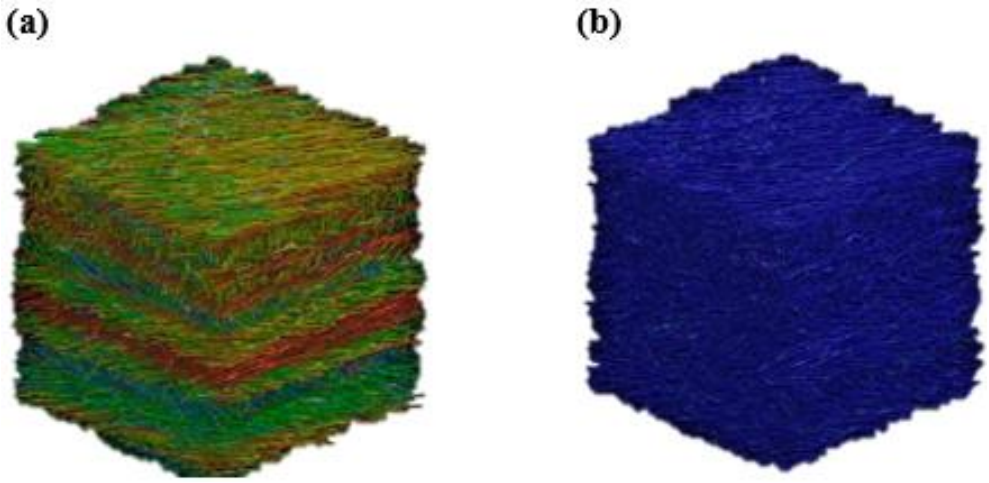

Figure 1-37 (a) In-plane and (b) out-of-plane fiber orientation of CTT [9, 76]

Table 1-1 Comparison of continuous and discontinuous CFRTP

Type	Continuous laminates	Injection molded	CTT
Fiber volume fraction V_f	High (>50%)	Relatively low	High (>50%)
Aspect ratio L/D	Highest	Low (variation)	High (hundreds-thousands)
Complex Design	Difficult	Suitable	Suitable
In-plane isotropy	Designable	Process dependent	Feasible

This dissertation investigates the fracture behaviors of complex components made by ultra-thin chopped carbon fiber tape reinforced thermoplastics (UT-CTT), as well as design optimization of these complex components. The objectives are as follows:

1) To clarify the interlaminar properties of UT-CTT, including interlaminar fracture toughness and interlaminar tensile strength;

2) To investigate fracture behaviors of UT-CTT hat-shaped hollow beam under transverse static and impact loadings, and develop a modelling technique for accurately expressing fracture behaviors;

3) To achieve optimal structures by taking full advantage of the merit “thickness variation” of UT-CTT.

In conclusion, the study can provide theoretical and numerical solutions to express fracture behaviors of UT-CTT structures, and show the lightweight potential of UT-CTT for industrial applications.

1.4 Organization of the thesis

This dissertation is divided into five chapters.

Chapter 1 firstly introduces the motivation of this research, and then literature reviews on development of CFRP, fracture behavior of CFRP and design optimization of CFRP structures were summarized. Finally, the research objectives and structure of the thesis were presented.

Chapter 2 investigates the interlaminar fracture toughness of UT-CTT and delamination behavior of UT-CTT L-shaped structure with a combination of theoretical calculation, experiment, and numerical simulation.

Chapter 3 experimentally and numerically involves fracture behaviors investigation of UT-CTT hat-shaped hollow beam under transverse static and impact loadings.

Chapter 4 conducts research on design optimization of CFRTP complex structures including L-shaped structure and hat-shaped hollow beam which aims to show the superiority of UT-CTT on thickness variation and lightweight.

Chapter 5 makes major conclusions of this work and future research are also discussed.

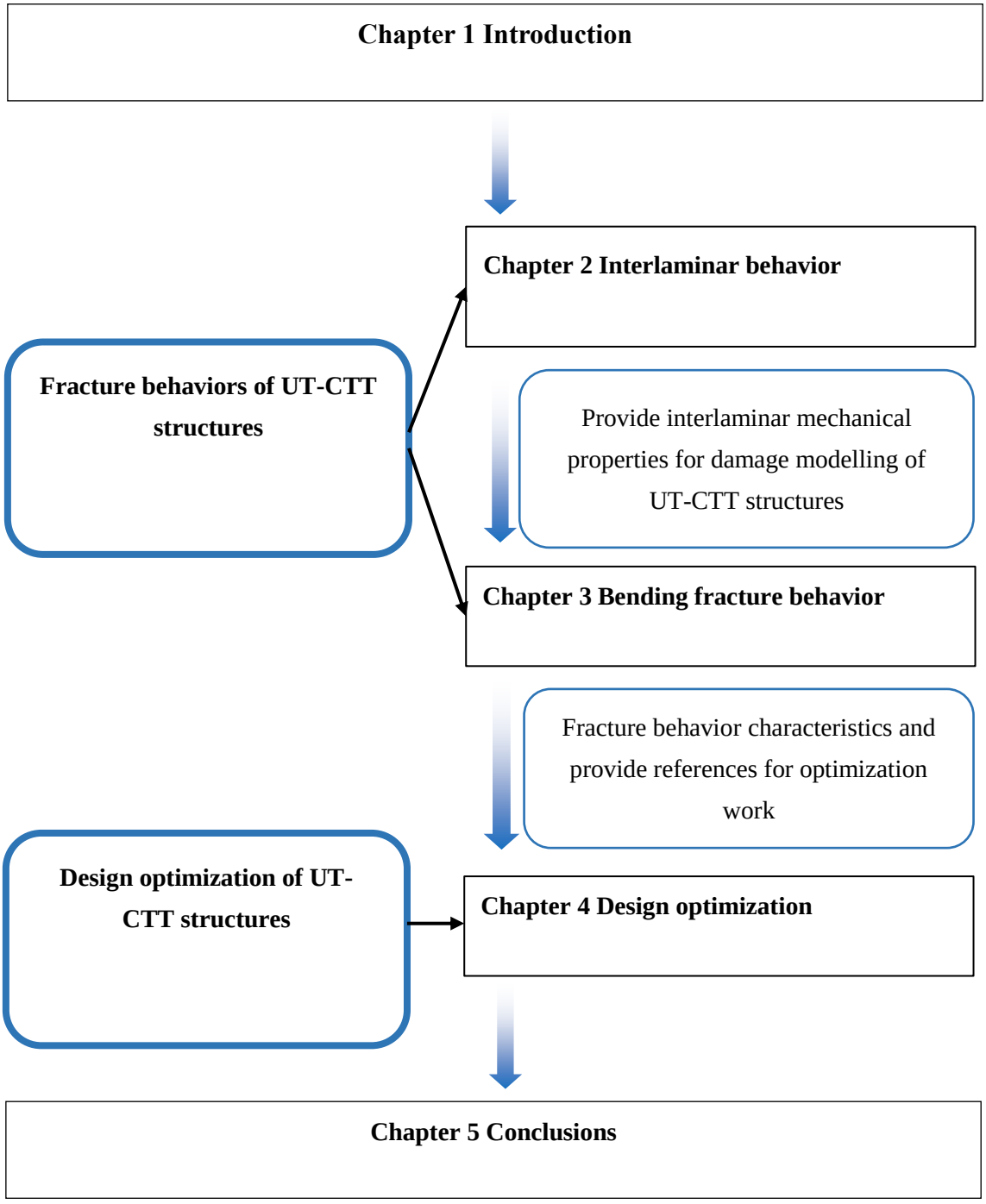

Figure 1-38 Flowchart of an overview of the doctoral dissertation

2. Interlaminar behavior of UT-CTT

2.1 Introduction

This chapter will theoretically, experimentally and numerically conduct research on the interlaminar behavior of UT-CTT. Double cantilever beam (DCB, mode I), end notched flexure (ENF, mode II) and four-point bending test of L-shaped specimens was investigated to determine the interlaminar fracture toughness and interlaminar tensile strength. The values of mode I and mode II interlaminar fracture toughness were obtained based on linear elastic fracture mechanics and beam theory in reference to JIS K 7086 standard, respectively. Besides, a computationally efficient model using surface-based cohesive zone model was developed for predicting delamination behavior of UT-CTT and validated by experimental and analytical methods.

2.2 Manufacture process

The UT-CTT samples were prepared from randomly oriented CF/PA6 ultra-thin unidirectional prepreg tapes. The tape was manufactured from carbon fibers (TR50S, Mitsubishi Rayon Co. Ltd., Japan) and polyamide 6 (PA6, Mitsubishi Plastics Co. Ltd., Japan). The preparation process of UT-CTT specimens was described in Figure 2-1. The prepreg sheets were cut into tapes measured 19 mm in length, 5 mm in width, 44 μm in thickness. Then, the chopped tapes were dispersed randomly using water dispersion method. After that, the tapes were sandwiched between two polytetrafluoroethylenes (PTFEs), which were subsequently attached together by heating, then the intermediate sheet was obtained. Finally, specimens were generated by stacking and press molding process.

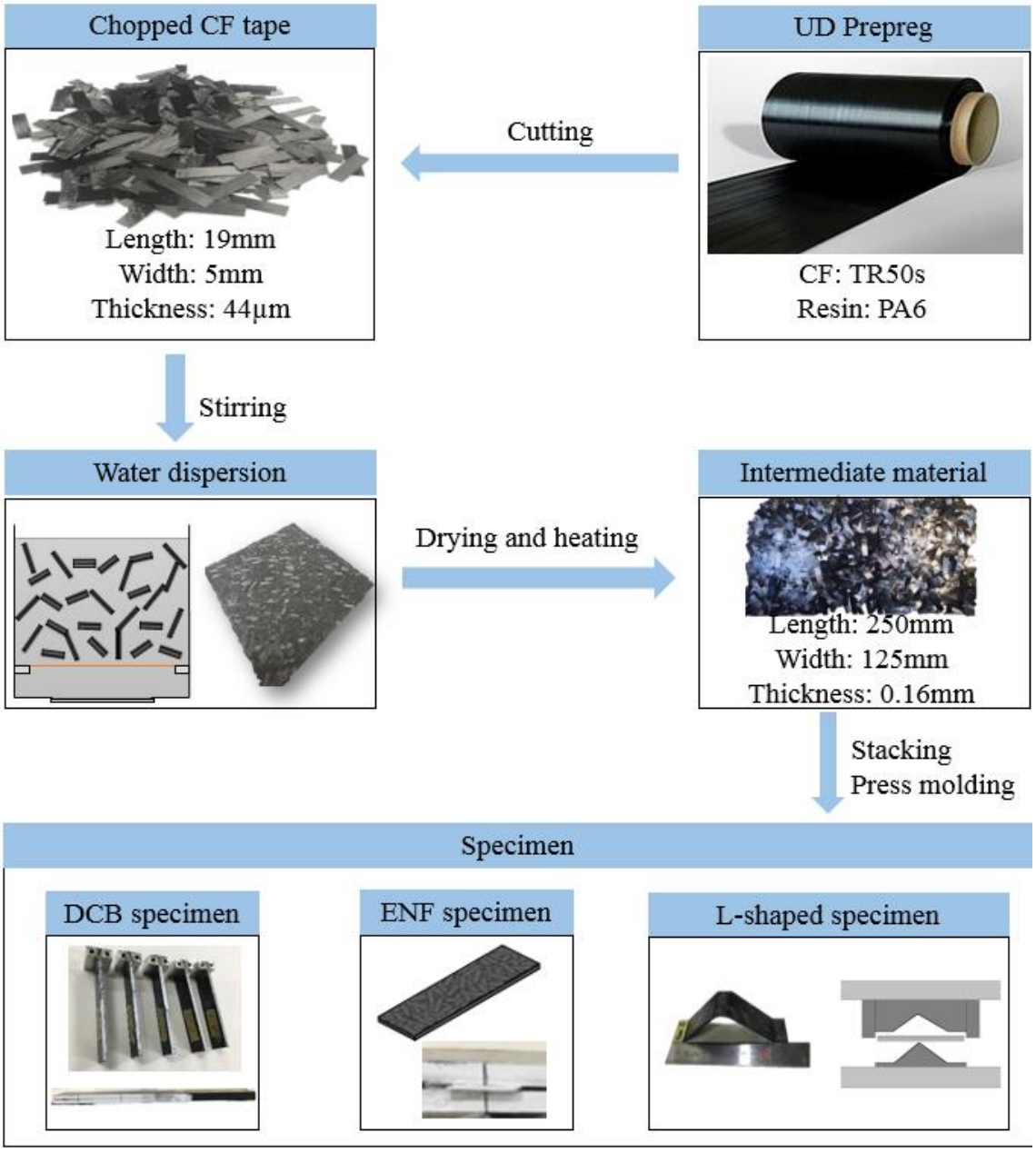

Figure 2-1 Preparation process of UT-CTT specimens

2.2.1 Cutting process

In order to obtain desired strand sizes of 18mm long with a constant width of 5 mm by chopping the prepregs, a digital cutting machine (Zund), also known as prepreg cutter, was used as shown in Figure 2-2. Prior to a cutting in a perpendicular direction to the aligned fibers, prepregs were precisely cut with 5 mm wide along longitudinal direction using with a maximum deviation of ±0.02 mm. By utilizing the operating system and control console, the accurate control of cutting

sequence, speed and areas were accessible. Also, vacuuming the lower side of prepregs could achieve dimensional conformance when cutting such thin sheets with particular dimensions. Cutting in the perpendicular direction was required using a customized cutter. Selecting length of the strand 18mm was easily achievable because various types of the cutter were designed to have a diversity of preform types for various experimental cases and purposes. Using the customized cutter and compression instrument allows one to fabricate accurate dimensions of chopped strands with negligible deviation.

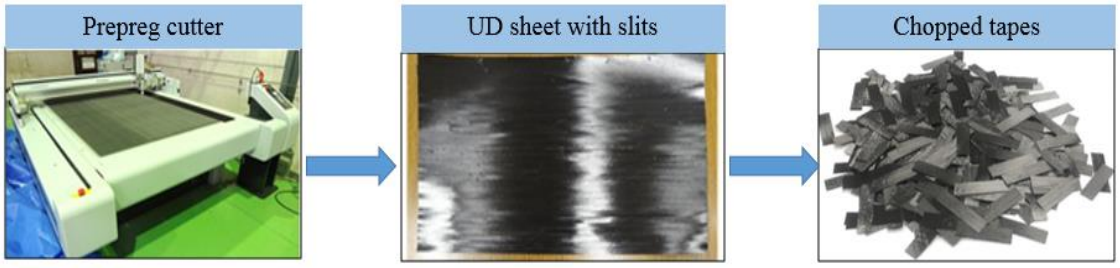

Figure 2-2 Cutting process of chopped tapes

2.2.2 Water dispersion method

In order to improve the controllability of the molding process and to facilitate the planar random orientation of fibers, water dispersion method was used. This method aims at minimizing the out-of-plane misalignment of the carbon fibers because the out-of-plane misalignment may degrade the mechanical properties of molded specimens. This process is considered as important because the ultimate goal of applying this material is the mass and continuous production using a conveyer belt with a form of sheets.

As shown in Figure 2-3, the water dispersion process is as follows: 1) The amount 23g of chopped strands were inserted in a container filled with water to achieve planar random orientation by stirring the filled water with centrifugal force. 2) The bottom of the water container was opened to flow out filled water, while the chopped strands were filtered through a mesh frame (280 × 280 mm). 3) The sheet-form was obtained after evaporating water.

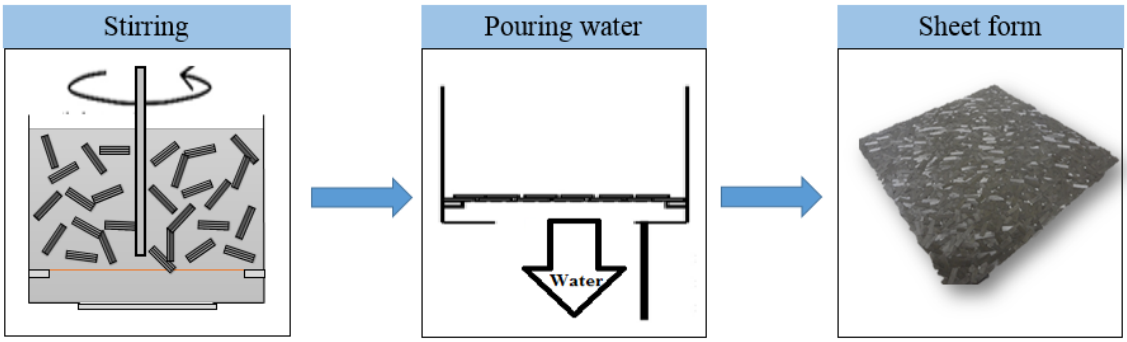

Figure 2-3 Water dispersion process

2.2.3 Manufacturing process of intermediate material

Since sheet form obtained in the above process was full of water, water absorbed in the strands was evaporated at 110 °C for 3 min, and then the filtered strands were heated and pressed at 260 °C for 1 min to make a final form of sheets with a square dimension (250 × 250 × 0.16 mm) as shown in Figure 2-4. The sheets were not fully compressed and consolidated and contain internal free spaces. Therefore, imposing sufficient consolidation by compression and heating was significant during forming procedures. The preform sheets were dried (90 °C for 12 h) using a vacuum oven, minimizing deterioration of material properties by water absorption of PA6 matrix in prepreg sheets.

Figure 2-4 Manufacture process of intermediate material

2.2.4 Specimen manufacturing process

As shown in Figure 2-5, after the obtained intermediate sheet was cut into pieces with the mold dimensions, the delamination was induced by inserting a 50 μm thick polyimide (PI) film between the two middle layers, and then the necessary number of layers pieces were stacked to produce thicker UT-CTT plates. Finally, the UT-CTT plates were cut into DCB and ENF specimens using

a diamond disk cutter, and the man-made pre-crack was created using the wedge. In order to apply loads to DCB specimens via pins, Aluminum blocks were bonded on the DCB specimens, and a small coupon of PTFE film of 0.15-0.30 mm thickness was inserted between the crack surfaces in ENF specimens.

L-shaped specimens were manufactured by laminating necessary plies of intermediate sheets by heat-and-cool compression molding using a set of upper and lower L-shaped molds as shown in Figure 2-6.

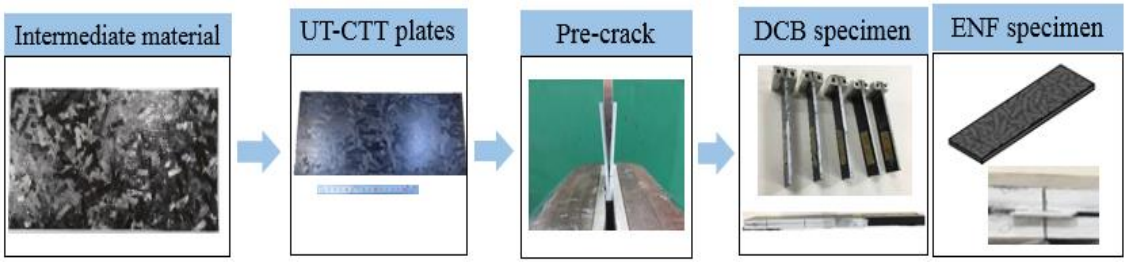

Figure 2-5 DCB and ENF specimen manufacture process

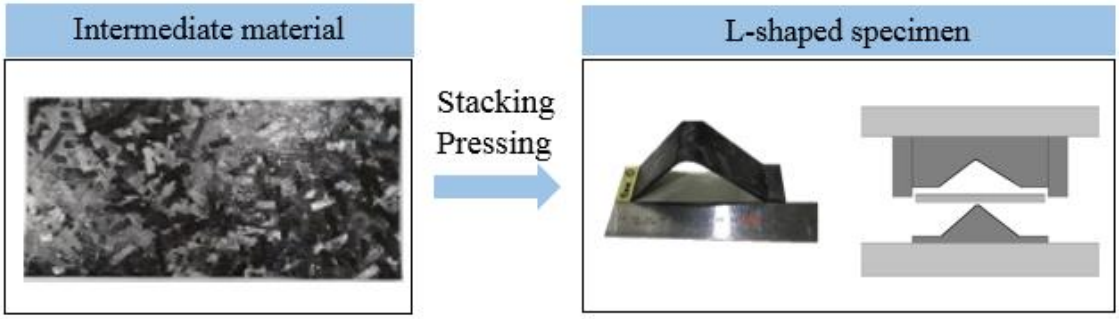

Figure 2-6 L-shaped specimen manufacture process

2.3 Interlaminar fracture toughness of UT-CTT

2.3.1 Experimental investigation

The DCB and ENF tests were performed according to guidelines in JIS K 7086 from the Japanese Industrial Standards Association [86] to investigate three kinds of specimens: 48-ply UT-CTT laminate, 36-ply $[0°_{36}]_s$ UD laminate, 48-ply $[0°, 90°]_{24s}$ Cross-ply (CP) laminate. The dimensions of the specimens are as shown in Table 2-1. The side edge of each specimen was painted white and scaled to observe the crack growth. All the tests were performed using a universal test machine (AUTOGRAPH AGS-5kN, Shimadzu Cooperation, Japan). The schemes and photographs of the DCB and ENF test setups are shown in Figure 2-7. Loads were applied to the specimen via pins through universal joints in DCB tests, and for ENF tests, a small coupon of PTFE film of 0.15-0.30 mm thickness was inserted between the crack surfaces to reduce the friction between the upper and lower substrates during the shear movement. The size of the coupon was 25 mm wide, and 5 mm long in the specimen longitudinal direction. It was placed just above the supporting cylinder. The stroke speed was 1 mm min^{-1} for the DCB tests and 2 mm min^{-1} for the ENF tests. It should be noted that the geometric boundary condition, $a_0/L = 0.5$ is setup for ENF tests in JIS K7086 standard while $a_0/L > 0.7$ is necessary to ensure stable crack growth by using compliance-based beam method for the determination of mode II fracture toughness [87].

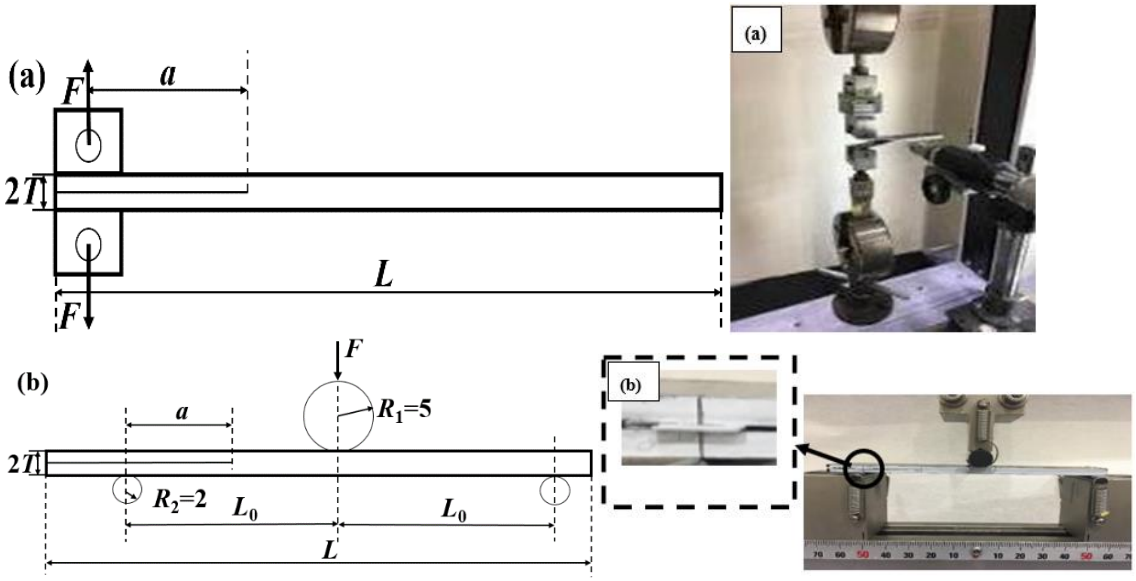

Figure 2-7 The schemes and photographs of (a) DCB and (b) ENF test setups

Table 2-1 Dimensions of DCB and ENF specimens

	(mm)	DCB		ENF		
	Specimen	L × B × 2T	a	L × B × 2T	a	L_0
UT-CTT	E1	120 × 24 × 4.2	33.5	122 × 24 × 4	25	50
	E2	120 × 24 × 4.2	36	122 × 24 × 4	25	50
	E3	120 × 24 × 4.2	35	122 × 24 × 4	25	50
	E4	120 × 24 × 4.2	35.5	122 × 24 × 4	25	50
	E5	120 × 24 × 4.2	35	122 × 24 × 4	25	50
UD	E1	120 × 24 × 3	36	117 × 24 × 3	25	50
	E2	120 × 24 × 3	35.5	115 × 24 × 3	25	50
	E3	120 × 24 × 3	35	115 × 24 × 3	25	50
	E4	120 × 24 × 3	37	116 × 24 × 3	25	50
				116 × 24 × 3	25	50
CP	E1	117 × 24 × 4.02	36.5	118 × 24 × 4	25	50
	E2	117 × 24 × 4.11	38.5	118 × 24 × 4	25	50
	E3	118 × 24 × 4.09	38	117 × 24 × 4	25	50
	E4	118 × 24 × 4.05	36	118 × 24 × 4	25	50
	E5	118 × 24 × 4.01	35	118 × 24 × 4	25	50

2.3.1.1 Double cantilever beam tests (Mode I)

The load-displacement curves showing the results of the DCB tests for UT-CTT, UD and CP are presented in Figure 2-8. Unstable crack growth resulted in saw-tooth like load-displacement curves after the initial stage of increasing load in the DCB tests for all specimen. The unstable crack propagation is a consequence of regions with different toughness. When the crack reaches the tougher region, it slows down until the release rate of the stored elastic energy is enough to propagate the crack through the tougher region, therefore, the release rate of stored energy is higher than that required for stable growth leading to crack growth acceleration and an unstable fracture occurs.

For UT-CTT DCB specimens, the scatter can be observed in the load-displacement curves. More specifically, the initial bending stiffness of the specimen E1 was higher than that of other specimens because the initial pre-crack length of E1 was slightly lower than those of others. However, the initial bending stiffness of specimen E2 was higher than that of specimens E3, E4 and E5, which was unexpected because the initial pre-crack length of E2 was slightly larger than that of specimens E3,E4 and E5; this can be explained by significant variations in the opening stiffness when the crack position was varied in the vicinity of the center of the DCB specimen [19]. Fiber bridging phenomenon influences markedly the crack propagation energy, so the bridging force was eliminated by cyclic loading-unloading conditions in E4 and E5. In addition, the crack surfaces of the first UT-CTT DCB specimen and one of the unidirectional DCB specimens (for comparison purposes) were scanned by a 3D measurement macroscope. The thickness of the UT-CTT and UD DCB specimens are 4.2 mm and 3 mm, respectively. In Figure 2-9 and Figure 2-10, the different colors represent the variations in height, and it can be seen clearly that crack occasionally travels above the symmetry-plane, but the crack front of the UT-CTT DCB specimen was nearly straight, which is similar to that of the unidirectional DCB specimen.

2. Interlaminar behavior of UT-CTT

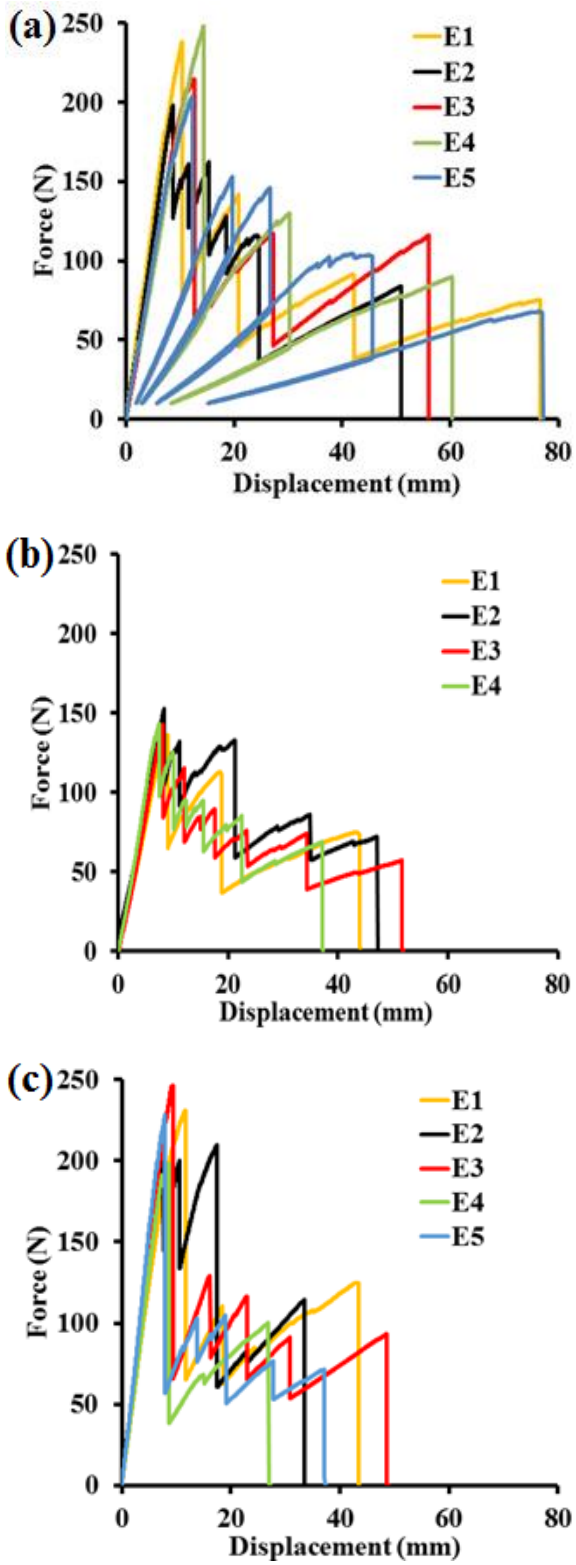

Figure 2-8 Load-displacement curves showing the results of DCB tests for (a) UT-CTT (b) UD (c) CP

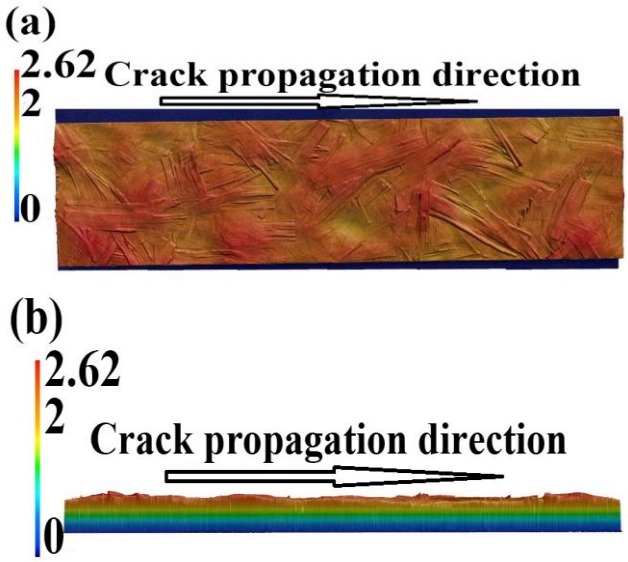

Figure 2-9 3D measurement macroscope of crack propagation region in UT-CTT DCB specimen: (a) top view (b) side view

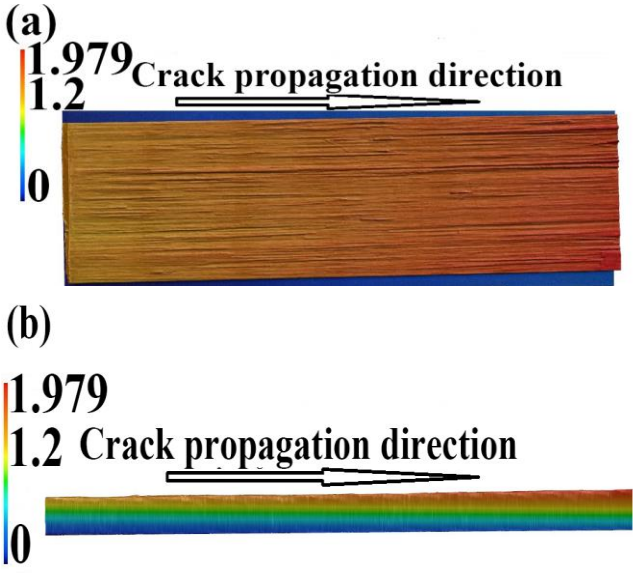

Figure 2-10 3D measurement macroscope of crack propagation region in UD DCB specimen: (a) top view (b) side view

2.3.1.2 End notched flexure tests (Mode II)

Figure 2-11 shows the corresponding load-displacement curves representing the results of the ENF experiments for UT-CTT, UD, and CP. The reproducibility of the ENF test results was very high (better than that of the mode I DCB tests). The force began to decrease when the crack was initiated and continued to propagate. For UD ENF specimens, all of the specimens show the stable crack propagation, whereas both stable and unstable crack propagation phenomenon could be observed for UT-CTT and CP ENF specimens. A scanning electron microscope (SEM) was used to investigate the cause of stable propagation of a crack for UT-CTT ENF specimen. The fractured E1 specimen was cut into two pieces (consisting of the upper beam and lower beam) along the crack propagation path after the ENF tests. Three different regions of the lower beam, including the crack origin, propagation path, and uncrack region, are shown in Figure 2-12. Two small areas of this sample were selected for SEM observation, and the SEM image in Figure 2-13 shows that matrix extension could resist crack growth, resulting in stable crack propagation during the ENF test.

2. Interlaminar behavior of UT-CTT

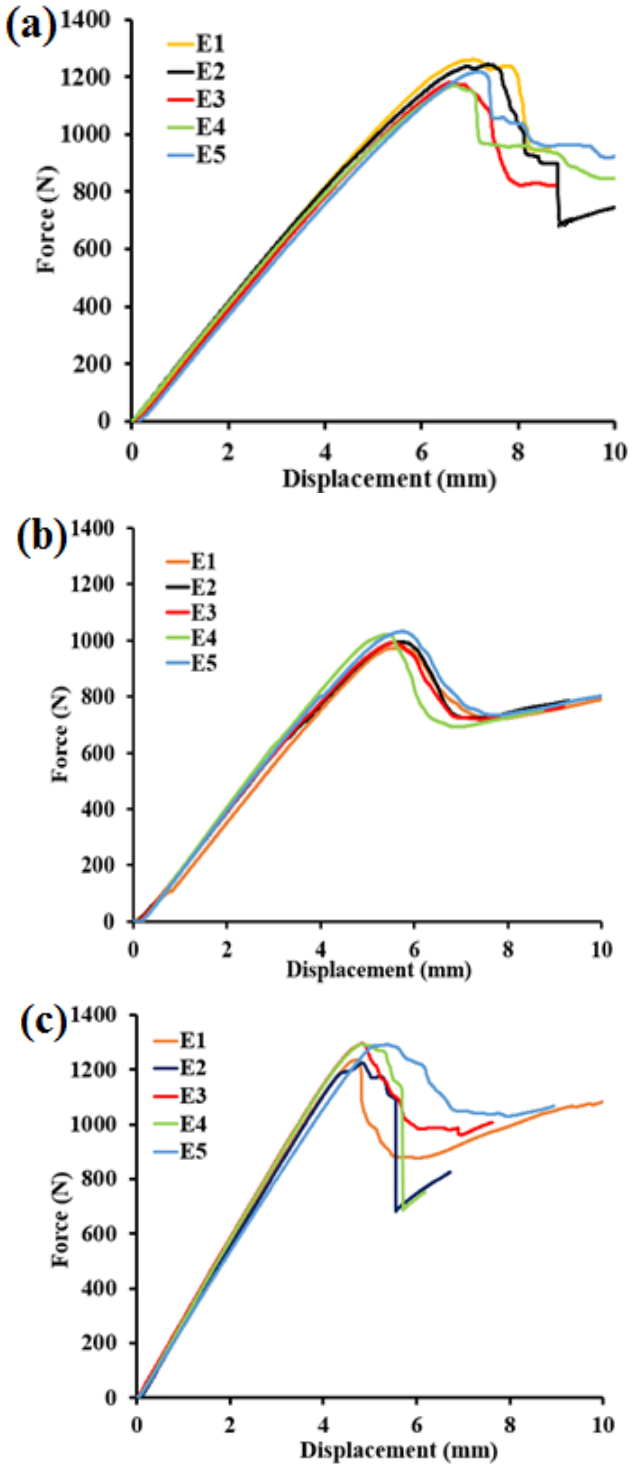

Figure 2-11 Load-displacement curves showing the results of ENF tests for (a) UT-CTT (b) UD (c) CP

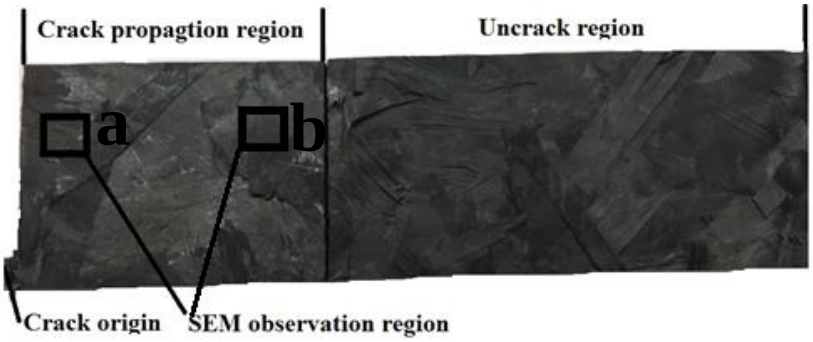

Figure 2-12 Three different regions of the lower beam in one ENF specimen

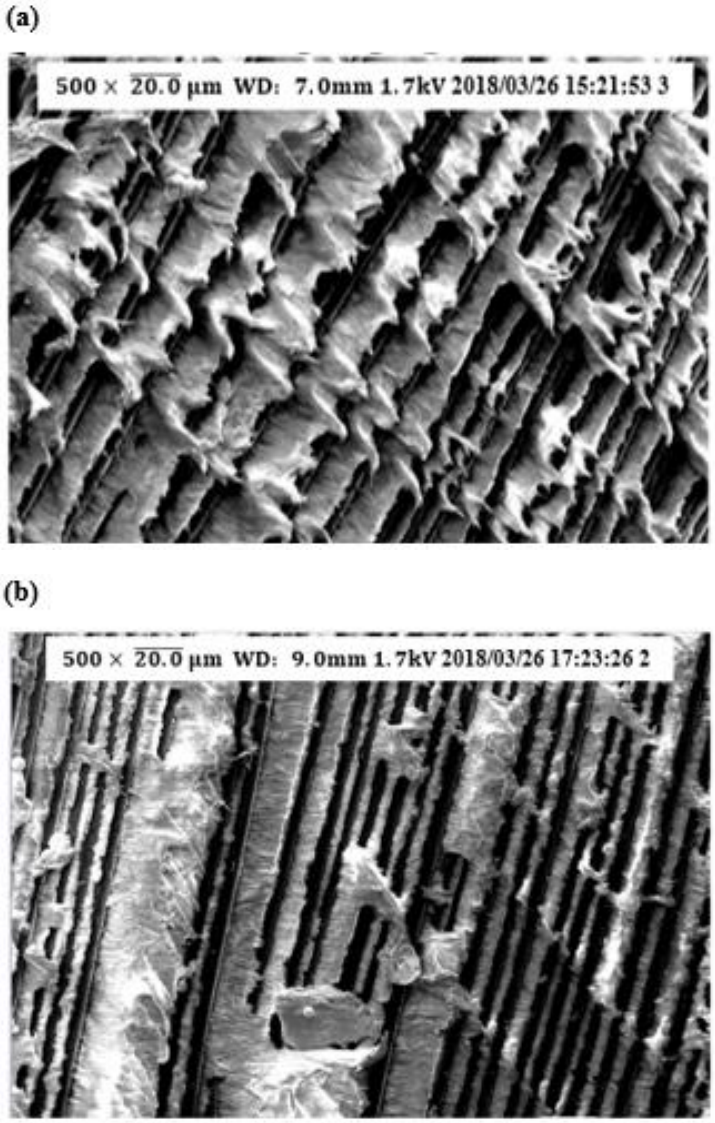

Figure 2-13 SEM fractograph of the crack growth (a) region a and (b) region b in a specimen after the ENF test (Left to right: crack propagation direction)

2.3.2 Theoretical investigation

2.3.2.1 Double cantilever beam tests (Mode I)

In order to determine the value of G_{Ic}, an analytical model based on linear elastic fracture mechanics was used. The force F and corresponding displacement δ was given by [88]

$$F = \sqrt{\frac{G_{Ic} B^2 T^3 E_1}{12a^2}} \qquad \textbf{Equation 2-1}$$

$$\delta = F \frac{8a^3}{BT^3 E_1} \qquad \textbf{Equation 2-2}$$

Eliminating a from both equations yields

$$F = \sqrt{8} B (T^3 E_1)^{\frac{1}{4}} \left(\frac{G_{Ic}}{12}\right)^{\frac{3}{4}} \delta^{-0.5} \qquad \textbf{Equation 2-3}$$

where G_{Ic} is the Mode I critical strain energy release rate, B is the width of the specimen, T is half the thickness of the specimen, E_1 is Young's modulus in the direction 1, a is the length of the delamination.

Since delamination length is impossible to be measured due to the unstable crack growth propagation and the curves exhibit non-linear response after linear response, the crack initiation point is given at the point of non-linearity according to [89]. It is noted that the value of G_{Ic} can be determined by fitting Equation 2-3 to the experimentally derived curves since all other parameters in Equation 2-3 are known. Since G_{Ic} corresponds with crack propagation, it is reasonable to fit it on all points of maximum force, corresponding with the point at which the crack will propagate. Therefore, by fitting Equation 2-3 through the first point of maximum force, which represents the crack initiation, yielded the initiation critical energy release rate $G_{Ic,initiation}$ and is illustrated in Figure 2-14. It can be seen that these curves do not capture the behavior after initiation well. Besides, the value of the propagation critical energy release rate $G_{Ic,propagation}$ was determined by fitting Equation 2-3 through all points of maximum force except the first. This is illustrated in Figure 2-15 and yields a better approximation for the curves.

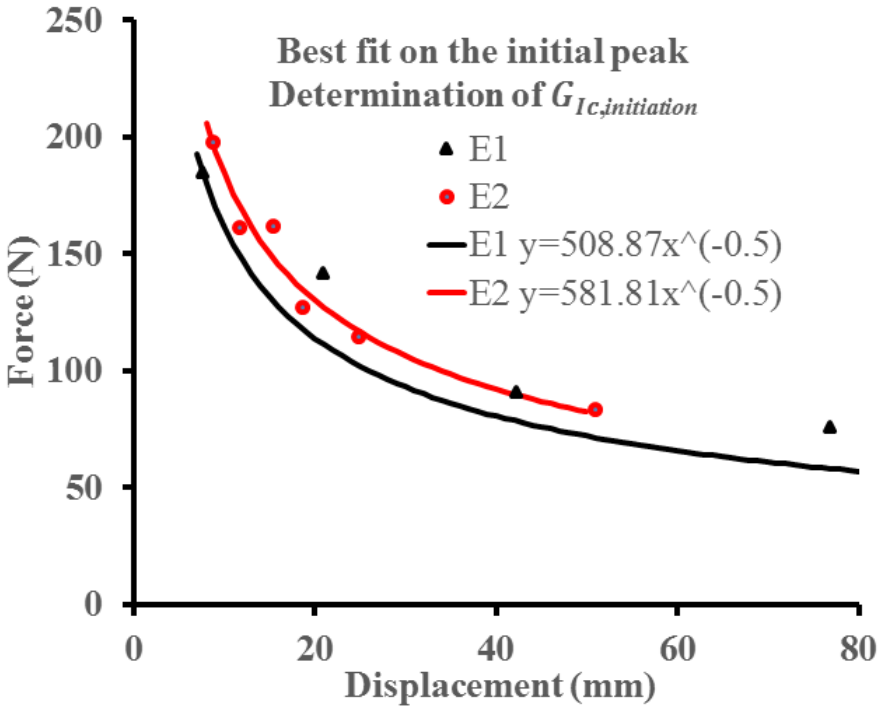

Figure 2-14 Determination of $G_{Ic,initiation}$

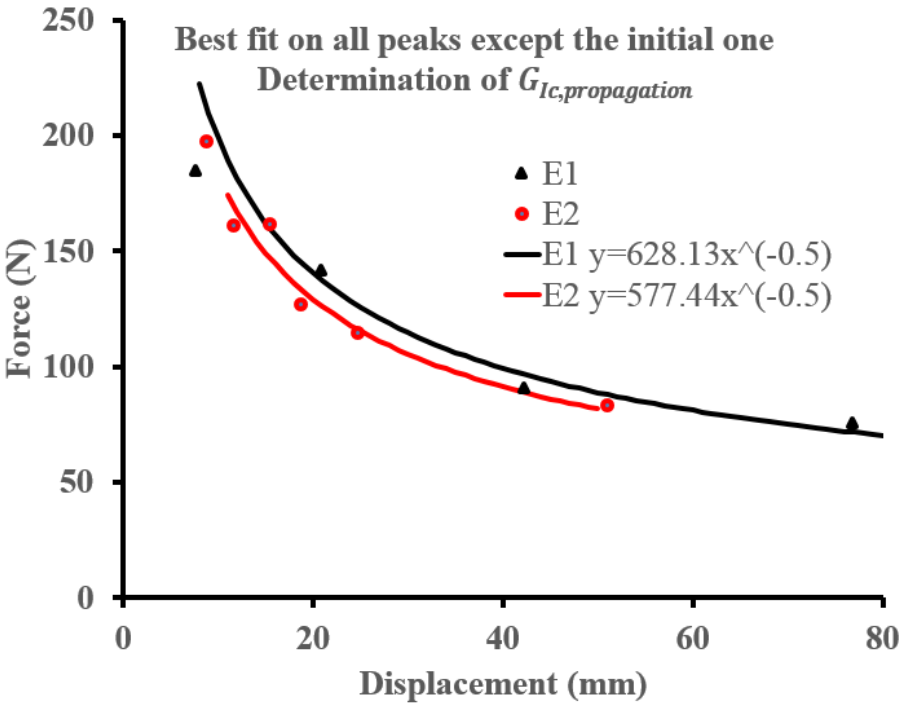

Figure 2-15 Determination of $G_{Ic,propagation}$

2.3.2.2 End notched flexure tests (Mode II)

The Mode II critical strain energy release rate G_{IIc} was determined using the Equation 2-4 and Equation 2-5 based on beam theory outlined in JIS K7086.

$$a = \left[\frac{C_1}{C_0} a_0^3 + \frac{2}{3}\left(\frac{C_1}{C_0} - 1 \right) L_0^3 \right]^{\frac{1}{3}} \quad \textbf{Equation 2-4}$$

$$G_{IIc} = \frac{9a^2 P_c^2 C_1}{2B\left(2L_0^3 + 3a^3\right)} \quad \textbf{Equation 2-5}$$

where G_{IIc} is the Mode II critical strain energy release rate, a_0 and C_0 are the initial crack length and load point compliance of the specimen, respectively. P_C indicates the critical load which is generally determined by maximum load or 5% offset load according to the load-displacement curve. a and C_1 are the crack length and load point compliance at $P = P_C$, respectively.

In this study, for specimens with stable crack propagation, the plateau value of R-curve can be seen as $G_{IIc,propagation}$ while an averaged $G_{IIc,propagation}$ was taken from the several plateaus in the R-curve due to unstable delamination growth in other specimens shown in Figure 2-16. Figure 2-17 gives an overview of Mode I and Mode II critical strain energy release rate.

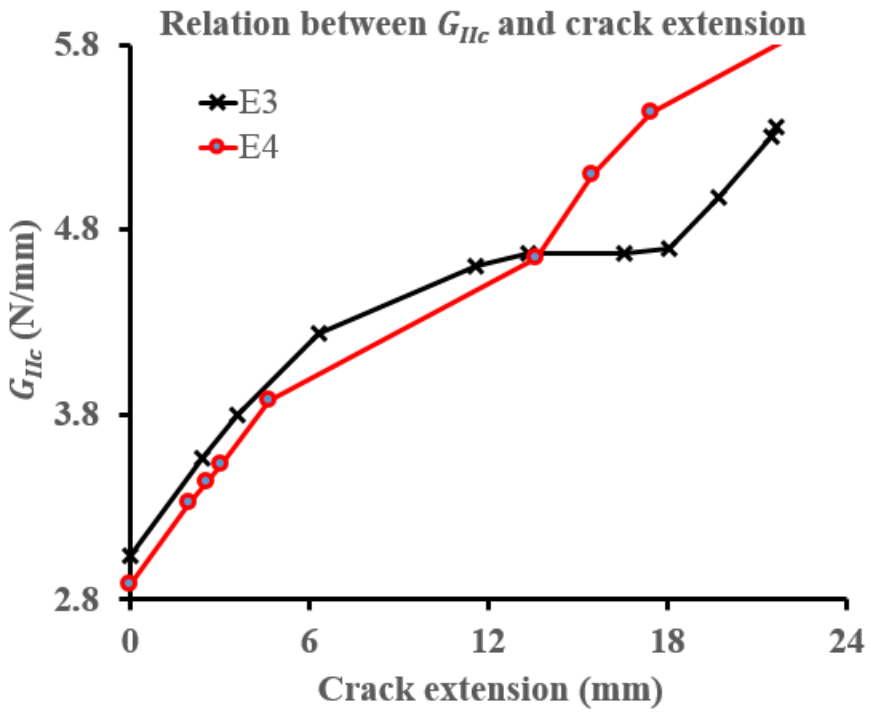

Figure 2-16 Determination of $G_{IIc,propagation}$

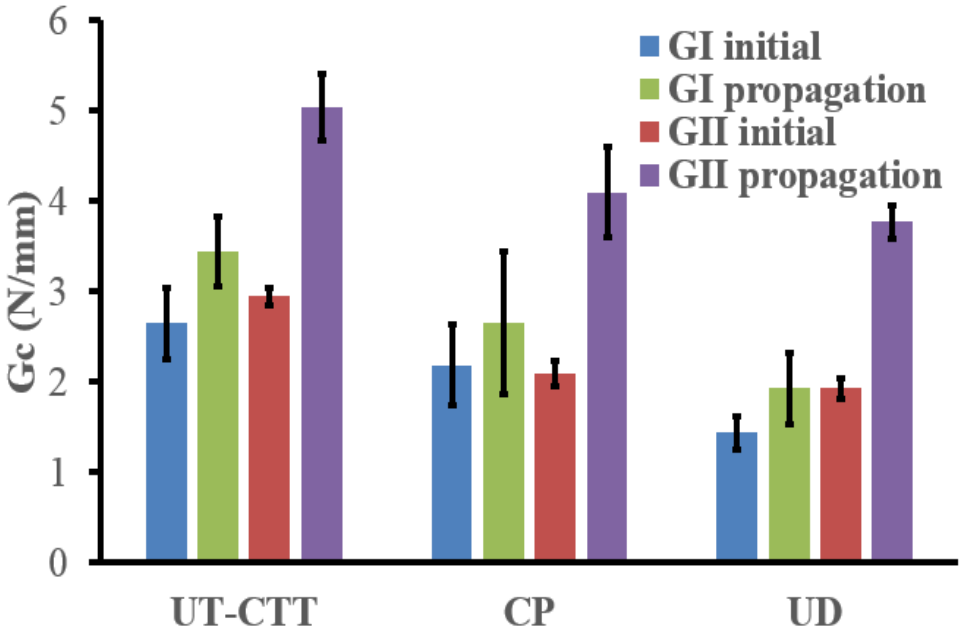

Figure 2-17 Resulting critical strain energy release rate for DCB and ENF tests

2.3.3 Finite Element Analysis

2.3.3.1 Interlaminar damage model

CZM is increasingly used to investigate the onset and propagation of delamination behavior of composite structures. The CZM can reproduce the whole delamination process including the linear stage up to a peak load, damage initiation, and crack growth. In most real applications interfaces are subjected to multiaxial loading, so interpolation of traction-separation laws of normal and shear modes for modes I and II as shown in Figure 2-18 can be used to simulate mixed-mode delamination behavior which caused by multiaxial loading.

After the initiation of delamination, a linear softening starts and the traction becomes zero at the critical displacement, and the area under the curve for each pure mode is characterized by the corresponding fracture toughness G_{ic}. Mode I fracture toughness G_{Ic} and Mode II fracture toughness G_{IIc} can be measured from DCB tests and ENF tests. The value of Mode III fracture toughness G_{IIIc} is seen as same as that of Mode II fracture toughness G_{IIc}. The mode-mixity is taken into account for the delamination onset and propagation based on quadratic nominal stress criterion and Benzeggagh-Kenane (B-K) criterion, respectively.

The quadratic stress criterion (as defined in the expression below) was used for damage initiation. The criterion can be represented as

$$\left\{\frac{\langle t_n \rangle}{t_n^0}\right\}^2 + \left\{\frac{t_s}{t_s^0}\right\}^2 + \left\{\frac{t_t}{t_t^0}\right\}^2 = 1 \qquad \textbf{Equation 2-6}$$

The mixed-mode propagation criterion is given as

$$G_c = G_{Ic} + (G_{IIc} - G_{Ic})\left(\frac{G_{II}+G_{III}}{G_I+G_{II}+G_{III}}\right)^{\eta} \qquad \textbf{Equation 2-7}$$

where B-K criterion constant η is a non-dimensional curve fitting factor obtained from the mixed-mode fracture toughness tests of a similar material.

The damage evolution law describes the degradation rate of material stiffness. Damage variable, D, means the overall damage in the material. The stress components of the traction-separation model are affected by the damage according to

$$t_n = \begin{cases} (1-D)\bar{t_n}, \bar{t_n} \geq 0 \\ \bar{t_n}, otherwise \end{cases}$$ **Equation 2-8**

$$t_s = (1-D)\bar{t_s}$$ **Equation 2-9**

$$t_t = (1-D)\bar{t_t}$$ **Equation 2-10**

Damage variable at any place on the loading curve for an element is determined using a linear damage evolution relation as

$$D = \frac{\delta_m^f(\delta_m^{\max} - \delta_m^0)}{\delta_m^{\max}\left(\delta_m^f - \delta_m^0\right)}$$ **Equation 2-11**

where t_n^0, t_s^0 and t_t^0 mean the peak value of the contact stress. n, s, and t correspond to normal to the interface, the first shear direction and the second shear direction, respectively. D is the overall damage at the contact point. $\bar{t_n}, \bar{t_s}$ and $\bar{t_t}$ represent the contact stress corresponding to the current separations without damage in the elastic traction-separation behavior. δ_m^f represents the effective separation at complete failure. δ_m^0 is the effective separation at the initiation of damage. $\delta_m^{\max}$ is the maximum effective separation.

Viscous regularization of the constitutive equations, which makes the tangent stiffness matrix of the softening material to be positive for sufficiently small time increments, was used to overcome severe convergence difficulties in the implicit analysis which results from softening behavior and stiffness degradation in the material models.

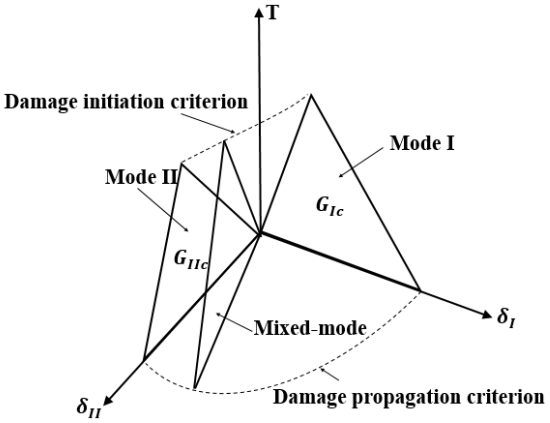

Figure 2-18 Constitutive law of interlaminar cohesive zone model in mixed-mode

In a pure normal (Mode I) or shear mode (Mode II), the traction increases linearly up to the interfacial strength. Triangular traction-separation law was used to simulate the crack initiation and propagation as shown in Figure 2-19. The interface stiffness K_i for mode I and mode II of the

traction–separation law, which correlates traction to separation before crack onset, is defined as [90]:

$$K_I = \frac{\alpha E_3}{T}$$ **Equation 2-12**

$$K_{II} = \frac{\alpha G_{12}}{T}$$ **Equation 2-13**

where E_3 is the through-the-thickness Young's modulus, G_{12} is the in-plane shear modulus, a value of >50 for α is sufficiently accurate for most problems. In this study, $\alpha = 50$.

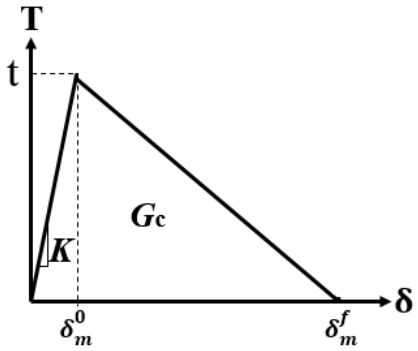

Figure 2-19 Triangular traction-separation law

2.3.3.2 Simulations of DCB and ENF tests

2D Finite element models (see in Figure 2-20 and Figure 2-21) were developed in Abaqus [37], the software suite for FE analysis, to simulate the delamination onset and propagation. The FE models were composed of four-node 2D plane strain elements. Surface-based cohesive contacts were inserted between two substrates because the surface based CZM is easier than the cohesive element approach to model cohesive connections [91]. For the DCB tests, the upper substrate was loaded at a speed of 1 mm min^{-1} at the appropriate nodes on loading blocks while the lower one was constrained only free rotation around Z-axis. For the ENF tests, the loading cylinder was loaded at the velocity of 2 mm min^{-1}. Surface-to-surface contact was considered between rigid cylindrical surfaces and the deformable substrates. Boundary conditions were included to fix the supporting cylinders in the X, Y, and Z directions and to restrain the loading cylinder in the Y direction, and the lowest node at the specimen mid-section was also restrained in the direction X. A very refined mesh with element sizes of 0.15 mm and 0.1 mm were used in a damage propagation zone in front of the crack tip; the mesh size was determined in the simulation of the DCB and ENF specimens after an investigation into the mesh dependence.

The values of $G_{Ic,min} = 2.14\ N/mm$ and $G_{Ic,max} = 3.78\ N/mm$ were used due to unstable crack propagation, and the interfacial tensile strength $t_n = 55.6\ MPa$, which was experimentally determined in Section 2.4.1, was used in the numerical simulation for DCB tests. In the case of ENF tests, the value of $G_{IIc,average} = 5.04\ N/mm$ (mean value determined experimentally) was used. Several test methods, including the short beam shear (SBS) test and compression shear test (CST), have developed for the purpose of characterizing the interfacial shear strength [92] and this work should be finished in the future in order to get more accurate numerical simulation results. In the present study, the value of the interfacial shear strength $t_s = 40.1\ MPa$ was obtained from [93]; however, the PA6 used in the reference was not the same as that in this study. Therefore, values of 60 MPa and 90 MPa were also used to show the influence of the interfacial shear strength. What is more, the influence of the friction was also carried out in ENF tests since the friction coefficient is very difficult to measure experimentally. Table 2-2 summaries the mechanical properties of UT-CTT.

Table 2-2 Mechanical properties of UT-CTT

Parameter		Value
Elastic Modulus (GPa)	E_1	44.8
	E_2	44.8
	E_3	7.33
Shear Modulus (GPa)	G_{12}	16.7
	G_{13}	1.08
	G_{23}	1.08
	μ_{12}	0.34
	μ_{13}	0.345
	μ_{23}	0.345
Mode I critical strain energy release rate (N/mm)	$G_{Ic,min}$	2.14
	$G_{Ic,max}$	3.78
Mode II critical strain energy release rate (N/mm)	G_{IIc}	5.04
The interface tensile strength (MPa)	t_n	55
The interface shear strength (MPa)	t_s	40.1, 60, 90

2.3.3.3 Numerical analysis results and discussion

Figure 2-22 shows the numerically obtained load-displacement curves corresponding to the minimum and maximum critical strain energy release rate values of $G_{Ic,min} = 2.14\ N/mm$ and $G_{Ic,max} = 3.78\ N/mm$ determined experimentally for DCB tests. All force values were normalized to a width of 24 mm. The numerical results show a good correlation with analytical results and with the experimental results for E1 and E2 test specimens. Both simulation results with $G_{Ic,min}$ and $G_{Ic,max}$ define a band in which the experimental and analytical results can fit. For ENF model, the friction coefficient between the substrates of the ENF model, and between the cylinders and the substrates were set as same, and friction coefficient of 0.02 and 0.2 was used to investigate the influence due to friction. Similar to the results of DCB tests, all force values were normalized to a width of 24 mm. The shape of load-displacement curves in Figure 2-23 remains similar, but a difference of maximum force for model C (the friction coefficient is 0.02) and model D (the friction coefficient is 0.2) reaches up to 6%, meanwhile, an obvious difference of maximum force can be seen when the interfacial shear strength changes from 40.1 MPa to 90 MPa. Moreover, 20% difference can be reached when a combination of interfacial shear strength and friction coefficient is taken into account. Therefore, as shown in Figure 2-24 the numerical results considering the above parametric studies show good agreement with the experimental results (E3 and E5) for ENF tests.

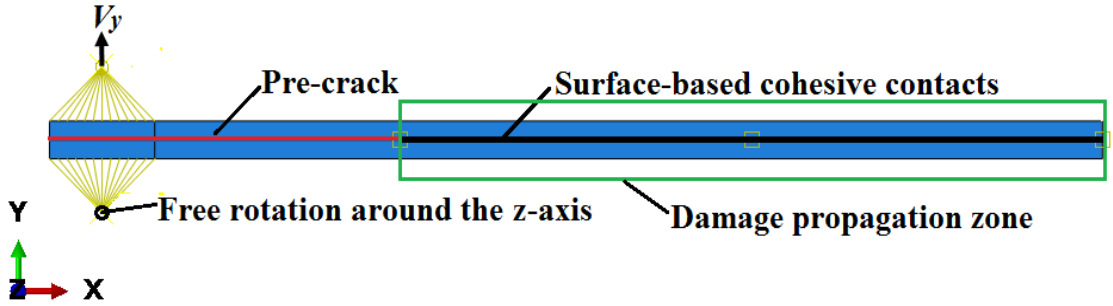

Figure 2-20 Finite element model of DCB tests

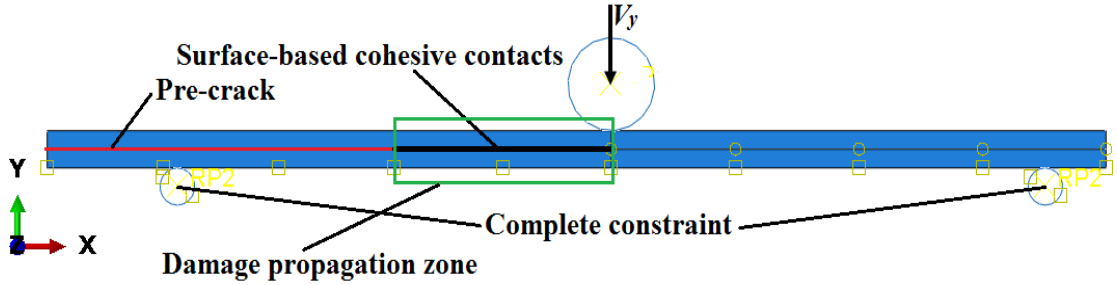

Figure 2-21 Finite element model of ENF tests

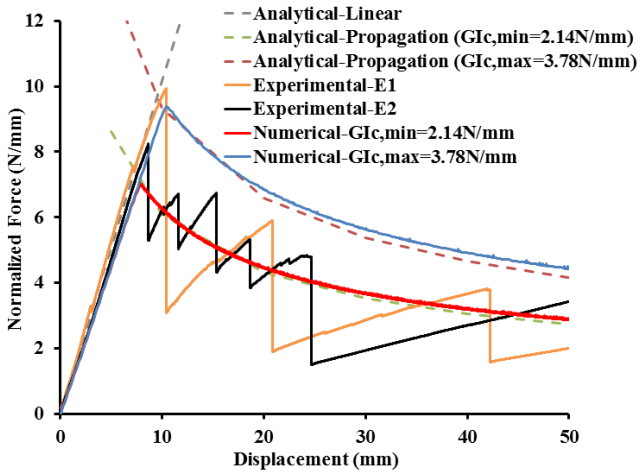

Figure 2-22 Numerical load-displacement results for DCB tests

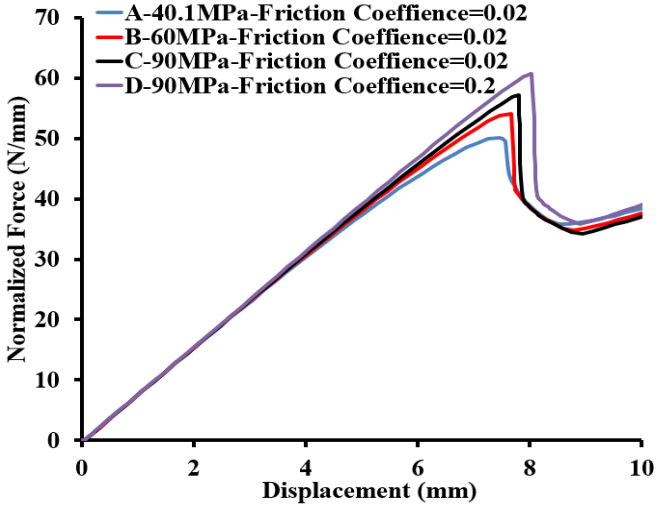

Figure 2-23 Influence of interfacial shear strength and friction coefficient on the numerical load-displacement curves for ENF tests

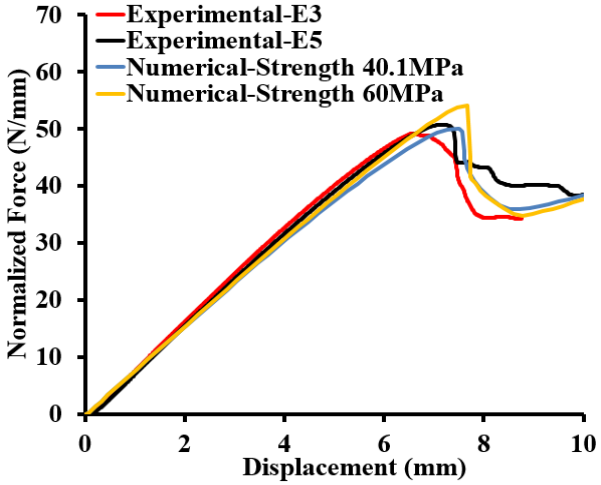

Figure 2-24 Numerical load-displacement results for ENF tests

2.4 Interlaminar tensile strength of UT-CTT

2.4.1 Experimental investigation

As illustrated in Figure 2-25, the produced specimens were characterized by the total length of each leg part ($L = 60\ mm$), width ($W = 35\ mm$), total thickness ($t = 2.2\ mm$), inner radius of the corner ($r_i = 5\ mm$), outer radius of the corner ($r_0 = 7.2\ mm$), and the angle between two leg parts ($\alpha = 90^{\circ}$). L-shaped structures were subjected to standardized four-point bending tests (Figure 2-26) [94], with the radii of cylindrical loading bars (R_1) and cylindrical support bars (R_2) equaling to 3 mm and 2 mm, respectively. Importantly, care needs to be exercised in choosing geometrical parameters such as distances between cylindrical loading bars (L_1) and cylindrical support bars (L_2) [95], since small L_1 could generate additional out-of-plane shear stresses and cause premature delamination, whereas small L_2 could result in through-the-thickness failure in leg parts. Therefore, the above parameters were optimized by preliminary FEM simulations to afford $L_1 = 14.2\ mm$ and $L_2 = 82\ mm$. All four-point bending tests were performed using a universal test machine (AUTOGRAPH AGS-5kN, Shimadzu Corp., Japan), and cylindrical loading bars were moved at a speed of 2 mm min^{-1} during loading until failure was observed.

Figure 2-25 Image (left) and dimensions (right) of a representative L-shaped specimen.

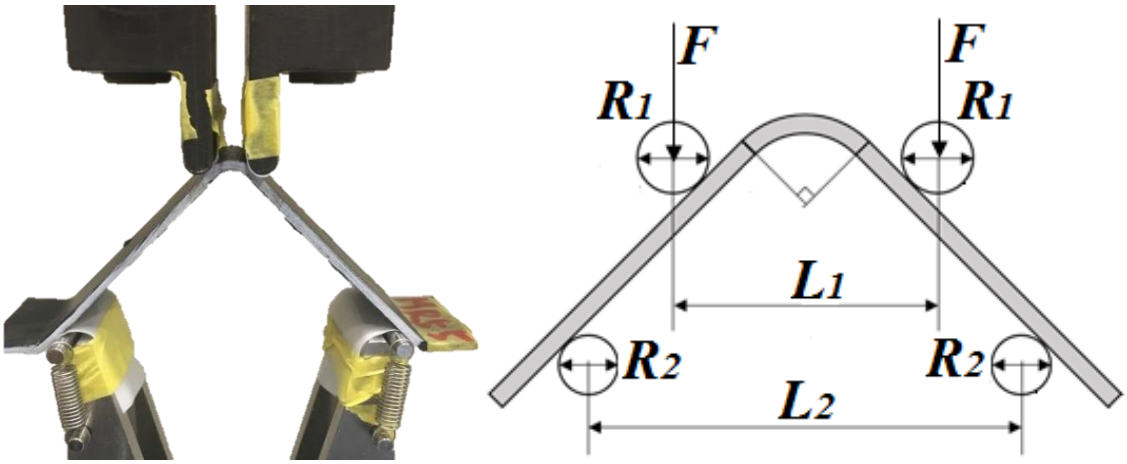

Figure 2-26 Setup of a four-point bending test: image (left) and schematic diagram (right)

2.4.2 Theoretical investigation

The analytical method was developed to determine the interlaminar tensile strength as shown below with the assumptions that the test section is in pure bending and the legs are perfectly rigid. The schematic of test configurations is as shown in Figure 2-27.

$$CBS = \left(\frac{P}{2w\cos\phi}\right)\left(\frac{d_x}{\cos\phi} + (D+t)\tan\phi\right) \quad \textbf{Equation 2-14}$$

$$\phi = \sin^{-1}\left(\frac{-d_x(D+t) + d_y\sqrt{d_x^2 + d_y^2 - (D+t)^2}}{d_x^2 + d_y^2}\right) \quad \textbf{Equation 2-15}$$

$$d_y = d_x\tan\phi_0 + \frac{D+t}{\cos\phi_0} - \Delta \quad \textbf{Equation 2-16}$$

$$\sigma_r(r) = \frac{CBS}{r_o^2 \cdot g}\left\{1 - \frac{1-c^{k+1}}{1-c^{2k}}\cdot\left(\frac{r_m}{r_o}\right)^{k-1} - \frac{1-c^{k-1}}{1-c^{2k}}\cdot c^{k+1}\cdot\left(\frac{r_o}{r_m}\right)^{k+1}\right\} \quad \textbf{Equation 2-17}$$

$$g = \frac{1-c^2}{2} - \frac{k}{k+1}\cdot\frac{\left(1-c^{k+1}\right)^2}{1-c^{2k}} + \frac{kc^2}{k-1}\cdot\frac{\left(1-c^{k-1}\right)^2}{1-c^{2k}} \quad \textbf{Equation 2-18}$$

$$r_m = \left[\frac{\left(1-c^{k-1}\right)(k+1)(cr_0)^{k+1}}{\left(1-c^{k+1}\right)(k-1)r_0^{-k+1}}\right]^{\frac{1}{2k}} \quad \textbf{Equation 2-19}$$

$$c = \frac{r_m}{r_o} \quad \textbf{Equation 2-20}$$

$$k = \sqrt{\frac{E_\theta}{E_r}} \quad \textbf{Equation 2-21}$$

where σ_r is the out-of-plane tensile stress at failure, P is the total applied loading, w is specimen width, D is the diameter of the cylindrical bars, t is specimen thickness, Δ is the imposed displacement at failure, r_0 is the inner radius, E_θ is equivalent to E_1, E_r is equivalent to E_3, CBS is curved beam strength.

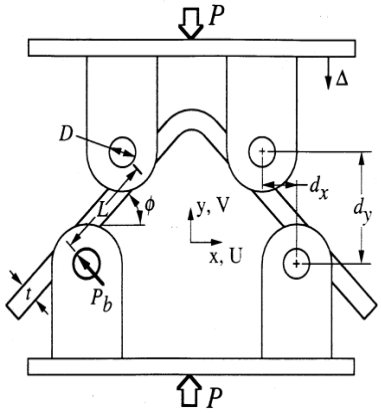

Figure 2-27 Schematic of test configurations

2.4.3 Finite Element Analysis

The above tests were also modeled using FEM to correctly estimate the stress field in the curved section at the failure load and thus determine interlaminar tensile strength. Four-node 2D plane strain finite element models were developed in Abaqus [91] to predict the global response and the final failure of the structure due to delamination in the curved section. The element size in the curved section was chosen to be small for obtaining a more accurate stress distribution, being increased in the two leg parts to reduce computational time. Element number with 14 in thickness was determined after an investigation of the mesh dependence, with the boundary conditions presented in Figure 2-28. The cylindrical loading bars moved at a speed V_y, whereas the cylindrical support bars were fixed. Moreover, free translation in the Y-direction was applied to the center nodes. Finally, contacts between cylindrical bars and the L-shaped structure were treated as surface-to-surface contacts.

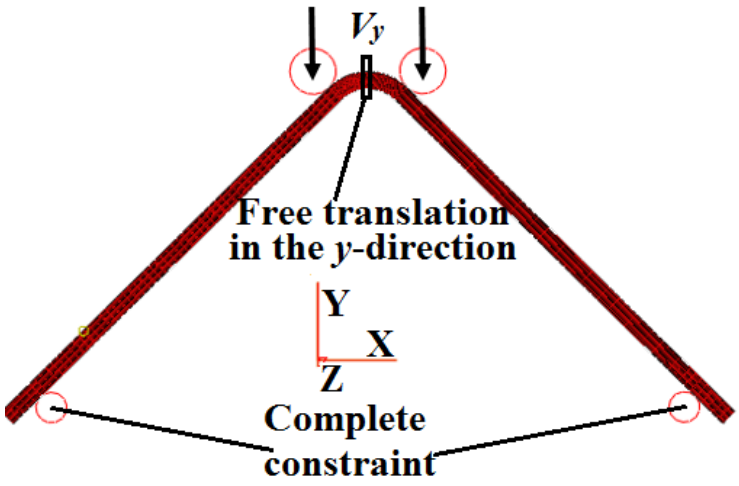

Figure 2-28 Finite element model of a four-point bending test.

2.4.4 Results and discussion

The experimentally observed position of actual delamination almost coincided with that of FEM-derived maximum radial stress (Figure 2-29), with the corresponding load-displacement relationships as shown in Figure 2-30. The propagation of the first macroscopic delamination was instantaneous, inducing a first peak load and a sudden decrease of macroscopic rigidity. The stress distribution of the L-shaped specimen including interlaminar tensile stress (S22) and interlaminar shear stress (S12) is as shown in Figure 2-31.

The interlaminar tensile strength experimentally determined as described elsewhere [96] equaled to 55.6 MPa, and its variation almost coincided with the experimental scattering range (coefficient of variation = 7.1%), whereas finite element simulation afforded a value of 53.4 MPa. Thus, the difference between the values obtained by these different methods was only 2.2 MPa, as illustrated in Figure 2-32, showing that finite element simulation can be utilized as a reference method.

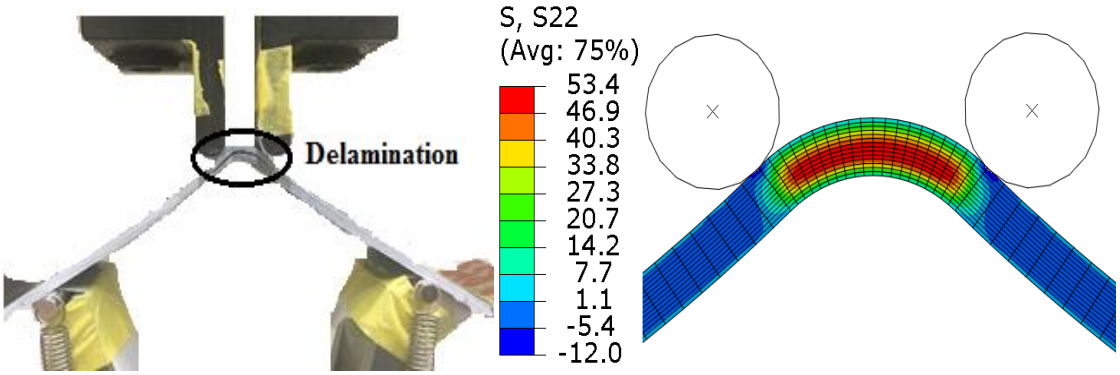

Figure 2-29 Delamination in four-point bending tests (left) and FEM-derived radial stress distribution (right)

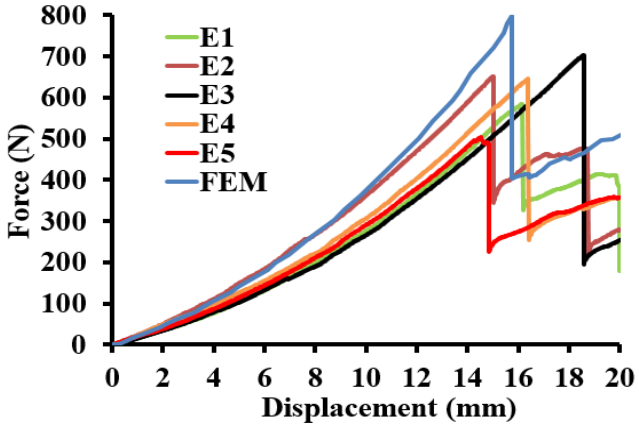

Figure 2-30 Experimental and simulated load-displacement relationships

2. Interlaminar behavior of UT-CTT

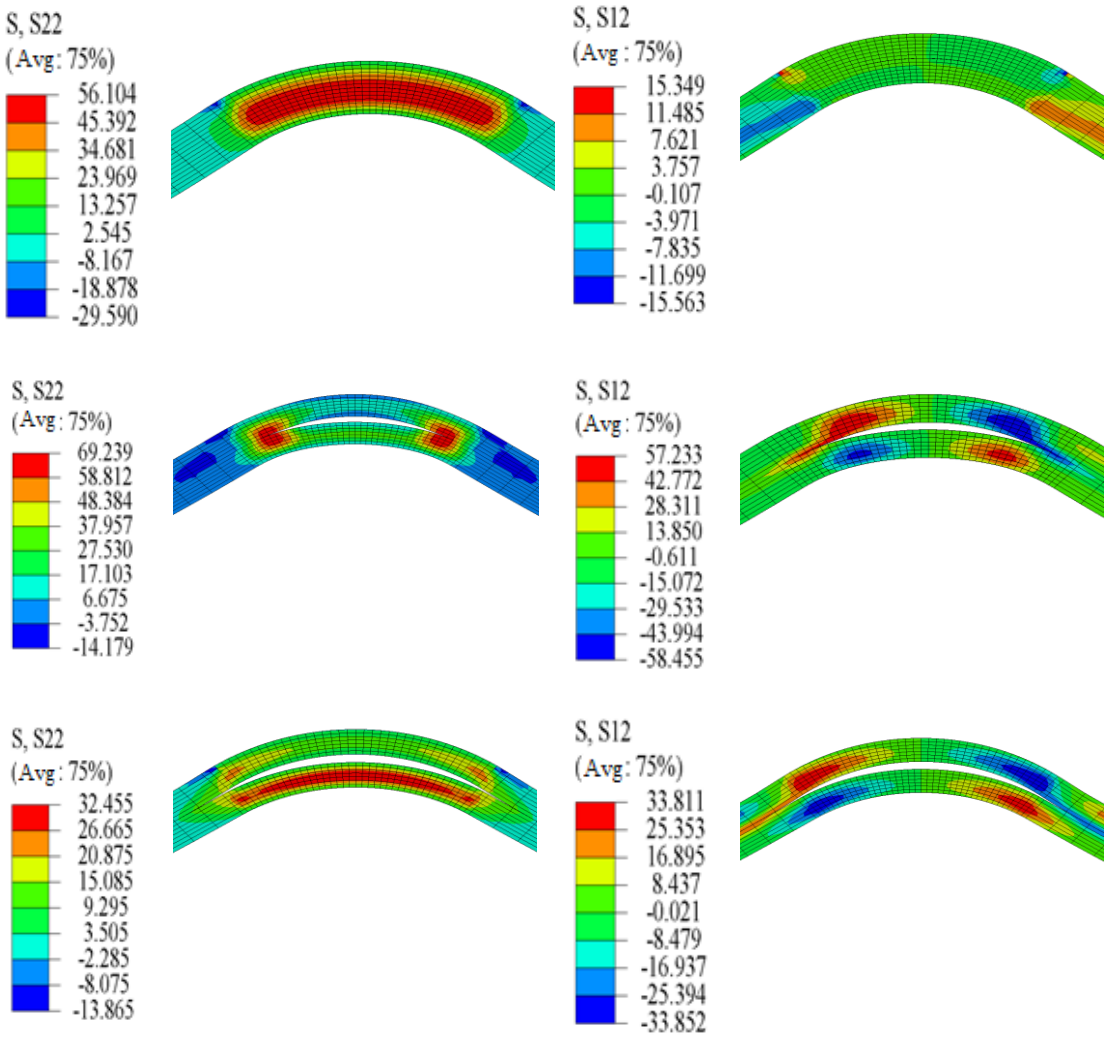

Figure 2-31 Stress distribution of interlaminar tensile (S22) and shear (S12) stress

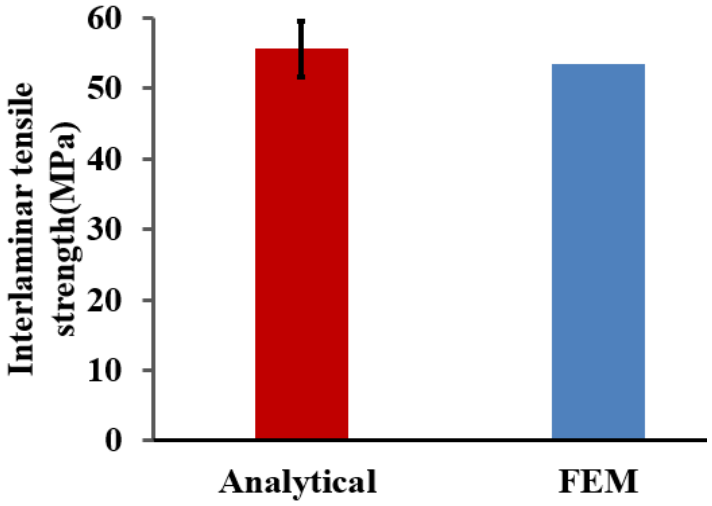

Figure 2-32 Analytical and simulated interlaminar tensile strength

2.5 Concluding remarks

This chapter describes a theoretical, experimental and numerical study to investigate two representative cases of delamination in UT-CTT: delamination in a double cantilever beam (Mode I); delamination in an end notched flexure (Mode II) and developed a modelling technique to express the delamination behavior of UT-CTT L-shaped structure.

(1) Out-of-plane mechanical properties of UT-CTT including interlaminar fracture toughness and interlaminar tensile strength were determined by using experimental and numerical analysis. In examples of mode I delamination, unstable crack growth resulted in saw-tooth like load-displacement curves after the initial stage of increasing load for all UD, UT-CTT and CP specimens. Besides, all of the specimens exhibited the stable crack propagation for UD ENF specimens, whereas both stable and unstable crack propagation phenomenon could be observed for UT-CTT and CP ENF specimens.

(2) The considered analytical approach worked well for UT-CTT to determine the Mode I and Mode II fracture toughness. An analysis model based on linear elastic fracture mechanics was used to obtain the initiation critical energy release rate $G_{Ic,initiation}$ (average value 2.65 N/mm) and the propagation critical energy release rate $G_{Ic,propagation}$ (average value 3.45 N/mm) because of unstable crack propagation during DCB tests. For ENF tests, a value of 2.95 N/mm for $G_{IIc,initiation}$ and 5.04 N/mm for $G_{IIc,propagation}$ were found using beam theory in reference to JIS K 7086 standard.

(3) The crack front of DCB specimens presented nearly straight, enabling the application of the cohesive zone model in FEM, and the unexpected stable crack propagation for ENF specimens results from the matrix extension which resists crack growth.

(4) A computationally efficient model using surface-based cohesive zone model with triangular CZM law was developed for predicting delamination behavior of UT-CTT and validated by experimental and analytical methods. For DCB tests, the numerical results with minimum and maximum critical strain energy release rate values define a range in which analytical and experimental results can fit well. Moreover, for ENF tests, a combination of interfacial shear strength and friction show a value of 20% influence on force-displacement, and the numerical results could achieve good correlation with the experimental results by choosing appropriate parameters.

(5) An accurate method for estimating the interlaminar tensile strength was presented by analysis of four-point bending test of L-shaped specimen and finite element simulation results, revealing that the failure of these commonly used structures was due to the sudden and instantaneous propagation of delamination in the curved section. The accuracy of finite element simulations was demonstrated by comparing simulated load-displacement relationships and interlaminar tensile strengths with experimental data.

Therefore, the proposed method can accurately determine the interlaminar fracture toughness and interlaminar tensile strength of UT-CTT, allowing engineers to improve their designs by relying on an integrated consideration of in- and out-of-plane strengths of composite materials.

3. Fracture behavior of UT-CTT hat-shaped hollow beam under static and impact loadings

3.1 Introduction

This chapter will experimentally and numerically describe fracture behaviors of UT-CTT hat-shaped hollow beam under transverse static and impact loadings. The experiments in this chapter were finished by collaborating with Mr. Xiao [97-99]. The numerical model was to incorporate some hypothetical inter-layers in UT-CTT and assign them with the failure model as a cohesive zone model, which can perform non-linear characteristics with failure criterion for representing delamination failure. The dynamic material parameters for the model were theoretically predicted by considering the effect of strain-rate dependency. The damage mode predicted by FEM agreed well with that of experimental results. It shows that the proposed modelling approach for interacting damage modes can serve as a benchmark for modelling damage coupling in composite materials.

3.2 Manufacturing process

The preparation process of UT-CTT hat-shaped hollow beam was described in Figure 3-1. Firstly, the UD prepreg sheets were cut into tapes measured 19 mm in length, 5 mm in width, 44 μm in thickness. After that, the chopped tapes were dispersed randomly by hand on a PTFE sheet. Although the specimen made by hand dispersion may cause lower mechanical property comparing with the one made by water dispersion, the limitation of molding size makes manufacturing of intermediate sheer by water dispersion method impossible. In the next step, the randomly dispersed tapes were heated and pressed with 5 MPa, 255 ℃ within 5 s. Then, the obtained UT-CTT intermediate sheet measured 400 mm in length, 250 mm in width, 0.16 mm in thickness were stacked to produce hat-shaped and panel parts. Finally, the hat-shaped hollow

beam was assembly by ultrasonic welding for transverse static tests and rivet joints (Figure 3-2) for impact tests.

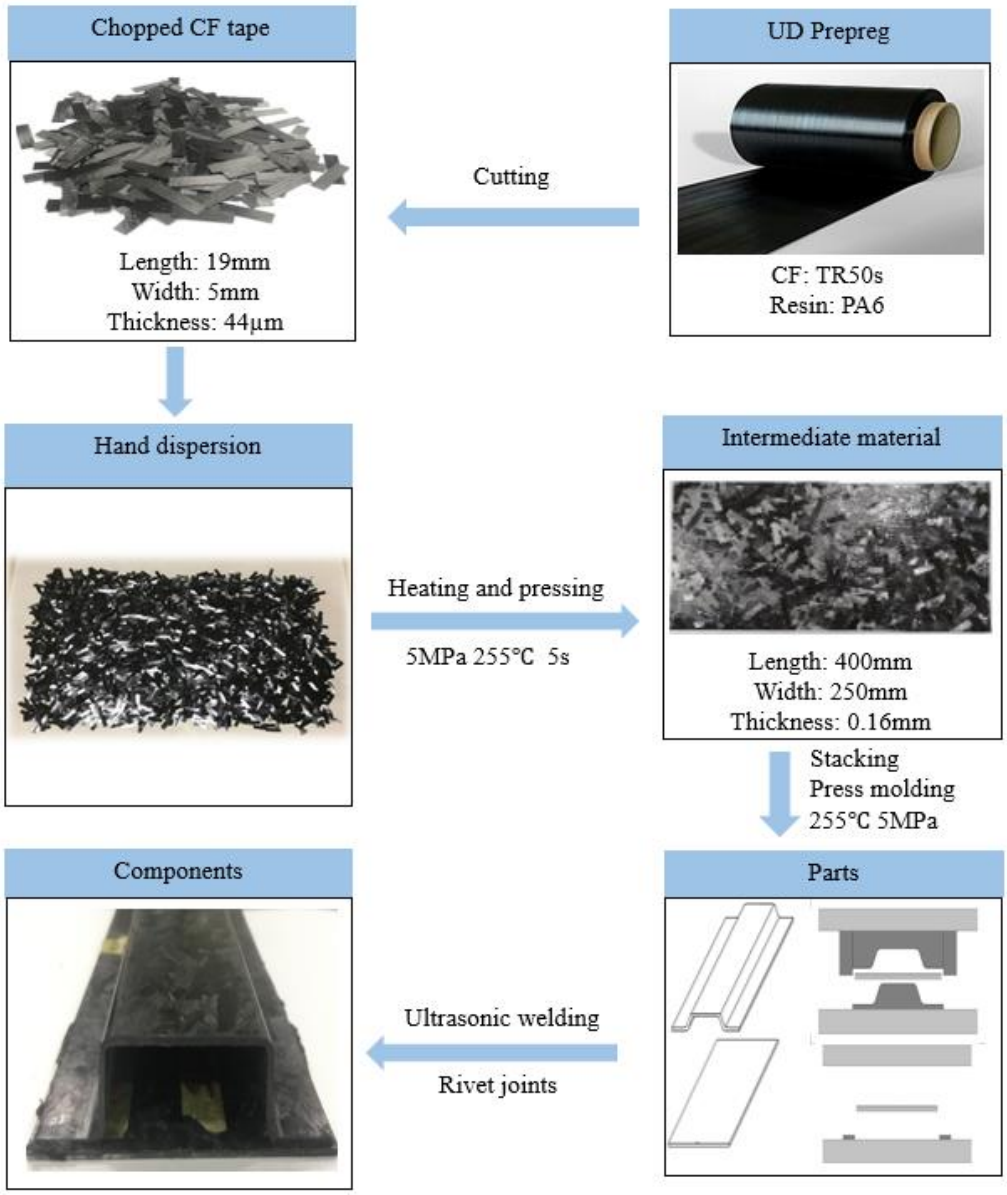

Figure 3-1 Preparation process of UT-CTT hat-shaped hollow beam

Figure 3-2 Rivet joints for assembling hat-shaped hollow beam

3.3 Fracture behavior of UT-CTT hat-shaped hollow beam under transverse static loading

3.3.1 Experimental investigation

The hat-shaped hollow beam was subjected to standardized three-point bending tests (Figure 3-3), with the radii of cylindrical loading bars (R_1) and cylindrical support bars (R_2) equaling to 75 mm and 15 mm, respectively. The span was 370 mm. All three-point bending tests were performed using a universal test machine (AUTOGRAPH AGS-10kN, Shimadzu Corp., Japan), and cylindrical loading bars were moved at a speed of 1 mm min^{-1} as shown in Figure 3-4. The dimensions of the hat-shaped hollow beam and test setup are as shown in Table 3-1.

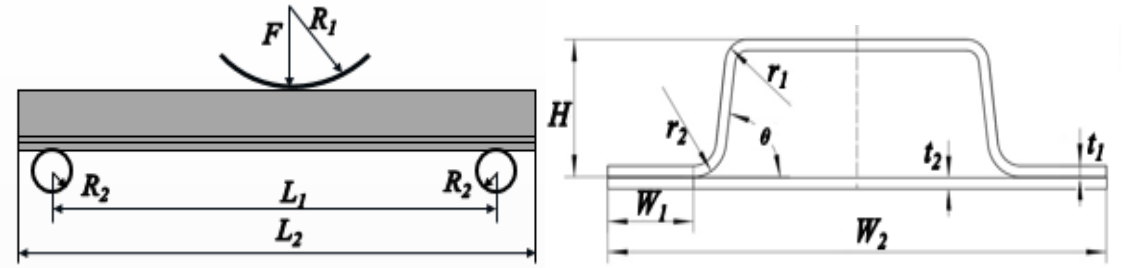

Figure 3-3 Schematic diagram of a three-point bending test and specimen.

Figure 3-4 Three-point bending test for hat-shaped hollow beam

Table 3-1 Dimensions of hat-shaped hollow beam and test setup

(mm)	W_1	W_2	H	t_1	t_2	r_1	r_2	θ	L_1	L_2	R_1	R_2
	18	100	26	2	2	5	7.5	83°	370	400	75	15

3.3.2 Finite Element Analysis

3.3.2.1 Composite material models and failure criterion

Several constitutive material models for composite structures can be implemented in Altair RADIOSS 14.0 [100], such as LAW12 and LAW25, etc. The LAW12 can be used in solid and shell elements, whereas LAW25 is only available for shell elements. Therefore, the material model LAW12 was used for 3D modelling of the UT-CTT hat-shaped hollow beam. Damage initiation and evolution should be considered to predict the fracture behavior of the UT-CTT hat-shaped hollow beam.

3.3.2.1.1 Damage initiation criterion

Damage initiation means the onset of degradation at a material point, and Hashin failure criteria[101] was employed to simulate damage initiation. Two types of failure models are available: unidirectional lamina model and fabric lamina model, when /FAIL/HASHIN is input in Altair RADIOSS 14.0.

(1) Unidirectional lamina model:

Tensile/shear fiber mode:

$$F_1 = \left(\frac{\sigma_{11}}{X_T}\right)^2 + \frac{\sigma_{12}^2+\sigma_{13}^2}{\left(\sigma_{12}^f\right)^2} - 1 = \begin{cases} \geq 0 & failure \\ < 0 & no\ failure \end{cases} \quad \textbf{Equation 3-1}$$

Compression fiber mode:

$$F_2 = \left(\frac{\langle \sigma_a \rangle}{X_C}\right)^2 - 1 = \begin{cases} \geq 0 & failure \\ < 0 & no\ failure \end{cases}, \sigma_a = -\sigma_{11} + \left(-\frac{\sigma_{22}+\sigma_{33}}{2}\right) \quad \textbf{Equation 3-2}$$

Crush mode:

$$F_3 = \left(\frac{\langle p \rangle}{\sigma_c}\right)^2 - 1 = \begin{cases} \geq 0 & failure \\ < 0 & no\ failure \end{cases}, p = -\frac{\sigma_{11}+\sigma_{22}+\sigma_{33}}{3} \quad \textbf{Equation 3-3}$$

Failure matrix mode:

$$F_4 = \frac{\langle \sigma_{22} \rangle^2}{Y_T^2} + \frac{\sigma_{23}^2}{\left(\sigma_{23}^m\right)^2} + \frac{\sigma_{12}^2}{(\sigma_{12}^m)^2} - 1 = \begin{cases} \geq 0 & failure \\ < 0 & no\ failure \end{cases} \quad \textbf{Equation 3-4}$$

Delamination mode:

$$F_5 = S_{del}^2 \left[\left(\frac{\sigma_{33}}{Y_T}\right)^2 + \left(\frac{\sigma_{23}}{\sigma_{23}^m}\right)^2 + \left(\frac{\sigma_{13}}{\sigma_{13}^m}\right)^2\right] - 1 = \begin{cases} \geq 0 & failure \\ < 0 & no\ failure \end{cases} \quad \textbf{Equation 3-5}$$

(2) Fabric lamina model:

Tensile/shear fiber mode:

$$F_1 = \left(\frac{\sigma_{11}}{X_T}\right)^2 + \frac{\sigma_{12}^2+\sigma_{13}^2}{\left(\sigma_{12}^f\right)^2} - 1 = \begin{cases} \geq 0 & failure \\ < 0 & no\ failure \end{cases} \quad \textbf{Equation 3-6}$$

$$F_2 = \left(\frac{\langle\sigma_{22}\rangle}{Y_T}\right)^2 + \frac{\sigma_{12}^2+\sigma_{23}^2}{\left(\sigma_{12}^f \frac{Y_T}{X_T}\right)^2} - 1 = \begin{cases} \geq 0 & failure \\ < 0 & no\ failure \end{cases} \quad \textbf{Equation 3-7}$$

Compression fiber mode:

$$F_3 = \left(\frac{\langle\sigma_a\rangle}{X_C}\right)^2 - 1 = \begin{cases} \geq 0 & failure \\ < 0 & no\ failure \end{cases}, \sigma_a = -\sigma_{11} + (-\sigma_{33}) \quad \textbf{Equation 3-8}$$

$$F_4 = \left(\frac{\langle\sigma_b\rangle}{Y_C}\right)^2 - 1 = \begin{cases} \geq 0 & failure \\ < 0 & no\ failure \end{cases}, \sigma_b = -\sigma_{22} + (-\sigma_{33}) \quad \textbf{Equation 3-9}$$

Crush mode:

$$F_5 = \left(\frac{\langle p\rangle}{\sigma_c}\right)^2 - 1 = \begin{cases} \geq 0 & failure \\ < 0 & no\ failure \end{cases}, p = -\frac{\sigma_{11}+\sigma_{22}+\sigma_{33}}{3} \quad \textbf{Equation 3-10}$$

Shear failure matrix mode:

$$F_6 = \frac{\sigma_{12}^2}{(\sigma_{12}^m)^2} - 1 = \begin{cases} \geq 0 & failure \\ < 0 & no\ failure \end{cases} \quad \textbf{Equation 3-11}$$

Delamination mode:

$$F_7 = S_{del}^2\left[\left(\frac{\sigma_{33}}{t_n}\right)^2 + \left(\frac{\sigma_{23}}{\sigma_{23}^m}\right)^2 + \left(\frac{\sigma_{13}}{\sigma_{13}^m}\right)^2\right] - 1 = \begin{cases} \geq 0 & failure \\ < 0 & no\ failure \end{cases} \quad \textbf{Equation 3-12}$$

where X_T is the longitudinal tensile strength, Y_T is the transverse tensile strength, X_C is the longitudinal compressive strength, Y_C is the transverse compressive strength, t_n is the interlaminar tensile strength, σ_c is the crush strength, σ_{12}^f is the fiber shear strength, σ_{12}^m is the matrix shear strength in the 12-direction, σ_{23}^m is the matrix shear strength in the 23-direction, σ_{13}^m is the matrix shear strength in the 13-direction, S_{del} is delamination criteria scale factor.

3.3.2.1.2 Damage evolution criterion

Once damage initiation occurs in an integration point, damage evolution will begin. In the process of damage evolution, ultimate failure is determined by maximum plastic work or maximum strain values in Altair RADIOSS 14.0.

3.3.2.2 Finite element model

UT-CTT hat-shaped hollow beam was designed by using 3D FEM in Altair RADIOSS 14.0 as shown in Figure 3-5. The thickness of the hat-shaped and the panel part was both 2 mm. Element number with 14 in thickness which is the same as the number of layers in the actual specimen, was established with consideration of mesh dependence. It is assumed that the out-of-plane properties of the welding layer were large enough since the interface by welding was consolidated through the process of heating up, compressive pressing, and cooling down in the same way as the manufacturing process of the consolidation of randomly oriented chopped tapes. Welding layer between the hat-shaped and the panel part was connected by using tie constraint, whereas the failure behavior of the main layers was defined to comply with Hashin failure criteria. The material model LAW12, accompanying with /FAIL/HASHIN, was applied to the main layers of the UT-CTT hat-shaped hollow beam.

The cylindrical loading bar and cylindrical support bars have rigid body property. And, the cylindrical loading bar was assigned with a constant speed $V_z = 1\ \text{mm min}^{-1}$ in the vertical direction and detected the reactive force influenced by the deformation of the hollow beam, whereas the cylindrical support bars were fixed. Contacts between cylindrical bars and the hat-shaped hollow beam were treated as surface-to-surface contacts. The element size in the contact sections was chosen to be small for obtaining a more accurate stress distribution, being increased in the other parts to reduce computational time. The mechanical properties used for hat-shaped hollow beam simulation analysis are as shown in Table 3-2. After numerical computation, the post-processing built an animation of deformation and fracture behavior of the hat-shaped hollow beam and also output the contact force and the displacement.

Table 3-2 Mechanical properties of UT-CTT hat-shaped hollow beam

E_1 (GPa)	E_2 (GPa)	E_3 (GPa)	μ_{12}	G_{12} (GPa)	G_{13} (GPa)	G_{23} (GPa)
34.0	34.0	7.33	0.24	15.36	0.84	0.84

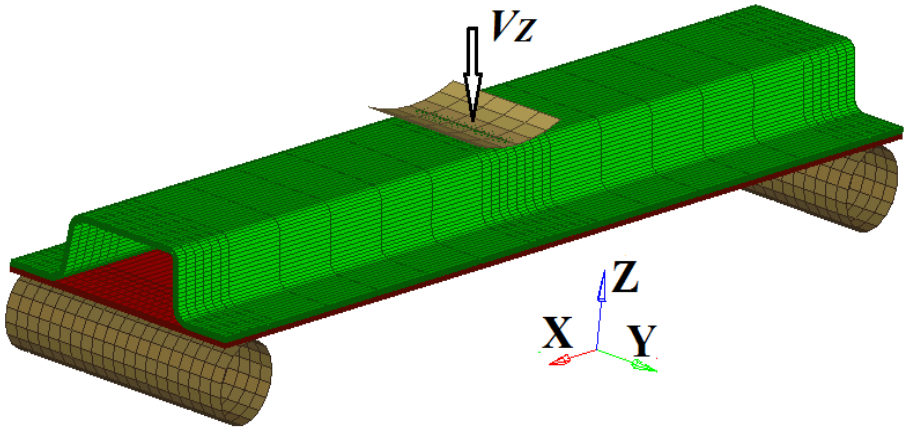

Figure 3-5 Finite element model of hat-shaped hollow beam under transverse static loading

3.3.3 Results and discussion

Figure 3-6 shows the load-displacement curve of experimental results under transverse static loading. The bending load increases to the first peak, and then progressive failure mode was observed as follows:

1) Crack initiation: The crack initiates at the corners of the top wall of the hat-shaped part due to compressive stress concentration, and it is characterized by the severe local fragmentation of fiber and matrix (Figure 3-7).

2) Crack propagation: The cracking region spreads towards the symmetric axis at the top wall of the hat-shaped part and towards the overlap area at the side wall. Simultaneously, the corners of the top wall of the hat-shaped part begin to crush, and the top and side wall start buckling (Figure 3-8).

3) Tensile failure: The crack starts growing in the overlap area and the bottom panel, and the load decreased slowly (Figure 3-9).

As shown in Figure 3-10, damage propagation in FEM using Hashin failure criteria shows a similar tendency with that in the experiments. Meanwhile, the stress distribution in the longitudinal direction of the hat-shaped hollow beam also shows same damage propagation mode which can be visualized in Figure 3-11.

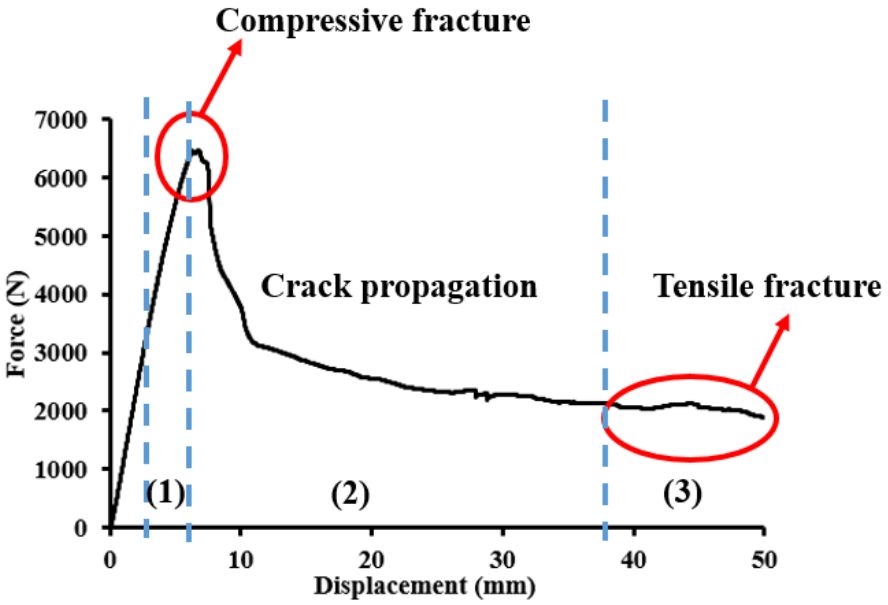

Figure 3-6 Load-displacement curve of experimental results under transverse static loading

Figure 3-7 Fracture process: compressive fracture

Figure 3-8 Fracture process: crack propagation

Figure 3-9 Fracture process: tensile failure

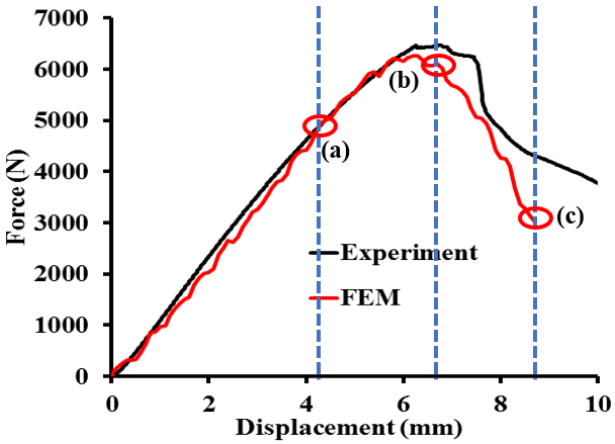

Figure 3-10 Load-displacement curves of FEM and experiment under transverse static loading

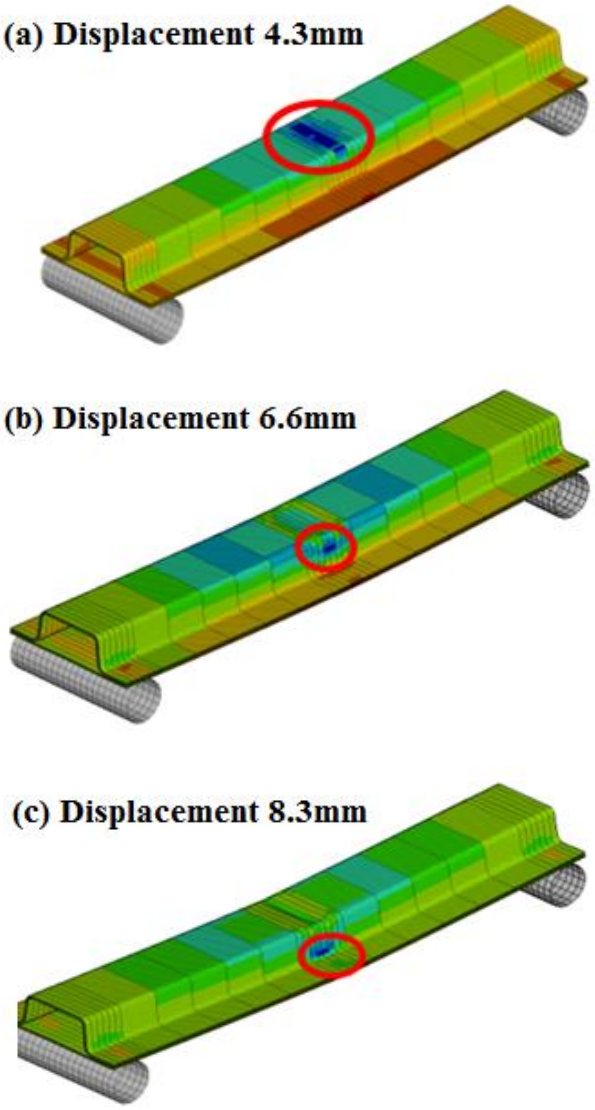

Figure 3-11 Stress distribution of FEM under transverse static loading

3.4 Fracture behavior of UT-CTT hat-shaped hollow beam under impact loading

3.4.1 Experimental investigation

The drop-weight impact test machine was developed to evaluate the crashworthiness of the hat-shaped hollow beam under impact loading condition. The 9250 impact testing system (Figure 3-12), which comprises Instron dynatup drop tower impact testers (Figure 3-13), system controller, impulse data acquisition software, impulse signal conditioning unit, national instruments data acquisition card, was used. Figure 3-14 shows a photograph of the drop-weight impact test machine and schematic diagram of the jig for three-point bending test. The dimensions of test setup are same as that in transverse static tests. The diameter of the impactor and the supporters are both 16 mm, and the span is set to 170 mm. Two springs were compressed using a chain block and launched the drop-weight assembly when the trigger was actuated to increase both the acceleration of the impactor and impact energy. Impact energy of the test machine was set to higher than the energy absorption capability of the specimen in order to study the collapse mechanism of the hat-shaped hollow beam at a high strain rate. The mass of the drop-weight assembly was 10 kg, and the maximum impact velocity of the impactor before it reaches the specimen can be controlled by changing the compression length of the springs. During the tests, a high-speed camera (Photron SA1.1) was used to record the whole fracture process.

After the tests, a digital filtering method was used to suppress signal distortion induced by impactor ringing, which is a well-known and inevitable problem of a drop-weight tester. The “ringing” oscillations generally occur at higher frequencies than the oscillations generated by the specimen. The process of multi-filtering with a lower pass filter can be found in Appendix 1.

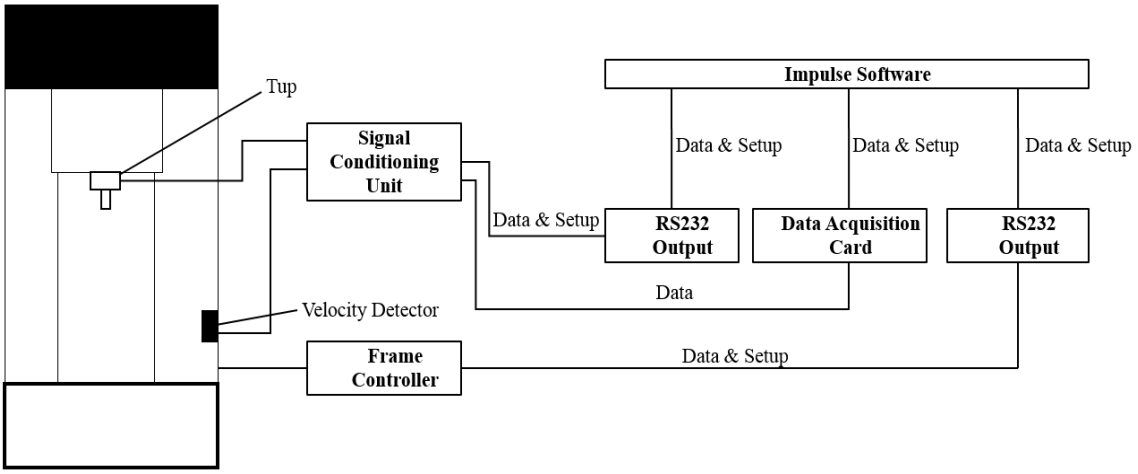

Figure 3-12 The 9250 impact testing system

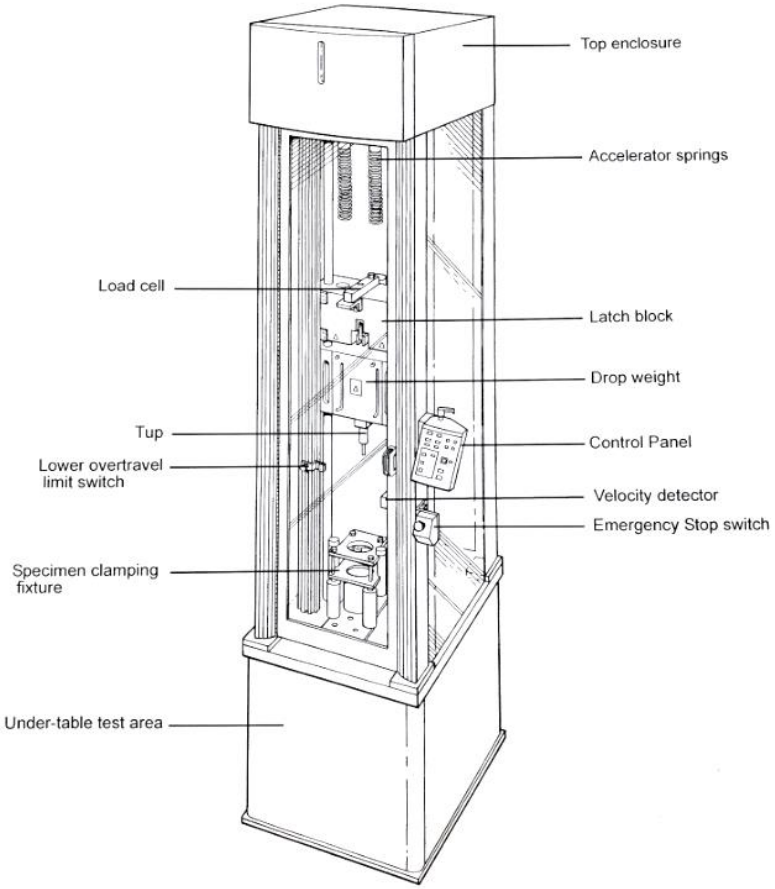

Figure 3-13 Instron dynatup drop tower impact testers

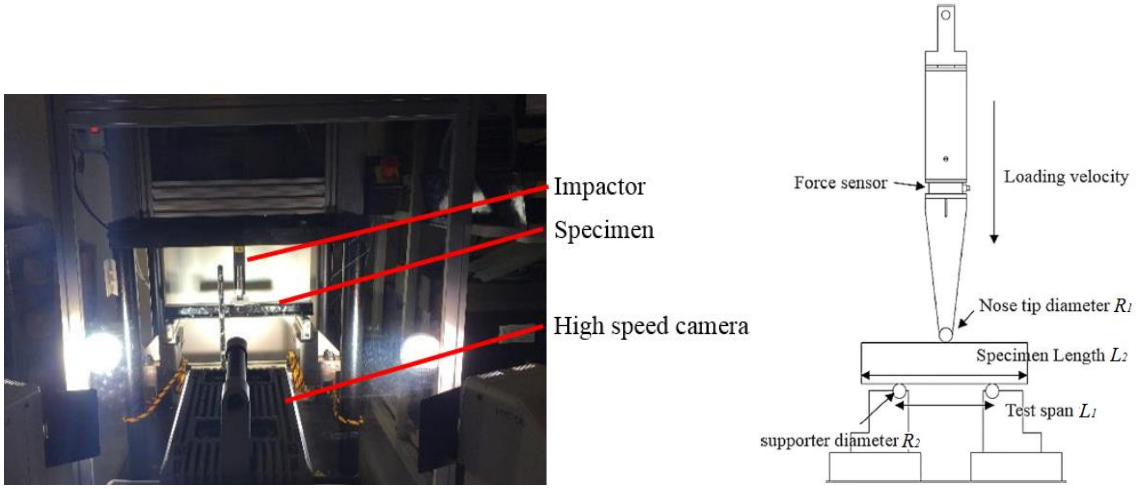

Figure 3-14 Photograph of drop-weight impact test machine (left) and schematic diagram of jig for three-point bending test (right)

3.4.2 Finite Element Analysis

3.4.2.1 Theoretical prediction of UT-CTT dynamic mechanical properties

In order to obtain the strength of UT-CTT with consideration of strain rate dependence, the impact tests were carried out [102]. Figure 3-15 shows the relationship between impact velocity and impact strength of the experimental results. The relationship between impact strength and strain rate formulates a double logarithmic linear function as shown in Figure 3-16, which means the dynamic strength of UT-CTT can be predicted from the reference static strength. Therefore, the strength at the velocity of 8.5 m/s was about 1.38 times than that at the static velocity. Moreover, it is assumed that the theoretical relationship derived based on Dow's theory [103] can be used for the prediction of dynamic properties of UT-CTT. Therefore from the Equation 3-13, the modulus of the matrix in the impact case was about 1.90 times than that at the static one.

$$\frac{\sigma_{Bf}(R)}{\sigma_{Bf}(R_0)} = \left[\frac{E_m(R)}{E_m(R_0)}\right]^{\frac{1}{2}} \qquad \textbf{Equation 3-13}$$

where $\sigma_{Bf}(R)$ is the dynamic compressive strength, R is strain rate, $\sigma_{Bf}(R_0)$ is the standard compressive strength, R_0 is the standard strain rate, $E_m(R)$ is the dynamic matrix elastic modulus, $E_m(R_0)$ is the standard matrix elastic modulus.

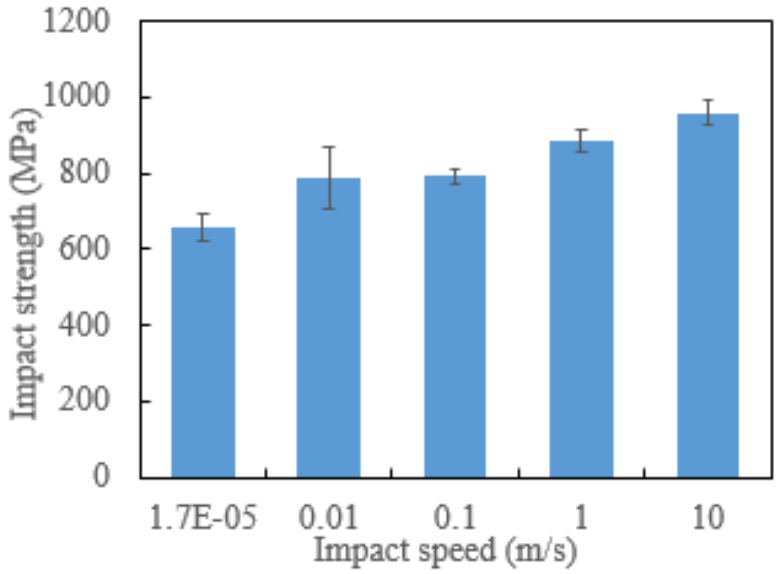

Figure 3-15 The relationship between impact velocity and impact strength of UT-CTT

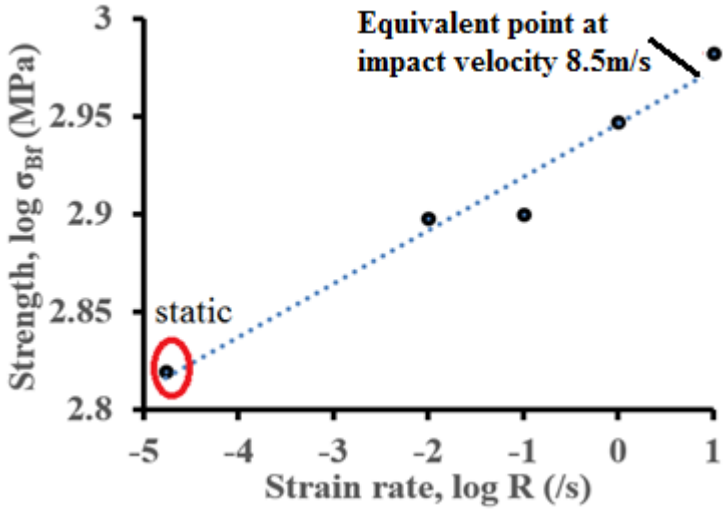

Figure 3-16 Comparison of experiments and prediction of the strength of UT-CTT

The ratio of dynamic to static parameters is called 'scaling factor'[47]. The in-plane elastic moduli of UT-CTT are primarily influenced by the modulus of fiber, so the scaling factor is set to 1.0 for the prediction of dynamic in-plane elastic moduli. However, the following mechanical properties of UT-CTT are influenced by the modulus of the matrix and the scaling factor can be 1.90 as is the same as that of the matrix: (1) The out-of-plane moduli of UT-CTT. From the Equation 3-14 [47], the out-of-plane moduli of UT-CTT are primarily influenced by the modulus of the matrix. (2) The out-of-plane tensile and shear strength. It is noted that the yield stresses of the matrix have significant influence on that in the out-of-plane shear and normal directions. (3) The tensile

strength. The tensile strength might be determined by the out-of-plane shear yield stress of UT-CTT, which means that the tensile strength of UT-CTT also shows strain-rate dependence since the in-plane tensile failure is mainly caused by the inter-layer slip of chopped tapes rather than the fracture of tapes themselves. (4) The in-plane tensile fracture strain. The in-plane tensile fracture strain can be calculated by dividing in-plane tensile strength by in-plane elastic modulus. (5) The in-plane shear strength and its fracture strain. It is noted that the in-plane shear strength and its fracture strain can be influenced by the modulus of the matrix due to the brittle fracture. However, for the determination of the out-of-plane tensile and shear fracture strain, there was no experimental data to show the relationship of strain-rate dependence of the out-of-plane fracture strain, so the dynamic out-of-plane fracture strain is set as static one based on the assumption that the value of the dynamic out-of-plane fracture strain should never exceed the static one. It is noted that the strain-rate dependence of the out-of-plane fracture strain should be accurately determined using analytical or experimental methods in the future.

$$E_3 = E_m \frac{1 + \xi \frac{E_f/E_m - 1}{E_f/E_m + \xi} V_f}{1 - \xi \frac{E_f/E_m - 1}{E_f/E_m + \xi} V_f} \qquad \textbf{Equation 3-14}$$

E_m and E_f represent the elastic moduli of matrix and fiber, respectively; V_f is carbon fiber volume fraction; ξ is a measure of reinforcement geometry which depends on loading conditions.

The dynamic stress-strain curves were estimated from the static ones based on the schematic relationships as shown in Figure 3-17. For determination of in-plane dynamic material properties, the value of 1.90 was set as the scaling factor of the in-plane tensile, compressive and shear strengths, and the scaling factor of the in-plane moduli was set as 1.0. Besides, in order to determine the dynamic out-of-plane properties, the scaling factor of the out-of-plane moduli, normal and tangential strengths were assumed to be 1.90 as mentioned above, and the dynamic out-of-plane fracture strain was assumed as same as static one. From these assumptions and predictions, the dynamic material properties were summarized as indicated in Table 3-3. It is worth noting that the damage propagation criterion for delamination failure is that once the critical distance between points initially in contact is reached, the interface failure is complete. Therefore, dynamic fracture toughness was not listed here, although strain rate dependence of fracture toughness should also be taken into account.

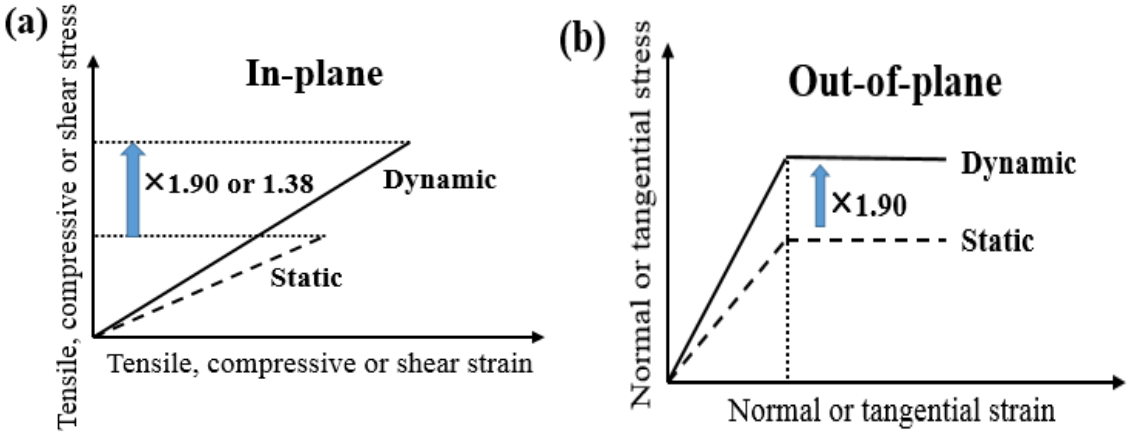

Figure 3-17 Determination of dynamic (a) In-plane (b) Out-of-plane material properties

Table 3-3 Static and dynamic mechanical properties

	Parameter		Static (1.7×10^{-5} m/s)	Dynamic (8.5 m/s)
	Elastic Modulus (GPa)	E_1	34.0	34.0
		E_2	34.0	34.0
		E_3	7.33	13.93
	Shear Modulus (GPa)	G_{12}	16.7	16.7
		G_{13}	1.08	2.05
		G_{23}	1.08	2.05
In-plane	Tensile strength (MPa)	X_T,Y_T	403	765.7
	Tensile fracture strain (%)	ε_T	0.7	1.33
	Compressive strength (MPa)	X_C,Y_C	280	532
	Compressive fracture strain (%)	ε_C	0.6	1.14
	Shear strength (MPa)	X_S	170	323
	Shear fracture strain (%)	ε_S	1.31	2.49
Out-of-plane	Tensile strength (MPa)	t_n	55.6	105.64
	Tensile fracture strain (%)	ε_n	0.7	0.7
	Shear strength (MPa)	t_s	30	57
	Shear fracture strain (%)	ε_s	17	17

3.4.2.2 Finite element model

3.4.2.2.1 Composite material model and contact in LS_DYNA

The simulated material behavior is governed by the material model. The input parameters to the material model are defined in the material card, which usually includes some elastic anisotropic material properties, material coordinate definitions and other model parameters such as failure criterion. Each material model adopts a different model strategy for failure initiation prediction, material properties, and degradation schemes.

Constitutive models for composite structures can be implemented in LS_DYNA [104], such as MAT22(MAT_COMPOSITE_DAMAGE),MAT54/55(MAT_ENHANCED_COMPOSITE_DAMAGE), MAT59 (MAT_COMPOSITE_FAILURE_OPTION_MODEL). The material model MAT22 can be used in solid and shell elements and proposed by Chang-Chang. The material model MAT54/55 can be used for thin shells. In MAT54/55 an elastic-plastic stress-strain behavior is used, allowing a more ductile failure process. The stress is increased linearly until the failure criteria are reached in one mode. Then the stress-strain behavior is either ideal plastic or the maximum stress is reduced to a residual stress, depending on how certain parameters are defined in the material card. The integration point in a certain layer is removed when a specified failure strain is reached [105]. MAT54 makes use of the full Chang-Chang failure criteria where failure can occur in tensile fiber mode, compressive fiber mode, tensile matrix mode and compressive matrix mode. In MAT55, the tensile and compressive fiber mode is treated as in the Chang-Chang failure criterion, but for the matrix modes, the Tsai-Wu criteria are used instead. And these two failure criteria can be controlled with the CRIT parameter in the MAT54/55 material card. The material model MAT59, which applied for shell and solid elements and based on faceted failure surface and ellipsoidal failure surface, can be used for the material progressive failure criterions which include longitudinal and transverse directions in tension and compression respectively, and through-thickness direction in compression and shear [106]. Among MAT59, MAT_COMPOSITE_FAILURE_SOLID model is based on maximum stress criteria which include in-plane and out-of-plane tensile, compressive and shear strength.

The Chang-Chang criteria in MAT 54 is given as follows:

Tensile fiber mode:

$$\left(\frac{\sigma_{11}}{X_T}\right)^2 + \bar{\tau} = 1 \qquad \textbf{Equation 3-15}$$

Compressive fiber mode:

$$\left(\frac{\sigma_{11}}{X_C}\right)^2 = 1 \qquad \textbf{Equation 3-16}$$

Tensile matrix mode:

$$\frac{(\sigma_{22})^2}{Y_T} + \bar{\tau} = 1 \qquad \textbf{Equation 3-17}$$

Compressive matrix mode:

$$\frac{(\sigma_{22})^2}{2X_S} + \left[\left(\frac{Y_C}{2X_S}\right)^2 - 1\right]\frac{\sigma_{22}}{Y_C} + \bar{\tau} = 1 \qquad \textbf{Equation 3-18}$$

MAT55 uses Tsai-Wu failure criteria for compressive and tensile matrix failure modes as follows:

$$\frac{(\sigma_{22})^2}{Y_C Y_T} + \left(\frac{\sigma_{12}}{X_S}\right)^2 + \frac{(Y_C - Y_T)\sigma_{22}}{Y_C Y_T} = 1 \qquad \textbf{Equation 3-19}$$

The ellipsoidal failure surface in MAT59 is shown as follows:

$$f = \left(\frac{\sigma_{12}}{S_C}\right)^2 + \left(\frac{\sigma_{13}}{S_C}\right)^2 + \left(\frac{\sigma_{23}}{S_C}\right)^2 + \left[\frac{2\left(\sigma_2 - \frac{Y_T - Y_C}{2}\right)}{Y_C + Y_T}\right]^2 + \left[\frac{2\left(\sigma_1 - \frac{X_T - X_C}{2}\right)}{X_C + X_T}\right]^2 - 1 \qquad \textbf{Equation 3-20}$$

The MAT_ADD_EROSION provides failure option in the material models, which means the element will be deleted from the calculation if any one of the criterions defined here is satisfied. As shown in Table 3-4, EXCL is the exclusion number. The associated failure criteria calculations are bypassed when any of the failure constants are set to the exclusion number. MXPRES is the maximum pressure at failure. MNEPS is the minimum principle strain at failure. MNPRES is the minimum pressure at failure. SIGP1 is the principle stress at failure. SIGVM is the equivalent stress at failure. MXEPS is the maximum principle strain at failure. EPSSH is the shear strain at failure. SIGTH is the threshold stress. IMPULSE is the stress impulse for failure.

Table 3-4 Keyword card of MAT_ADD_EROSION

Variable	MID	EXCL	MXPRES	MNEPS	MNPRES	SIGPI
Type	A8	F	F	F		
Variable	SIGVM	MXEPS	EPSSH	SIGTH	IMPULSE	FAILTM
Type	F	F	F	F	F	F

In LS-DYNA models, the delamination can be modelled using tiebreak delamination contact. In the tiebreak contact, the penalty method was utilized as contact algorithm because appropriate forces can be generated to the slave nodes without generating spurious results. CONTACT_AUTOMATIC_ONE_WAY_SURFACE_TO_SURFACE_TIEBREAK contact,

which is one kind of tiebreak delamination contacts, can be established as adhesive. Normal failure stress and shear failure stress were defined in tiebreak contact card. As mentioned in Section 3.4.2.1, the relationship between the damage of the material and the distance between the two contact points is a linear function after the failure stress tiebreak criterion is met, and the contact will be broken once the critical distance is reached, finally the contact will convert into surface to surface contact to prevent penetrations. Tiebreak contact allows the separation of the surfaces under tensile loading, and the failure of the tied surfaces will occur once the following failure criterion is satisfied:

$$\left(\frac{|t_n|}{NFLS}\right)^2 + \left(\frac{|t_s|}{SFLS}\right)^2 \geq 1 \qquad \textbf{Equation 3-21}$$

where NFLS is the normal failure stress, SFLS is the shear failure stress.

For a better understanding of the contact parameter, two solid elements and two shell elements under tensile loading were investigated as shown in Figure 3-18. The dimensions of each element are 5×5×2 mm. The upper element is under vertical force and the extra five degrees of freedom were fixed, whereas all the lower element were fixed. CONTACT_AUTOMATIC_ONE_WAY_SURFACE_TO_SURFACE_TIEBREAK contact was used as the adhesive between two elements. In the card, OPTION = 6 was used in two solid elements model while OPTION = 8 in two shell elements model. For each model, the NFTS is set as 55 MPa and SFLS is 40 MPa. Figure 3-19 shows the comparison of force-time curves between two solid elements model and two shell elements model. Both models can successfully simulate the debonding process and the contact used here can be used for the following delamination simulation.

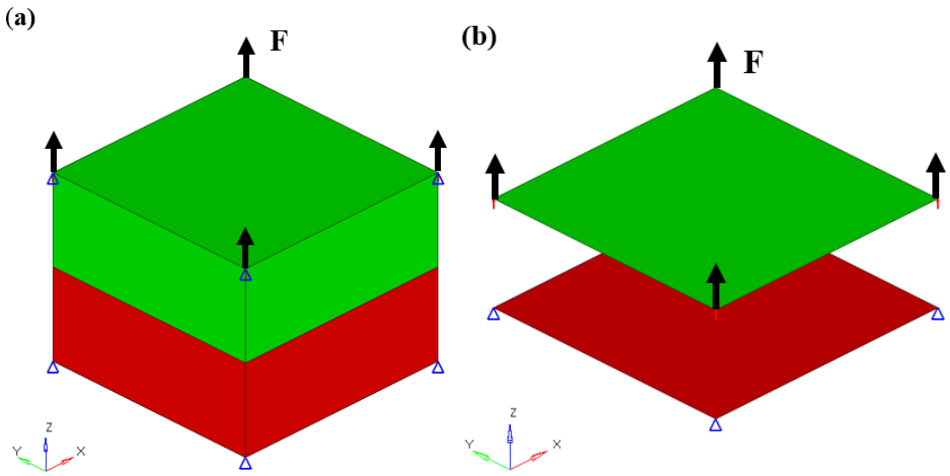

Figure 3-18 Finite element model of (a) two solid elements and (b) two shell elements under tension

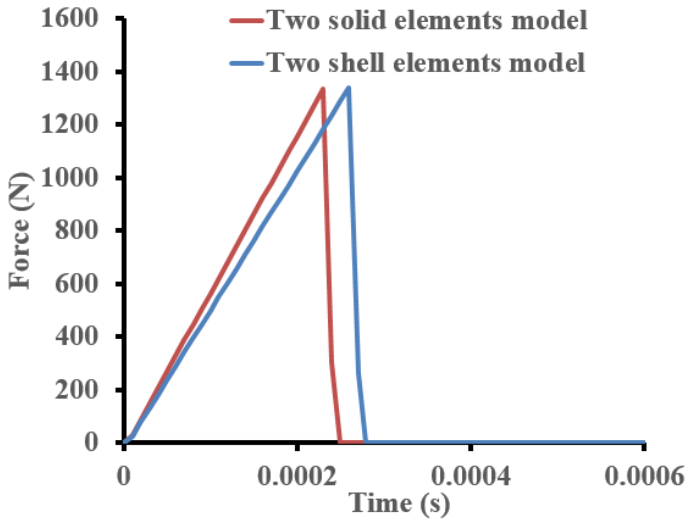

Figure 3-19 Comparison of force-time curves between two solid elements model and two shell elements model

3.4.2.2.2 Modeling details

2D shell and 3D solid finite element model were established for UT-CTT hat-shaped hollow beam as shown in Figure 3-20. In the 2D shell model, PART_COMPOSITE was defined to simulate lay-ups by defining MATID, thickness, and orientation and fully integrated shell element was used. The layers were assigned with the in-plane isotropic properties of UT-CTT using MAT54 and the parameters for the MAT54 material card are shown in Table 3-5. From the reference [107], the parameters including ALPH, BETA, FBRT, YCFAC TFAIL have the negligible effect on the simulation results, and the EFS parameter is not necessary once the DFAILT, DFAILC and

DFAILM have been defined. Moreover, XC and DFAILC are the primary parameters resulting in element failure and deletion, and the SOFT is the most important parameter for the accuracy of the simulation results, therefore the effect of the SOFT parameter on the simulation results will be studied. Welding layer between hat-shaped and panel parts was created by using CONTACT_AUTOMATIC_ONE_WAY_SURFACE_TO_SURFACE_TIEBREAK contact and the out-of-plane properties of the welding layer were large enough.

In the 3D solid model, element number with 14 in thickness, which is the same as the number of layers in the actual specimen, was established with consideration of mesh dependence as well as the delamination behavior. It is known that the out-of-plane normal and shear deformation results in the separation of chopped tapes in UT-CTT layers, which is similar with Mode I and Mode II delamination in continuous fiber reinforced composites; therefore, the model consists of stacked solid elements for the representation of intralaminar damage and cohesive interfaces for interlaminar failure. Cohesive layers and welding layer between hat-shaped and panel parts were created by using CONTACT_AUTOMATIC_ONE_WAY_SURFACE_TO_SURFACE_TIEBREAK contact and assigned with the out-of-plane properties while the main layers were assigned with the in-plane isotropic properties of UT-CTT using MAT59 and the failure behavior was defined to comply with Tsai-Wu criteria. It is assumed that the out-of-plane properties of the welding layer were large enough since the interface by rivet joints was very strong and showed no debonding during experiments.

In both models, the cylindrical loading bar and cylindrical support bars have rigid body property with material card MAT20, and the mass of 10 kg was assigned to the cylindrical loading bar. And, the initial velocity of the impactor was defined with INITIAL_VELOCITY. The movement of the impactor is vertical and the extra five degrees of freedom were fixed, whereas the cylindrical support bars were fixed. Contacts between cylindrical bars and the hat-shaped hollow beam were treated as surface-to-surface contacts with CONTACT_AUTOMATIC_ SURFACE_TO_SURFACE.

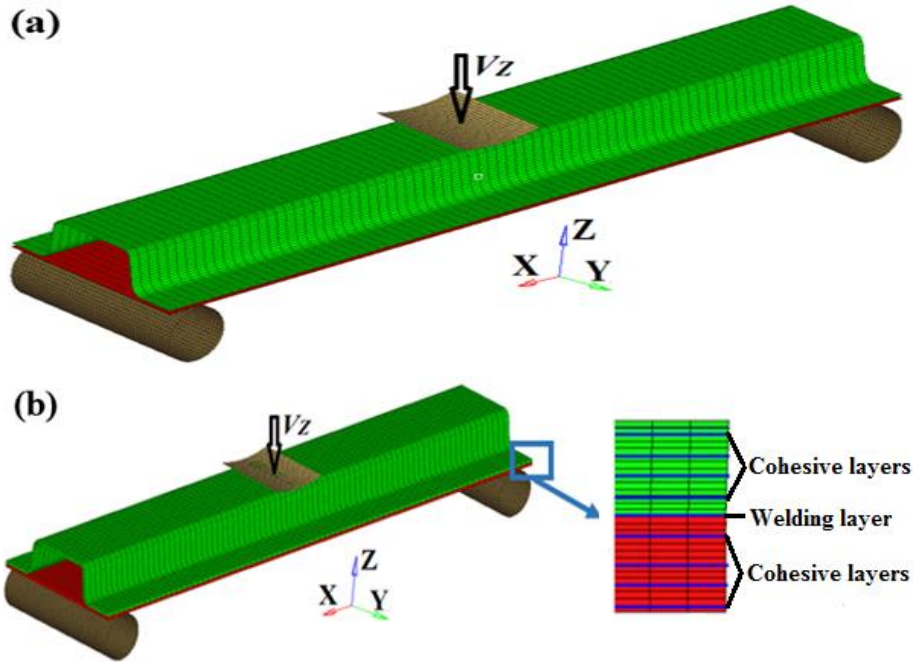

Figure 3-20 (a) 2D shell and (b) 3D solid Finite element model of hat-shaped hollow beam under impact loading

Table 3-5 Model parameters in MAT54

Parameter	Definition	Value
AOPT	Material axes option parameter	3
DFAILT	Max strain for fiber tension	0.0133
DFAILC	Max strain for fiber compression	-0.0114
DFAILM	Max strain for matrix straining in tension and compression	0.0133
DFAILS	Max shear strain	0.0249
EFS	Effective failure strain	0
TFAIL	Time step size criteria for element deletion	1e-7
ALPH	Shear stress non-linear term	0
SOFT	Softening reduction factor for strength in crush	0.5
FBRT	Softening for fiber tensile strength after matrix failure	0.95
YCFAC	Softening for fiber compressive strength after matrix failure	1.2
BETA	Weighing factor for shear term in tensile fiber mode	0
XC	Longitudinal compressive strength	-765.7
XT	Longitudinal tensile strength	765.7
YC	Transverse compressive strength	-532
YT	Transverse tensile strength	532
SC	Shear strength	323
CRIT	Failure criterion	54

3.4.3 Results and discussion

3.4.3.1 Experimental results

Figure 3-21 shows the load-displacement curve of experimental results in the static tests and impact tests at the velocity of 8.5 m/s. From the load-displacement curve of impact tests, the bending load rapidly increases to the peak value after the impactor contacts the top wall of the hat-shaped structure, and then the load drops sharply due to damage initiation occurring on the corner part of the hat-shaped structure. Several significant differences can be found by comparing the curves between the transverse static tests and the impact loading. 1) The shape of the load-displacement curve in the impact tests shows a fluctuation pattern and generate saw-tooth like shape whereas that of the transverse static tests shows a more stable load. 2) Comparing with the results of transverse static tests, the peak load in the impact tests is higher while the mean load is lower. 3) The load drops dramatically to near zero at the end of the first peak value point, showing that the complete rupture has occurred at the incident end of the hat-shaped hollow beam, leading to no material to physically withstand the load instantaneously.

Progressive deformation patterns of UT-CTT hat-shaped hollow beam in the impact tests at the velocity of 8.5 m/s are shown in Figure 3-22, which shows similar tendency with that in the transverse static tests. After the initial contact with the impactor, the compressive failure occurs on the corner part of the hat-shaped structure, and then the top and side wall winkles. The flange part keeps intact since the rivet joints show good strength. Subsequently, the crack starts growing in the bottom panel. Finally, the specimen completely separates. Specifically, the failure of the corner part of the hat-shaped structure leads no material to resist the bending load for a second which results in the bending load dramatically drops at the end of the first peak force. Subsequently, the crack propagates to other walls of the specimen, and the process of crack propagation, including contacting, bending, breaking, and complete failed, leads to the cyclic increase and decrease of bending load, consequently generating a lot of fluctuations on the load-displacement curves. With the wrinkle formation and increase in the deformation of the specimen, one half of the hat-shaped hollow beam penetrates into the other half of hat-shaped hollow beam, consequently generates delamination in the other half part. It is noted that no significant opening fracture at the overlap area can be observed, which means the flange part keeps intact since the rivet joints show good strength. During the fracture process, the fragment segments or debris

separate from the specimen with increasing shear forces can be observed in the impact tests at the velocity of 8.5 m/s (Figure 3-23). It is noted that final cracks appear on all regions and then the specimen completely separated in the impact tests at the velocity of 8.5 m/s as shown in Figure 3-24.

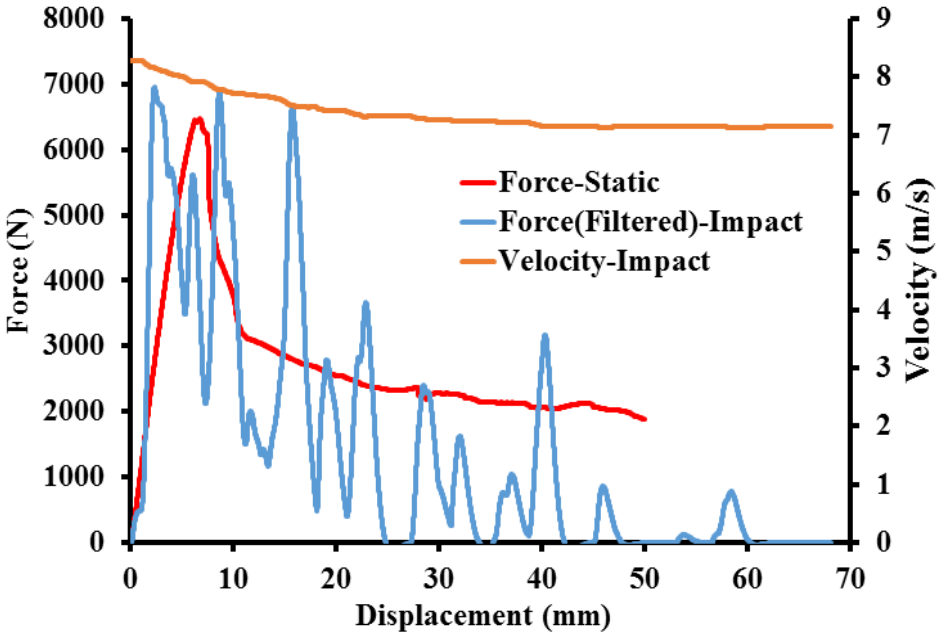

Figure 3-21 Load-displacement curves of experimental results under impact loading

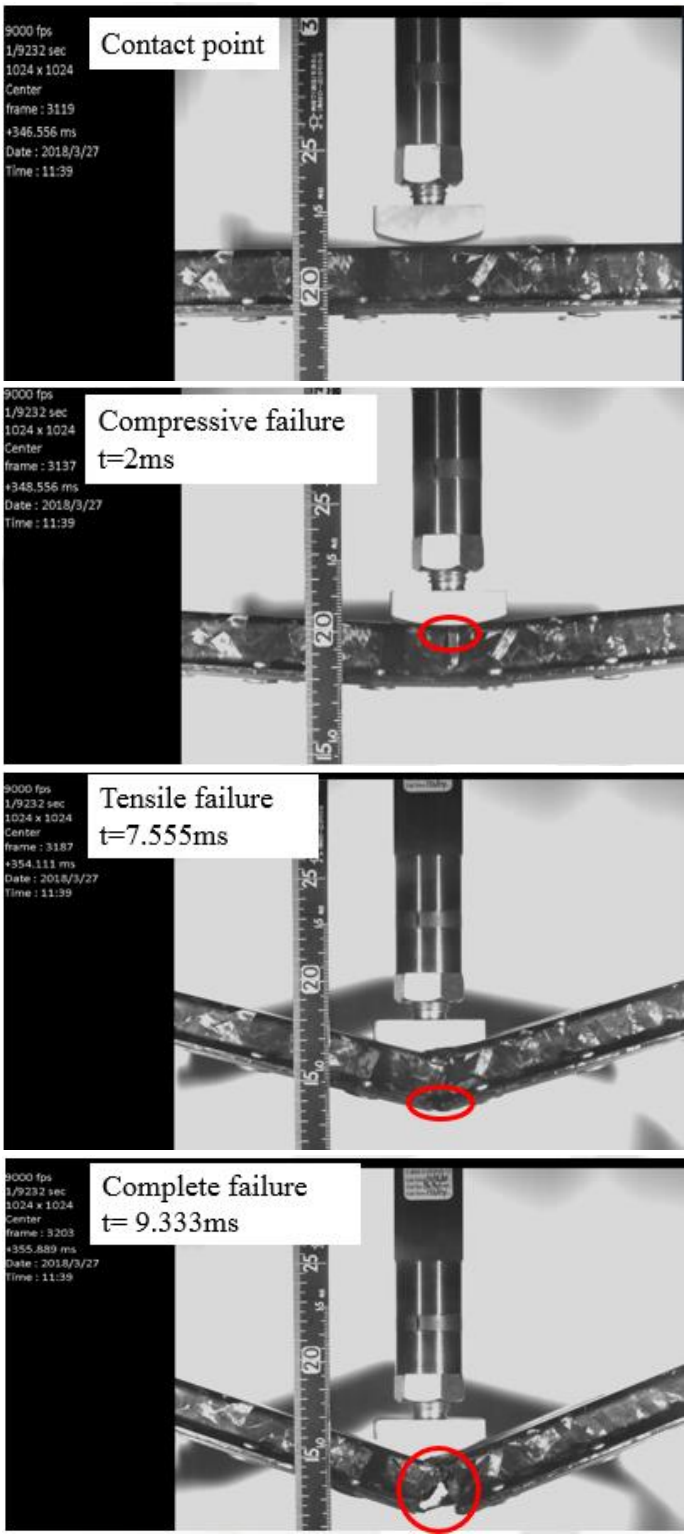

Figure 3-22 Fracture process of hat-shaped hollow beam at the velocity of 8.5 m/s

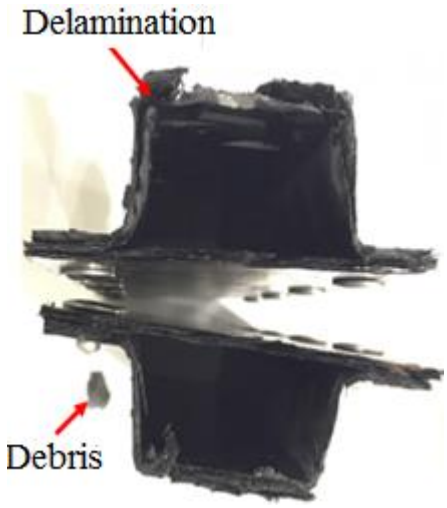

Figure 3-23 Failure mode of UT-CTT hat-shaped hollow beam at the velocity of 8.5 m/s

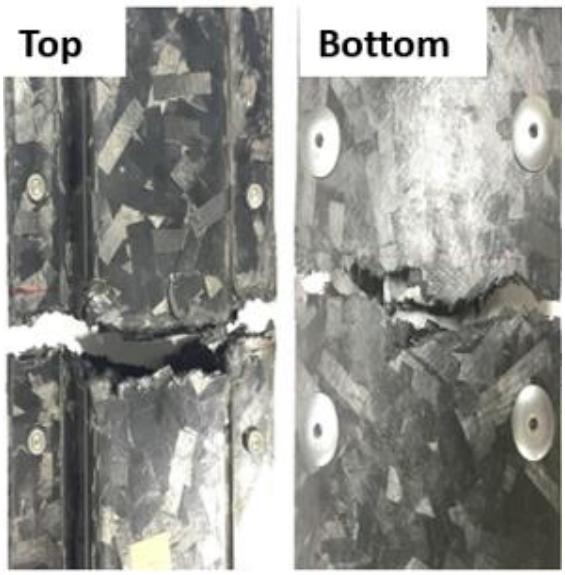

Figure 3-24 Terminal crack on specimen at the velocity of 8.5 m/s

3.4.3.2 Numerical results

Figure 3-25 shows the effect of the SOFT parameter on the simulation results of 2D shell FEM after investigating the sensitivity of the model to variations in the SOFT parameter. It can be observed that the SOFT parameter has no effect on the first peak of simulation results. Besides, by comparing the load-displacement curves between numerical and experimental results as shown in Figure 3-26, the first peak of the 2D shell FEM result is almost same as that of the experimental result even though the tendency shows some differences, especially after the first peak. The energy curves in Figure 3-27 show the ratio of hourglass energy and negative sliding energy (may

be caused by undetected initial penetration) to total energy is almost zero and verify the accuracy of the numerical results. Figure 3-28 shows the comparison of load-displacement curves between 3D solid FEM and experimental results. It can be observed that the first peak of the 3D solid FEM result is almost the same as that of the experimental result and the overall tendency of FEM is similar to the experimental one. By comparing the results of 2D shell FEM and 3D solid FEM, the results of 3D solid FEM is much better than that of 2D shell FEM since delamination failure was taken into account in 3D solid FEM.

Moreover, by observing the compressive stress distribution in 3D solid FEM of the hat-shaped hollow beam under impact loading as shown in Figure 3-29, the fracture process of the numerical simulation shows the same tendency as that of experimental results.

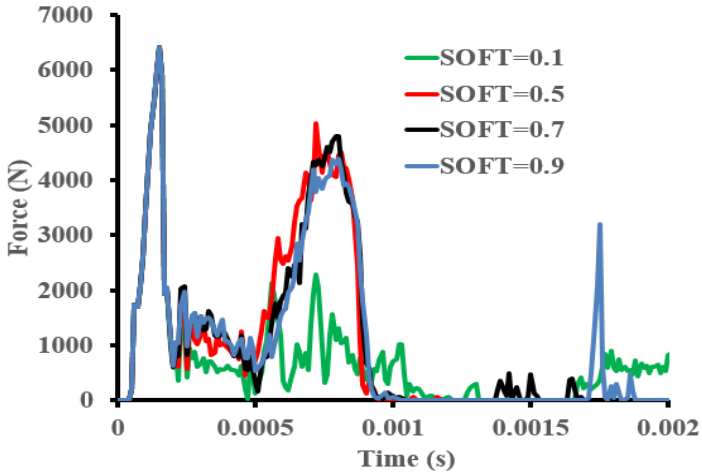

Figure 3-25 Effect of the SOFT parameter on the simulation results

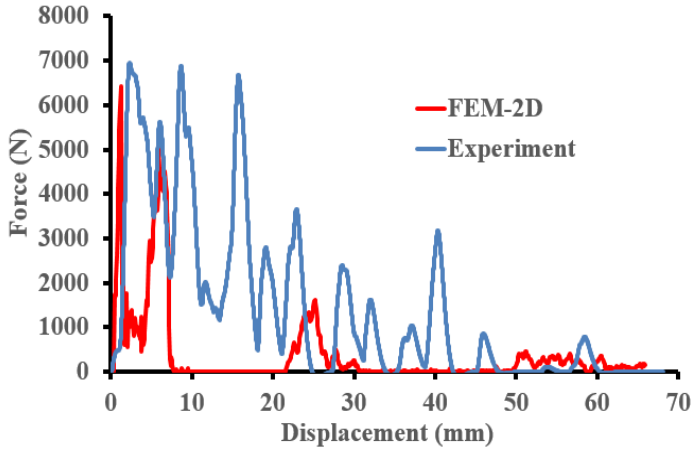

Figure 3-26 Comparison of load-displacement curves between 2D shell FEM and experimental results

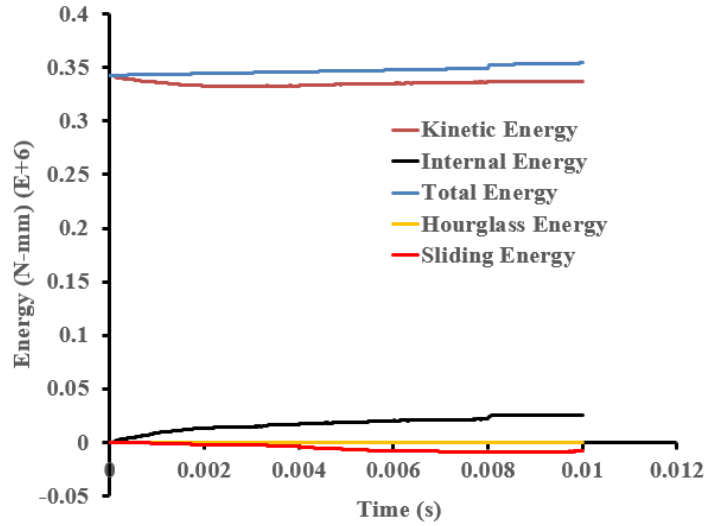

Figure 3-27 Energy curves for kinetic energy, internal energy, total energy, hourglass energy and sliding energy

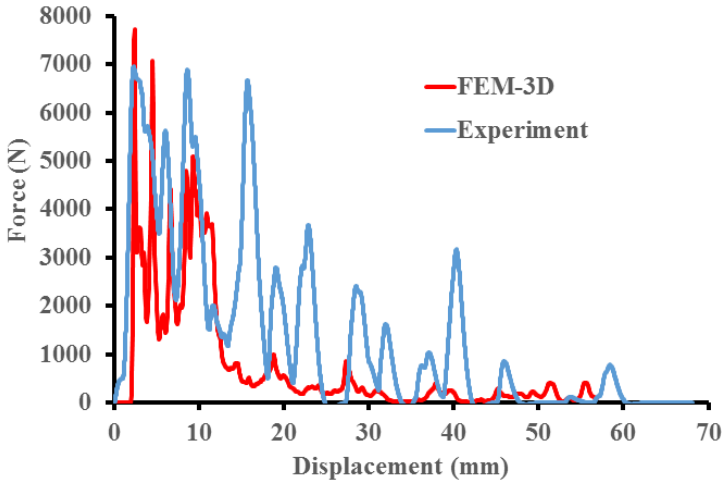

Figure 3-28 Comparison of load-displacement curves between 3D solid FEM and experimental results

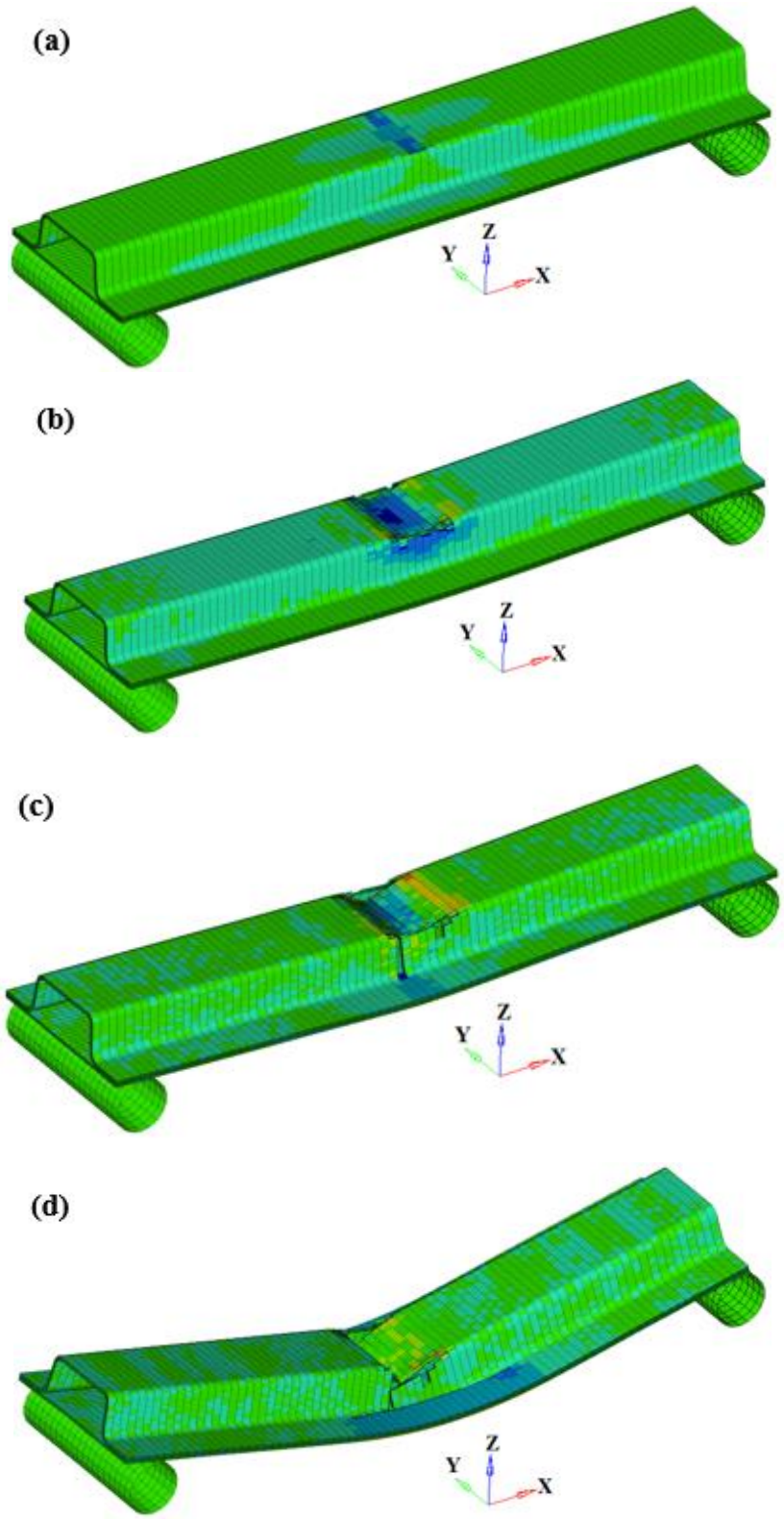

Figure 3-29 The compressive stress distribution in 3D solid FEM of hat-shaped hollow beam under impact loading

3.5 Concluding remarks

The bending fracture behavior of UT-CTT hat-shaped hollow beam was conducted under transverse static and impact loadings with a combination of experimental and numerical analysis. The typical load-displacement and failure mode were compared. The following conclusions can be obtained:

(1) Some significant differences can be found between the transverse static and the impact tests by comparing load-displacement curves. Firstly, the shape of the load-displacement curve in the impact tests shows a fluctuation pattern and generate saw-tooth like shape whereas that of the transverse static tests shows the more stable load. Secondly, the peak load in the impact tests is higher than that in the transverse static tests, but the mean load is lower than that in the transverse static tests. Finally, in the impact tests, the load drops dramatically to near zero at the end of the first peak value point, indicating that the complete rupture occurred at the incident end of the hat-shaped hollow beam, resulting in no wall to physically withstand compressive loading instantaneously.

(2) The progressive failure mode was observed in transverse static bending tests. The crack initiates at the corners of the top wall due to stress concentration caused by the increased compression, and then the cracking region spreads towards the symmetric axis at the top wall and towards the overlap area at the side wall. Simultaneously, the corners of the top wall begin to crush, and the top and side wall start buckling. Finally, the crack starts growing in the overlap area and bottom panel, and then the formation of a plastic hinge can be inhibited. Moreover, the fracture mechanisms under impact tests were similar to transverse static tests when observing the collapsed specimen macroscopically. However, the specimen had more severe damage like delamination, fiber breakage, matrix cracking and debris under impact bending.

(3) Dynamic mechanical parameters of UT-CTT were estimated with the consideration of the strain rate dependence. The value of the ratio of dynamic to static parameters was determined and can be used for the prediction of dynamic mechanical properties.

(4) The results of the proposed finite element models show similar tendency with experimental results in both transverse static and impact loadings. However, the effect of mechanical properties, like dynamic fracture toughness, were suggested to be investigated in the future in order to improve the accuracy of the proposed models.

Therefore, the proposed methods for interacting damage modes can accurately predict the fracture behavior of UT-CTT, and can serve as a benchmark for modelling damage coupling in composite materials.

4. Design optimization of UT-CTT complex structures

4.1 Introduction

In this chapter, strength-based optimization and lightweight optimization of complex structures under single flexural loading and multi-loadings will be studied to show potential applications of UT-CTT for mass-produced vehicles by taking full advantage of the merit "thickness variation". The optimal UT-CTT L-shaped structure, which aims to reduce the interlaminar tensile stress, will be found using free-shape optimization method. Moreover, the lightweight design of CFRTP hat-shaped hollow beam will be studied using multi-material solution, free-shape optimization and size optimization.

4.2 Overview of optimization methods

4.2.1 Optimization introduction

The goal of mathematical optimization is to find design variables x for which objective value f(x) should be satisfied with the prerequisite of the inequality constraints g(x) and equality constraints h(x). A general optimization problem can be expressed mathematically as follows:

Objective function: Minimize or maximize f(x)

Subject to: $g(x) \leq 0$, $h(x) = 0$

4.2.2 Types of optimization problems

Several optimization problem types can be classified as follows:

(1) Continuous optimization and discrete optimization

In continuous optimization problems, the design variables are continuous variables while the design variables in discrete optimization problems are discrete variables. Generally speaking,

optimization problems solved by multi-material solutions can be seen as discrete optimization and optimization problems solved by size optimization can be classified as a continuous optimization. The smoothness of the functions in continuous optimization problems means that the values of the objective functions and constraint functions at a certain point can be referred to deduce information about its neighborhood points, therefore continuous optimization problems are easier to be solved than discrete optimization problems. However, with improvements of algorithms and advancements in computing technology, the computational efficiency of discrete optimization problems has dramatically increased.

(2) Single-objective optimization and multi-objective optimization

Multi-objective optimization problems mean that optimal decisions should be adopted with consideration of trade-offs between two or more conflicting objectives. There are two methods to solve multi-objective optimization problems: the first one is to transfer the multi-objective optimization problems to single-objective optimization problems with a weighted combination of the different objectives. The other one is to use constraints to replace some objectives.

(3) Uncertain optimization and deterministic optimization

The parameters for the given problem have been known in the deterministic optimization problems, whereas the parameters are uncertainty in uncertain optimization problems. Among uncertain optimization problems, robust optimization is a relatively new technique to model uncertainty when the parameters are within certain bounds and the objective of robust optimization problems is to find the optimal solution that is feasible for all uncertainty data.

Specifically, four types of structural design optimization can be found: material optimization, topology optimization, shape optimization and size optimization depending on the type of design variables.

(1) Material optimization

The material types or material properties are the design variables in the material optimization problem and the nature of the material optimization problems can be seen as discrete optimization problems. Therefore, the design variables should be continualized to improve the computational efficiency. Continualization of the problem can be realized as shown in [108] to improve the computational efficiency by using a genetic algorithm[109] or nonlinear mixed-integer algorithm[110].

(2) Topology optimization

In topology optimization problems, the optimal distribution of material or positioning of members within a given design space can be found, which means topology optimization is an inherently discrete optimization and has restrictively high computational effort. The topology optimization is commonly used in initial design phases to clarify the optimal load paths within a given design space.

(3) Shape optimization

The goal of shape optimization is to find the optimal outer boundary of a structure while satisfying given constraints. Shape optimization includes parametric geometrical optimization and the optimal nodal position of the FE model which is the free-shape optimization in OptiStruct.

(4) Sizing optimization

The objective of sizing optimization is to find the optimal geometrical parameters of a structure, such as a length, width, thickness or cross-section of the structure. Since the design variables of sizing optimization are the element descriptions rather than nodal positions of the FE model, the sizing optimization problem is a well-conditioned continuous problem.

4.3 Design optimization of the L-shaped structure

4.3.1 Optimization procedure

A simplified model of UT-CTT L-shaped structures was established in OptiStruct 14.0 utilizing an eight-node hexahedral solid finite element. Element number with 14 in thickness was determined after investigating the mesh dependence. For the two leg parts, length, width, and thickness were discretized using 60, 35, and 14 layers of elements, respectively, with these numbers equaling to 20, 35, and 14, respectively, for the curved section. Overall, the model comprised 68600 elements and 76140 nodes. The degrees of freedom at the bottom of the outer nodes were constrained except for translation in the x-direction. Based on the simulated interlaminar tensile strength determined in Chapter 3, the horizontal static load (F = 360 N) along the X-axis was applied to outer nodes (Figure 4-1) in order to make interlaminar tensile stress exceed interlaminar tensile strength. After simulation, the maximum load point displacement was determined as 13.05 mm, and the total weight was obtained as 14.97 g.

As mentioned above, we aimed to minimize the interlaminar tensile stress of L-shaped structures to increase their delamination initiation load. Importantly, the stiffness of the optimized structure, i.e., its load point displacement, should not be less than that of the original one. The use of discontinuous fiber composites not only avoids winkle formation at curved parts but also enables thickness variation, allowing the position of surface nodes to be varied in the thickness direction, as shown in Figure 4-2. The displacements of these surface nodes were chosen as design variables, with their number equaling to 14769 (= the number of movable surface nodes). The maximal displacement of movable surface nodes was limited to 1.2 mm in the exterior normal direction (shrinking direction).

The design requirements, constraints, and variables were combined to mathematically formulate a design optimization problem below:

(1) Design variables: Node movement $d_y \geq -1.2\ mm$ ("–" represents movement in the shrinking direction).

(2) Constraints: Maximum load point displacement $d_L \leq 13.05\ mm$ and total weight $W \leq 14.97\ g$.

(3) Objective: Minimization of interlaminar tensile stress.

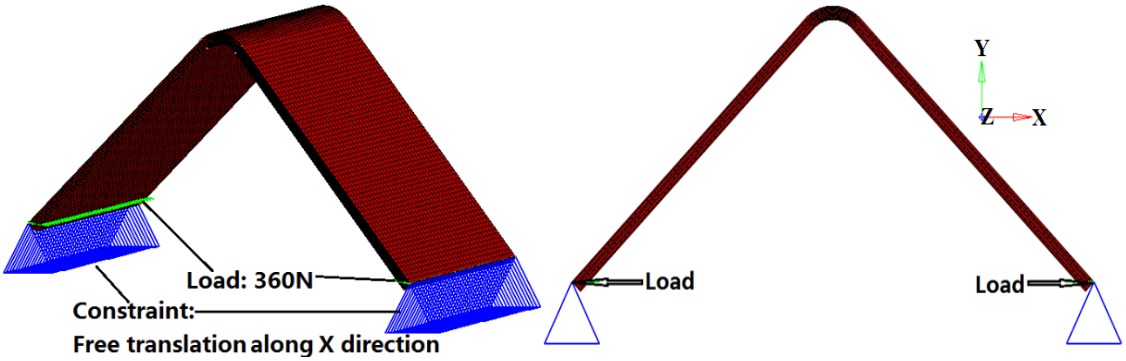

Figure 4-1 Finite element model used for optimization

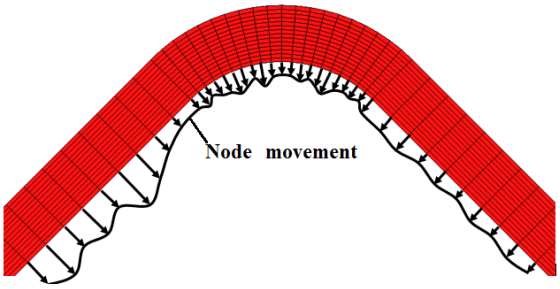

Figure 4-2 Schematic illustration of free-shape optimization

4.3.2 Optimization results

Figure 4-3 depicts the optimized geometry of an L-shaped structure, with different colors representing thickness variation in the Y-direction. The maximum curved section thickness of the optimized model increased from 2.2 mm (original thickness) to 2.63 mm, whereas the minimum thickness of leg parts decreased to 1.955 mm. The shape change in Figure 4-3 (a) was not symmetrical due to the fact that the symmetrical constraint was not set up in the optimization work, and the free-shape optimization results could be not symmetric even though finite element model was totally symmetric including mesh, load case and boundary condition were symmetric. Figure 4-4 shows the distributions of interlaminar tensile stress in the original and optimized structures. In the latter, interlaminar tensile stress was reduced from 53.77 MPa to 48.26 MPa, whereas the load point displacement (13.05 mm) was unchanged, and the structural weight was reduced from 14.97 g to 14.34 g. Thus, free-shape optimization reduced the interlaminar tensile stress of the L-shaped structure while maintaining its original stiffness and weight.

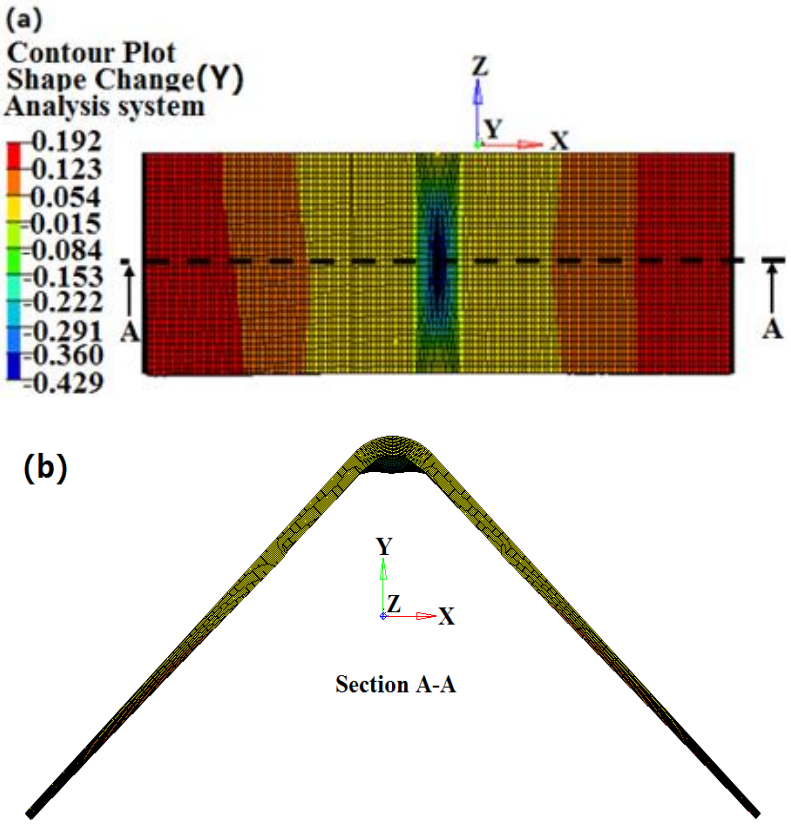

Figure 4-3 Free-shape optimization result: (a) bottom view (b) side view

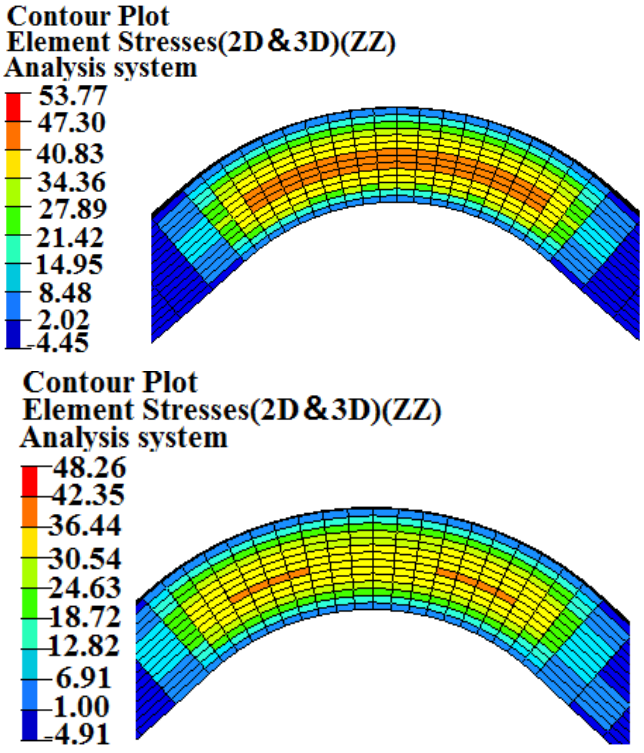

Figure 4-4 Interlaminar tensile stress distribution of original (up) and optimized models (down)

4.4 Design optimization of hat-shaped hollow beam

4.4.1 Optimization under single loading

Based on the result from flexural behavior investigation of UT-CTT has-shaped hollow beam in Chapter 3, the optimal structure will be found under flexural loading in this section through the multi-material solution and free-shape optimization method. The design requirement for CFRTP hat-shaped hollow beam was to minimize the weight while keeping the same stiffness as that of steel one. The stiffness of the optimized CFRTP hat-shaped hollow beam should be no less than that of the steel one, that is, the load point displacement of the optimized CFRTP hat-shaped hollow beam should be no less than that of the steel one. In order to reduce computational time, 2D shell finite element model of UT-CTT has-shaped hollow beam was established during the multi-material solution as shown in Figure 4-5. The thickness of the hat-shaped structure and the panel was both 2mm. The indenter, which was represented by the rigid body, was assigned with a constant force in the vertical direction; the supporters were constrained except translation along Z-axis and rotation around Y-axis. MAT25 was used as the material property of a ply and PROP17 was used for stacking multiplies. Four cases had been considered as shown in Table 4-1. The results showed that the highest flexural stiffness 1526 N/mm can be obtained when the UT-CTT hat-shaped structure and UD panel had been used.

In addition, the effect of the increasing ratio of UD plies in the panel was investigated for improving the flexural stiffness and keeping the total weight of the hat-shaped hollow beam. Figure 4-6 indicates the relationship between the ratio of UD plies in the panel and the flexural stiffness of the hat-shaped hollow beam. From the result, the optimal ratio of UD plies is 0.8, which means the thickness of the UD plies and UT-CTT is 1.6 mm and 0.4 mm, resulting in the highest flexural stiffness 1558 N/mm.

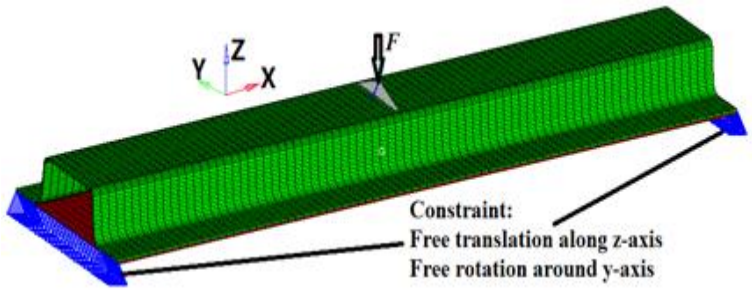

Figure 4-5 2D shell finite element model under flexural loading

Table 4-1 Material selection for high flexural stiffness

NO.	Hat	Panel	Flexural stiffness (N/mm)
1	UD	UD	798
2	UD	UT-CTT	773
3	UT-CTT	UD	1526
4	UT-CTT	UT-CTT	1418

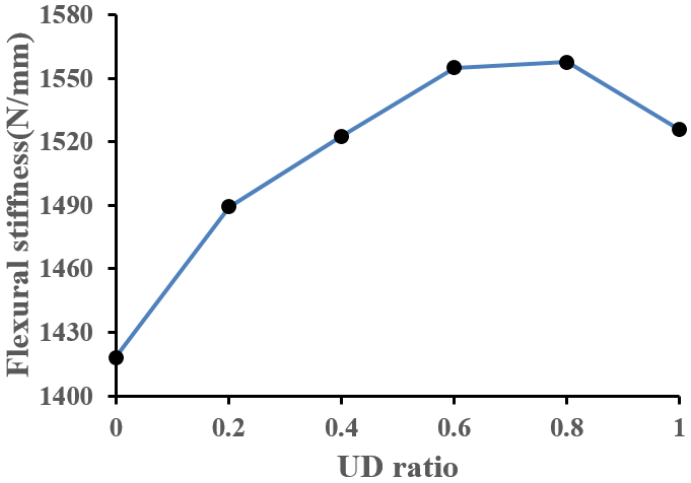

Figure 4-6 The relationship between UD ratio of panel and flexural stiffness

Based on above analytic procedures, the material used for the hat-shaped structure and panel, and the ratio of UD plies in the thickness of the panel have been determined for achieving the highest flexural stiffness of the CFRTP hat-shaped hollow beam. 3D solid FEM of UT-CTT hat-shaped hollow beam was established during free-shape optimization. The surface nodes, the position of which can be varied along the thickness direction, were marked in Figure 4-7. The movement of these surface nodes was chosen as design variables. The number of movable surface nodes totaled 6050, which led to 6050 design variables. There was a lower bound on the thickness for each

movable surface node for the actual design. In the present study, the maximum movements of the 6050 movable surface nodes were limited to 2 mm along normal direction (growing direction and shrinking direction). The design optimization problem is mathematically formulated as follows:

(1) Design variables: Nodes movement $-2\ mm \leq d_z \leq 2\ mm$;

(2) Constraints: The flexural stiffness ≥ 1704 N/mm (Steel);

(3) Objective: Minimum of total weight.

Figure 4-8 depicted the optimized geometry of the hat-shaped hollow beam. The different colors represented thickness variation along the Z direction. For hat-shaped structure, the maximum thickness of central curved parts of the optimized model increased from 2 mm (original thickness) to 3.538 mm whereas the minimum thickness of two end parts of hat-shaped decreased to 1.185 mm. For panel structure, the minimum thickness of two end parts of the panel structure decreased to 1.051 mm. The total weight of the optimized model was 247 g, which means the structural weight reduction was 38% with the same flexural stiffness compared with the weight of steel one. Besides, Figure 4-9 showed stress distribution of the original and optimized CFRTP hat-shaped hollow beam. The position of maximum stress for both models was around the corner between the upper part and the side part of the hat-shaped structure, and the maximum stress was reduced from 648 MPa to 385 MPa after free-shape optimization.

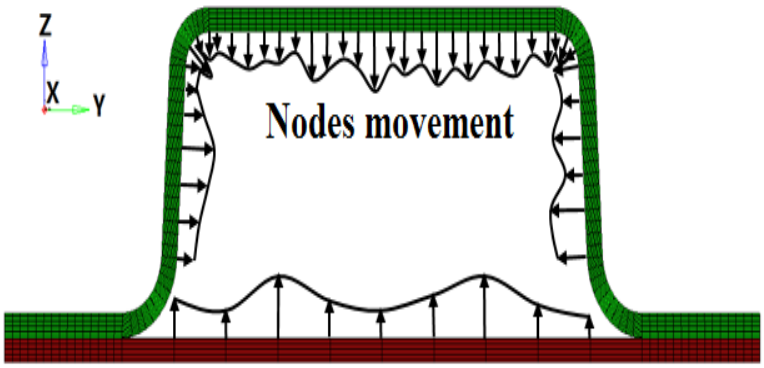

Figure 4-7 Schematic illustration of free-shape optimization

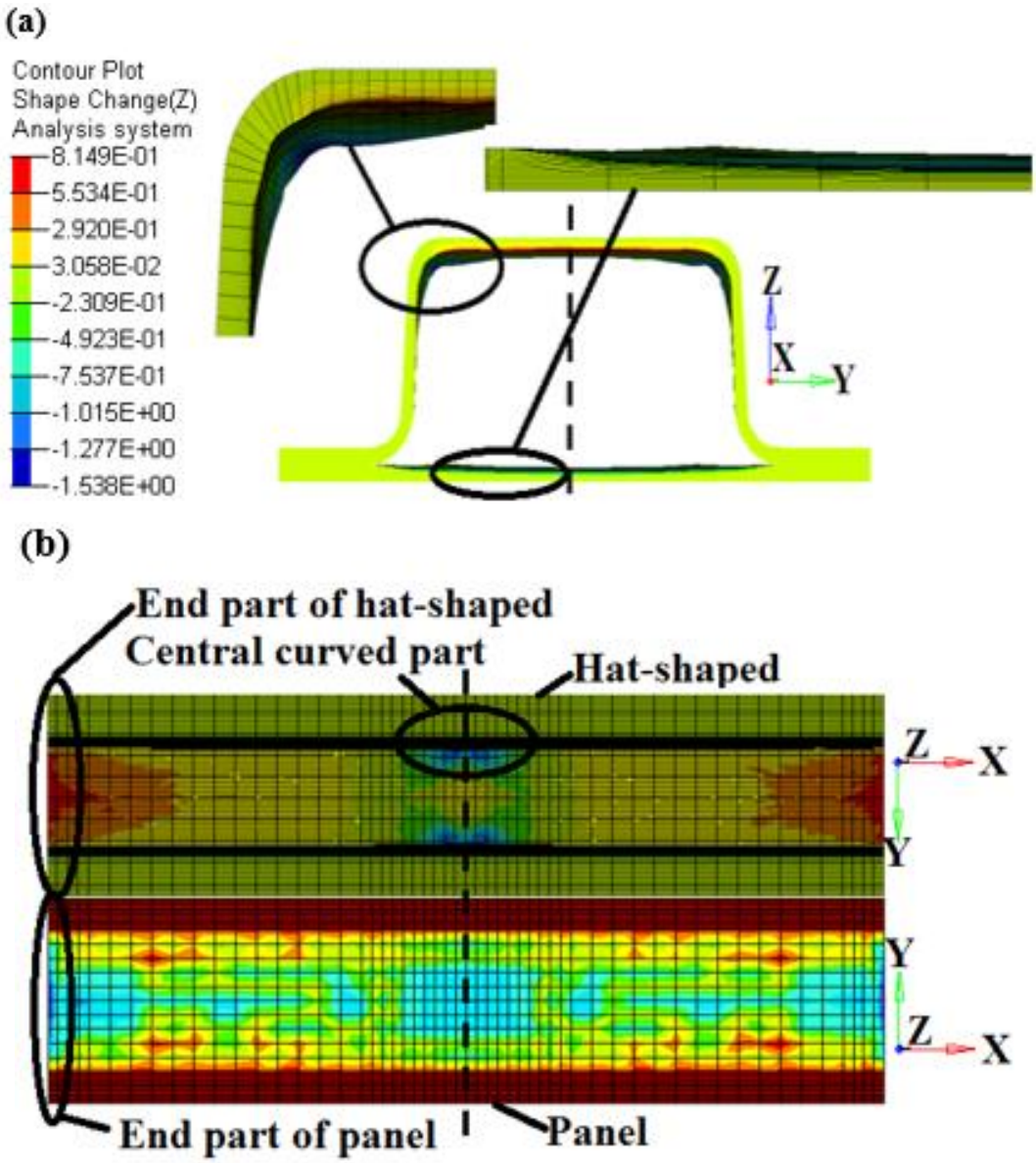

Figure 4-8 The free-shape optimization result: (a) side view (b) top view

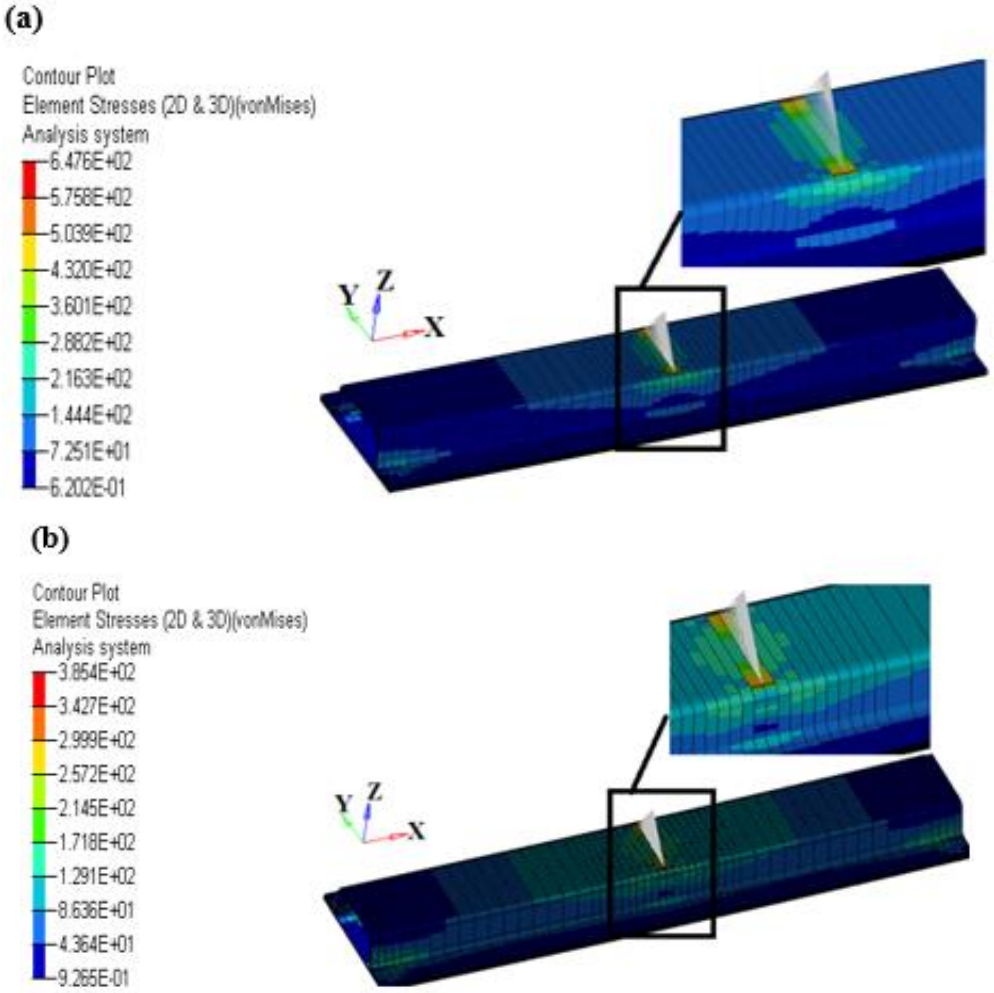

Figure 4-9 Stress distribution of CFRTP hat-stiffened model: (a) before optimization (b) after optimization

4.4.2 Optimization under multi-loadings

Robustness to load from the multi-directions is one of the features required for the automobile frame structure. In order to evaluate the possibility of mass-production application of CFRTP, the hat-shaped hollow beam was designed under three different loadings assuming the flexural, torsional and the roof collision condition as shown in Figure 4-10. The value of 200 N force was used to evaluate stiffness for each FE model.

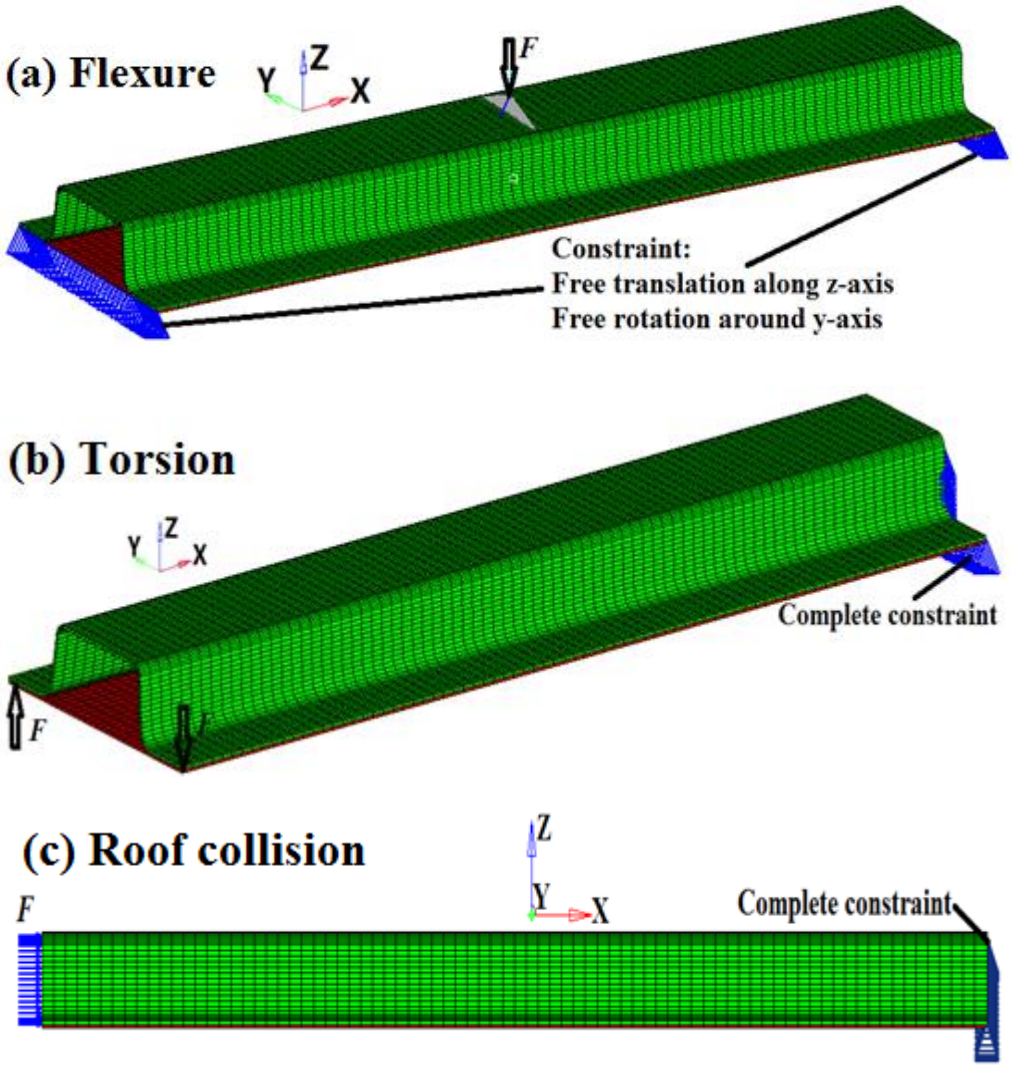

Figure 4-10 FE models of hat-shaped hollow beam under (a) flexural (b) torsional and (c) roof collision loadings

The thickness of steel hat-shaped and panel part are both 1 mm while the initial thickness of UT-CTT ones is 3 mm. The evaluated indexes in FEM study are mass and compliance of the model.

The compliance is defined as a relation of an inverse proportion with stiffness. The weight of the steel model is 746 g and UT-CTT model is 425 g, however, the stiffness of the UT-CTT model under three conditions are not more than that of steel one.

Therefore, the applicability of a hybrid structure composed of UT-CTT and UD material was used to improve stiffness and achieve more lightweight structure. Though mechanical properties of UD in the longitudinal direction are three times higher than those of UT-CTT, the mechanical properties in transversal direction are only one-eighth of UT-CTT. Hence, it is reasonable that UD is used as a reinforcement of UT-CTT.

The size optimization was used to find the optimal thickness of each ply of UT-CTT and UD (Figure 4-11). The design variables are the thickness of each ply of UT-CTT and UD, the lower and upper thickness of each ply are 0.1 mm and 0.5 mm. The constraint function is that the compliance of hybrid material structure is less than that of steel one, and the objective function is the minimization of mass. By size optimization, the thickness of each part and each ply was adjusted to the optimal parameter as shown in Figure 4-12 and Figure 4-13. Weight reduction of 43% was achieved in keeping the same stiffness as that of steel one under the three loading conditions. Table 4-2 shows the comparison of compliance and mass before and after optimization.

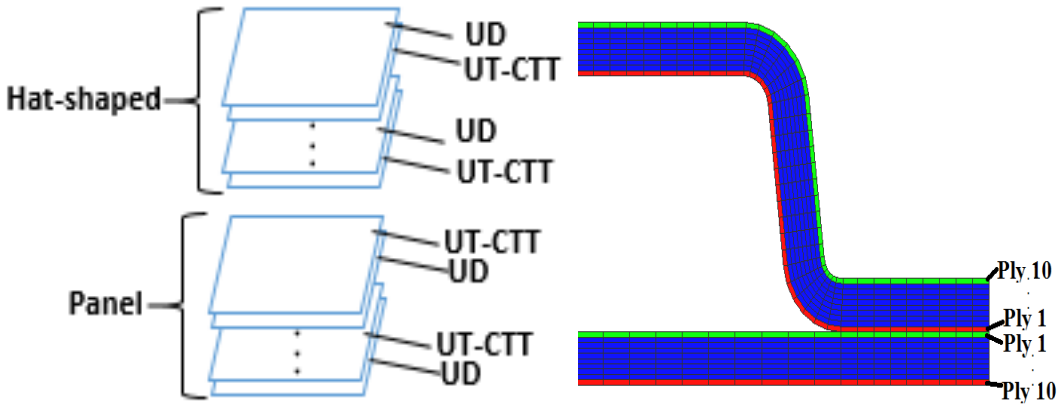

Figure 4-11 Stack consequence of UD and UT-CTT

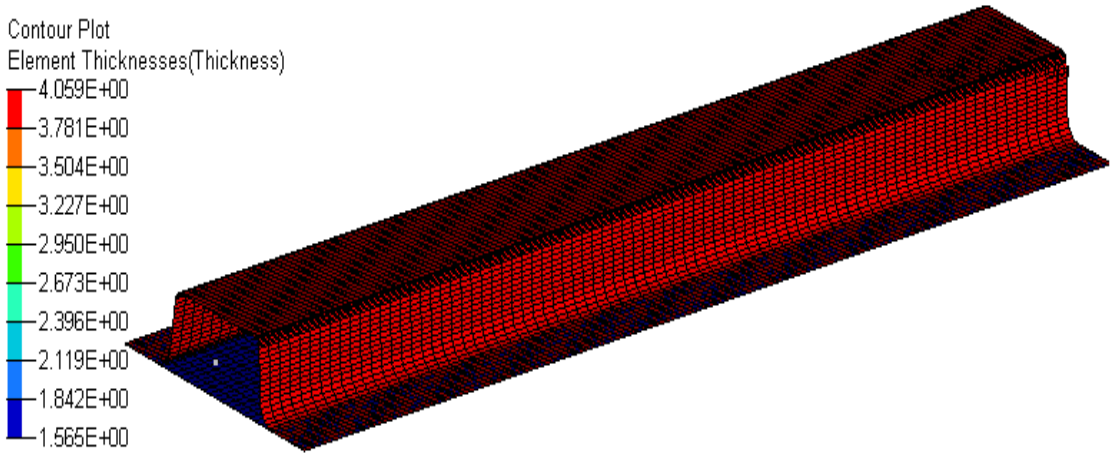

Figure 4-12 The optimal total thickness of each part

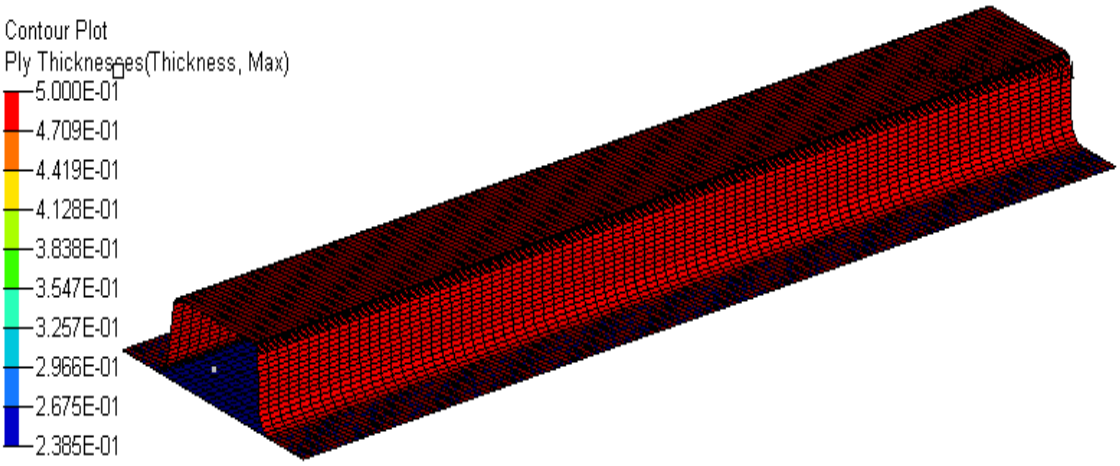

Figure 4-13 The maximum ply thickness of UT-CTT and UD

Table 4-2 Comparison of compliance and mass before and after optimization

	Material	Compliance			Mass (g)
		Flexure	Torsion	Roof collision	
Before optimization	Steel	7	186	0.2	746
	UT-CTT	9.6	91	0.31	425
Hybrid material	UT-CTT+UD	7.7	137	0.2	425
After size optimization	UT-CTT+UD	7	161	0.18	425

4.5 Concluding remarks

Strength-based optimization of L-shaped structure and lightweight optimization of the hat-shaped hollow beam have been conducted by using different optimization methods including multi-material solutions, free-shape optimization and size optimization.

(1) Free-shape optimization of the L-shaped structures was presented, with the objective (interlaminar tensile stress) considered with constraints on structural stiffness and weight, whereas the thickness variations of the inner parts of the L-shaped structure were used as design variables. The obtained results suggested that increasing the thickness of the central part of the curved section and decreasing that of two leg parts should result in a lower interlaminar tensile stress and unchanged original stiffness and weight.
(2) Weight reduction of 38% by CFRTP can be achieved through lightweight design using multi-material solution and free-shape optimization for UT-CTT hat-shaped hollow beam under flexural loading.
(3) Weight reduction of 43% was achieved with keeping the same stiffness as that of steel one under the three loading conditions including flexural, torsional and roof collision loadings.

Therefore, it can lead to a conclusion that the work can contribute to show potential application of UT-CTT for mass-produced vehicles by taking full advantage of the merit “thickness variation”.

5. Conclusions

The objectives of this thesis were to investigate fracture behaviors and design optimization of UT-CTT complex structures. Experimental and analytical characterization of interlaminar behavior, fracture mechanisms characteristics of UT-CTT hat-shaped hollow beam under transverse static and impact bending were performed. Besides, a computationally efficient 2D model for predicting delamination and finite element model for interacting damage modes which took into account out-of-plane failure were proposed and evaluated. Subsequently, strength-based optimization and lightweight optimization of complex structures under single flexural loading and multi-loadings were studied to show potential application of UT-CTT for mass-produced vehicles by taking full advantage of the merit "thickness variation". The following sections will summarize the main conclusions of this work and discuss future work.

5.1 Conclusions: Fracture behaviors investigation

5.1.1 Interlaminar behavior

The interlaminar fracture toughness and interlaminar tensile strength of UT-CTT were characterized experimentally, analytically and numerically.

In examples of mode I delamination, unstable crack growth resulted in saw-tooth like load-displacement curves after the initial stage of increasing load, while some specimens displaying mode II delamination exhibited stable crack propagation. 3D measurement macroscope showed that the crack front of DCB specimens presented nearly straight, enabling the application of cohesive zone model in FEM, and a microscopic study using scanning electron microscope revealed that the matrix extension that could resist crack growth resulted in stable crack propagation for ENF specimens. Analytical methods based on linear elastic fracture mechanics and beam theory work well for the determination of Mode I and Mode II fracture toughness of UT-CTT, respectively. An accurate method for estimating the interlaminar tensile strength of L-

shaped structures by analysis of four-point bending test was developed and revealed that the failure of these commonly used structures was due to the sudden and instantaneous propagation of delamination in the curved section.

A computationally efficient model using surface-based cohesive zone model with triangular CZM law developed in this study can be used for predicting the interlaminar behavior of UT-CTT. It is noted that the method that by defining a range with minimum and maximum critical strain energy release rate values to generate two stable crack propagation curves can efficiently predict unstable crack propagation process in DCB tests, whereas the numerical results could achieve a good correlation with the experimental results by choosing appropriate parameters of interfacial shear strength and friction in ENF tests.

5.1.2 Flexural and impact behavior

Fracture mechanisms characteristics of UT-CTT hat-shaped hollow beam subjected to transverse static and impact bending was clarified. The progressive failure mode was observed in transverse static bending tests. The crack initiates at the corners of the top wall due to stress concentration caused by the increased compression, and then the cracking region spreads towards the symmetric axis at the top wall and towards the overlap area at the side wall. Simultaneously, the corners of the top wall begin to crush, and the top and side wall start buckling. Finally, the crack starts growing in the overlap area and bottom panel, and then the formation of a plastic hinge can be inhibited. Moreover, the fracture mechanisms under impact tests were similar to transverse static tests when observing the collapsed specimen macroscopically. However, the specimen had more severe damage like delamination, fiber breakage, matrix cracking and debris under impact bending. Besides, the shape of the load-displacement curve in the impact tests shows a fluctuation pattern and generate saw-tooth like shape whereas that of the transverse static tests shows the more stable load. And, the peak load in the impact tests is higher than that in the transverse static tests, but the mean load is lower than that in the transverse static tests.

2D shell FEM and 3D solid FEM with consideration of the out-of-plane normal and tangential damage mechanisms were established to predict fracture behavior of hat-shaped hollow beam under impact loading. The tiebreak contact was used for delamination simulation, and the

simulation results of the 3D solid model show much closer to the experimental results than that of 2D shell model. Thus, the proposed methods can accurately predict the fracture behavior of UT-CTT, allowing engineers to improve their designs by relying on an integrated consideration of in- and out-of-plane strengths of composite materials. And the proposed modelling approach for interacting damage modes can serve as a benchmark for modelling damage coupling in composite materials.

5.2 Conclusions: Design optimization

Strength-based optimization and lightweight optimization of curved-shape structure and hat-shaped hollow beam have been conducted to show potential application of UT-CTT for mass-produced vehicles by taking full advantage of the merit “thickness variation”.

The interlaminar tensile stress of the optimal UT-CTT L-shaped structure has decreased from 53.77 MPa to 48.26 MPa using free-shape optimization method, in which the thickness of the inner parts has changed while keeping same structural stiffness and weight.

Weight reduction of 38% by CFRTP can be achieved through lightweight design using multi-material solution and free-shape optimization for UT-CTT hat-shaped hollow beam under flexural loading, and weight reduction of 43% was achieved in keeping the same stiffness as that of steel one under the three loading conditions including flexural, torsional and roof collision loadings.

5.3 Future work

UT-CTT, one kind of discontinuous CFRTPs, has developed recently and still has many problems to be solved by the improvement of the material itself. However, it is also important to accumulate knowledge about efficient structural design to maximize the potential mass-production application of UT-CTT. Studies of fracture behaviors and structure optimization in this work are part of research to realize this objective. Although notable contribution was made in this study, further work needs to be performed to advance the understanding of UT-CTT composites and to develop modelling techniques that would simplify certification. The recommended areas for future work are summarized as follows:

(1) Additional work needs to be done to address the issue of material heterogeneity both with respect to experimental work and modelling approaches. Also, the connection between the behavior and variability of test specimens and the actual components needs to be made. This comparison will help to understand what specimen size and geometry are the most representative of the component properties.

(2) Additional work about the measurement of UT-CTT mechanical properties needs to be done. In this work, interlaminar shear strength was determined using the parametric study, and dynamic composite material properties like out-of-plane fracture strain were predicted theoretically. Therefore, precise mechanical properties need to be obtained for more accurate numerical simulation.

(3) Additional work about damage criteria for intralaminar fracture simulation of UT-CTT structures and FEMs using static and dynamic mechanical properties should be compared. Although the proposed modellings for simulating fracture behavior of UT-CTT hat-shaped hollow beam under flexural and impact loadings show good agreement with experimental results to some extent, fracture behaviors of UT-CTT have been not completely understood, which means better suitable fracture criteria should be considered further, and the influence factors

(4) Design optimization that takes into account not only mechanical performance but also costs or manufacturing process should be also considered in the future work. What is more, the optimization with consideration of the effect of fibers alignments on the final optimization work should be studied since the present study did not consider the factor which may be a big influence on the actual optimal structures.

Appendix Digital filtering method

Digital filtering was used to suppress signal distortion induced by impactor ringing, which is a well-known and inevitable problem in the drop-weight test. Force versus time histories typically contains many oscillations caused by two primary sources. The first one is the natural frequency of the impactor, and is often referred to as "impactor ringing." The ringing may be more severe if the impactor components are not rigidly attached. The second one of force oscillations is the flexural vibration of the impacted specimen. The "ringing" oscillations generally occur at higher frequencies than the oscillations generated by the impacted specimen. It is noted that the high-frequency ringing oscillations are not an actual force applied to the specimen whereas the oscillations caused by the specimen are actual forces transmitted to the impacted specimen and should not be filtered or smoothed. For both sources, the oscillations are typically excited during initial contact and during damage formation. The equations of the digital low-pass filter which is applied to the data are as follows:

$$y(n) = a_0 x(n) + a_1 x(n-1) + a_2 x(n-2) - b_1 y(n-1) - b_2 y(n-2)$$

$$\begin{cases} a_0 = a_2 = \dfrac{(\omega_a T)^2}{4 + 2\sqrt{2}\omega_a T + (\omega_a T)^2} \\ a_1 = \dfrac{2(\omega_a T)^2}{4 + 2\sqrt{2}\omega_a T + (\omega_a T)^2} = 2a_0 \\ b_1 = \dfrac{-8 + 2(\omega_a T)^2}{4 + 2\sqrt{2}\omega_a T + (\omega_a T)^2} \\ b_2 = \dfrac{4 - 2\sqrt{2}\omega_a T + (\omega_a T)^2}{4 + 2\sqrt{2}\omega_a T + (\omega_a T)^2} \end{cases}$$

$$\omega_a = \frac{2}{T \tan(2\pi f_d T / 2)}$$

Here, x(n) is input force signal, y(n) is output force signal, T is sampling interval, f_d is cut-off digital frequency.

The sampling interval is 1.22e-6 s and the cut-off digital frequency is 2000 Hz. After digital filtering, the raw and filtered load-time and load-displacement curves at the velocity of 8.5 m/s are as follows:

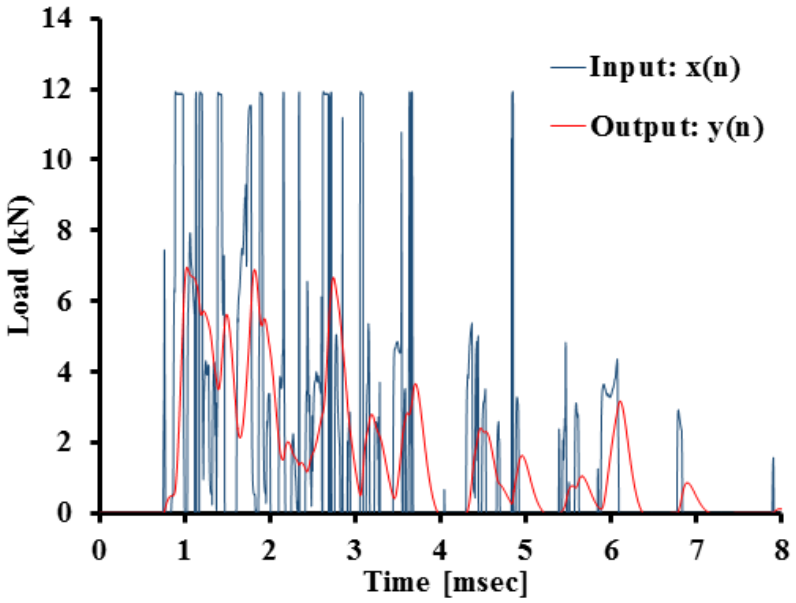

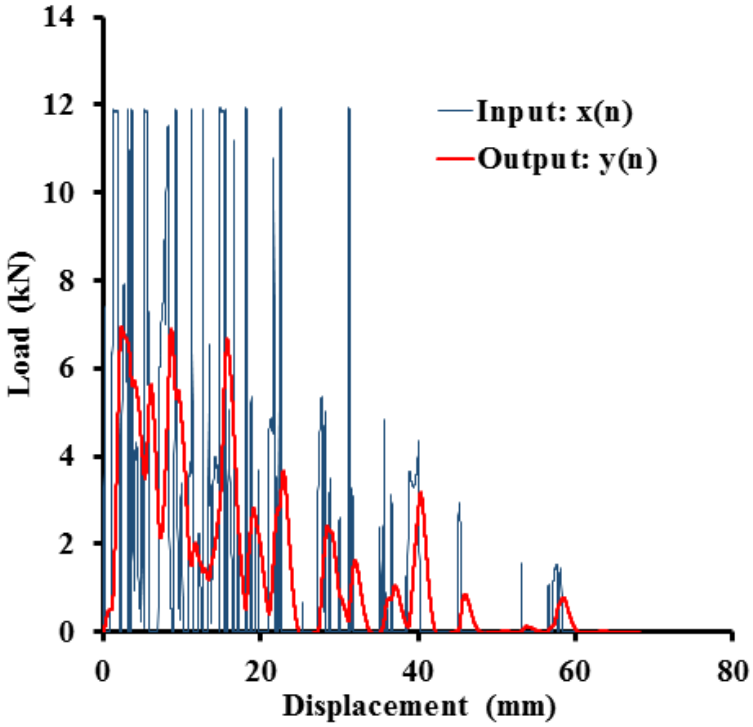

References

[1] M. Khelifa, V. Fierro, and A. Celzard, *FE simulation of repaired timber beams under tensile load using CFRP patches.* Journal of Adhesion Science and Technology, 2015. **29**(3): p. 158-170.

[2] J. Takahashi and T. Ishikawa. *Current Japanese activity in CFRTP for mass production automotive application*. in *13th Japan international SAMPE symposium and exhibition*. 2013. Nagoya, Japan.

[3] L. Svärd, *Composites failure modeling and optimization of a spring orthosis*. 2012, Chalmers University of Technology.

[4] D. Suzuki, J. Takahashi, K. Kageyama, K. Uzawa, and I. Ohsawa. *Purpose and target of the development of carbon fiber reinforced thermoplastics*. in *10th Japan International SAMPE Symposium & Exhibition (JISSE-10)*. 2007. Tokyo Big Sight, Tokyo, Japan.

[5] P. Feraboli, E. Peitso, F. Deleo, T. Cleveland, and P.B. Stickler, *Characterization of prepreg-based discontinuous carbon fiber/epoxy systems.* Journal of Reinforced Plastics and Composites, 2009. **28**(10): p. 1191-1214.

[6] P. Feraboli, E. Peitso, T. Cleveland, and P.B. Stickler, *Modulus measurement for prepreg-based discontinuous carbon fiber/epoxy systems.* Journal of Composite Materials, 2009. **43**(19): p. 1947-1965.

[7] M.E. Tuttle, T. Shifman, and B. Boursier. *Simplifying certification of discontinuous composite material forms for primary aircraft structures*. in *SAMPE Conference*. 2010. Seattle, Washington.

[8] L.T. Harper, *Discontinuous carbon fibre composites for automotive applications*. 2006, University of Nottingham.

[9] Y. Wan, T. Ohori, and J. Takahashi. *Mechanical properties and modeling of discontinuous carbon fiber reinforced thermoplastics*. in *The 20th international conference on composite materials. Copenhagen, Denmark*. 2015.

[10] G.P. Picher-Martel, A. Levy, and P. Hubert, *Compression moulding of Carbon/PEEK randomly-oriented strands composites: A 2D Finite Element model to predict the squeeze flow behaviour.* Composites Part A: Applied Science and Manufacturing, 2016. **81**: p. 69-77.

[11] B. Landry and P. Hubert, *Experimental study of defect formation during processing of randomly-oriented strand carbon/PEEK composites.* Composites Part A: Applied Science and Manufacturing, 2015. **77**: p. 301-309.

[12] A. Levy and P. Hubert, *Interstrand void content evolution in compression moulding of randomly oriented strands (ROS) of thermoplastic composites.* Composites Part A: Applied Science and Manufacturing, 2015. **70**: p. 121-131.

[13] M. Selezneva and L. Lessard, *Characterization of mechanical properties of randomly oriented strand thermoplastic composites.* Journal of Composite Materials, 2016. **50**(20): p. 2833-2851.

[14] M. Selezneva, S. Roy, L. Lessard, and A. Yousefpour, *Analytical model for prediction of strength and fracture paths characteristic to randomly oriented strand (ROS) composites.* Composites Part B: Engineering, 2016. **96**: p. 103-111.

[15] M. Selezneva, S. Roy, S. Meldrum, L. Lessard, and A. Yousefpour, *Modelling of mechanical properties of randomly oriented strand thermoplastic composites.* Journal of Composite Materials, 2017. **51**(6): p. 831-845.

[16] M. Selezneva, *Experimental and theoretical investigations of mechanical properties of randomly-oriented strand ROS composites*. 2015, McGill University.

[17] M. Darvell, *Randomized CFRTP tape piece laminates in structural automotive applications*. 2015, KTH Royal Institute of Technology.

[18] *Toray's carbon fiber materials adopted by Toyota's fuel cell vehicle Mirai CFRTP*. Available from: http://www.jeccomposites.com/knowledge/international-composites-news/toray%E2%80%99s-carbon-fiber-materials-adopted-toyota%E2%80%99s-fuel-cell.

[19] I. De Baere, S. Jacques, W. Van Paepegem, and J. Degrieck, *Study of the Mode I and Mode II interlaminar behaviour of a carbon fabric reinforced thermoplastic.* Polymer Testing, 2012. **31**(2): p. 322-332.

[20] S. Ivanov, L. Gorbatikh, and S. Lomov. *Interlaminar fracture behaviour of textile composites with thermoplastic matrices*. in *16th European Conference on Composite Materials*. 2014. Seville, Spain.

[21] Y. Ma, Y. Yang, T. Sugahara, and H. Hamada, *A study on the failure behavior and mechanical properties of unidirectional fiber reinforced thermosetting and thermoplastic composites.* Composites Part B: Engineering, 2016. **99**: p. 162-172.

[22] J. Schon, T. Nyman, A. Blom, and H. Ansell, *A numerical and experimental investigation of delamination behaviour in the DCB specimen.* Composites Science and Technology, 2000. **60**(2): p. 173-184.

[23] J. Schön, T. Nyman, A. Blom, and H. Ansell, *Numerical and experimental investigation of a composite ENF-specimen.* Engineering Fracture Mechanics, 2000. **65**(4): p. 405-433.

[24] W.X. Wang, M. Nakata, Y. Takao, and T. Matsubara, *Experimental investigation on test methods for mode II interlaminar fracture testing of carbon fiber reinforced composites.* Composites Part A: Applied Science and Manufacturing, 2009. **40**(9): p. 1447-1455.

[25] H. Zabala, L. Aretxabaleta, G. Castillo, and J. Aurrekoetxea, *Loading rate dependency on mode I interlaminar fracture toughness of unidirectional and woven carbon fibre epoxy composites.* Composite Structures, 2015. **121**: p. 75-82.

[26] H. Miyagawa, C. Sato, and K. Ikegami, *Effect of fiber orientation on Mode I fracture toughness of CFRP.* Journal of Applied Polymer Science, 2010. **115**(6): p. 3295-3302.

[27] L. Yao, R. Alderliesten, M. Zhao, and R. Benedictus, *Bridging effect on mode I fatigue delamination behavior in composite laminates.* Composites Part A: Applied Science and Manufacturing, 2014. **63**: p. 103-109.

[28] L. Yao, Y. Sun, L. Guo, R.C. Alderliesten, R. Benedictus, M. Zhao, and L. Jia, *Fibre bridging effect on the Paris relation of mode I fatigue delamination in composite laminates with different thicknesses.* International Journal of Fatigue, 2017. **103**: p. 196-206.

[29] E. Farmand-Ashtiani, J. Cugnoni, and J. Botsis, *Specimen thickness dependence of large scale fiber bridging in mode I interlaminar fracture of carbon epoxy composite.* International Journal of Solids and Structures, 2015. **55**: p. 58-65.

[30] P.N.B. Reis, J.A.M. Ferreira, F.V. Antunes, and J.D.M. Costa, *Initial crack length on the interlaminar fracture of woven carbon/epoxy laminates.* Fibers and Polymers, 2015. **16**(4): p. 894-901.

[31] G. Wimmer, W. Kitzmüller, G. Pinter, T. Wettemann, and H.E. Pettermann, *Computational and experimental investigation of delamination in L-shaped laminated composite components.* Engineering Fracture Mechanics, 2009. **76**(18): p. 2810-2820.

[32] Y. Wan, T. Matsuo, I. Ohsawa, and J. Takahashi, *Effects of curvature on strength and damage modes of L-shaped carbon fiber-reinforced polypropylene.* Journal of Reinforced Plastics and Composites, 2014. **33**(14): p. 1305-1315.

[33] T. Matsuo, T. Goto, and J. Takahashi, *Investigation about the fracture behavior and strength in a curved section of CF/PP composite by a thin-curved beam specimen.* Advanced Composite Materials, 2015. **24**(3): p. 249-268.

[34] Raju, B.G. Prusty, and D.W. Kelly, *Delamination failure of composite top-hat stiffeners using finite element analysis.* Proceedings of the Institution of Mechanical Engineers, Part M: Journal of Engineering for the Maritime Environment, 2013. **227**(1): p. 61-80.

[35] Q. Liu, H.L. Xing, Y. Ju, Z.Y. Ou, and Q. Li, *Quasi-static axial crushing and transverse bending of double hat shaped CFRP tubes.* Composite Structures, 2014. **117**: p. 1-11.

[36] B.C. Jin, X.C. Li, R. Mier, A. Pun, S. Joshi, and S. Nutt, *Parametric modeling, higher order FEA and experimental investigation of hat-stiffened composite panels.* Composite Structures, 2015. **128**: p. 207-220.

[37] M. Ramamurthi, J.S. Lee, S.H. Yang, and Y.S. Kim, *Delamination characterization of bonded interface in polymer coated steel using surface based cohesive model.* International Journal of Precision Engineering and Manufacturing, 2013. **14**(10): p. 1755-1765.

[38] D. Hu and C. Duan. *Simulation and analysis of transverse interface cracking of carbon fiber reinforced composite*. in *5th International Conference on Advanced Materials and Computer Science*. 2016. Qingdao, China.

[39] H. Wang, Q. Qin, H. Ji, and Y. Sun, *Comparison among different modeling techniques of 3D micromechanical modeling of damage in unidirectional composites.* Advanced Science Letters, 2011. **4**: p. 400-407.

[40] S. Jacques, I. De Baere, and W. Van Paepegem, *Analysis of the numerical and geometrical parameters influencing the simulation of Mode I and Mode II delamination growth in unidirectional and textile composites.* Applied Composite Materials, 2015. **22**(6): p. 637-668.

[41] G. Alfano, *On the influence of the shape of the interface law on the application of cohesive-zone models.* Composites Science and Technology, 2006. **66**(6): p. 723-730.

[42] E. Panettieri, D. Fanteria, and F. Danzi, *A sensitivity study on cohesive elements parameters: Towards their effective use to predict delaminations in low-velocity impacts on composites.* Composite Structures, 2016. **137**: p. 130-139.

[43] H. Yuan and X. Li, *Effects of the cohesive law on ductile crack propagation simulation by using cohesive zone models.* Engineering Fracture Mechanics, 2014. **126**: p. 1-11.

[44] P.F. Liu, Z.P. Gu, X.Q. Peng, and J.Y. Zheng, *Finite element analysis of the influence of cohesive law parameters on the multiple delamination behaviors of composites under compression.* Composite Structures, 2015. **131**: p. 975-986.

[45] R. Campilho, M.D. Banea, J. Neto, and L.F.M. da Silva, *Modelling adhesive joints with cohesive zone models: effect of the cohesive law shape of the adhesive layer.* International Journal of Adhesion and Adhesives, 2013. **44**: p. 48-56.

[46] M. Ridha, V.B.C. Tan, and T.E. Tay, *Traction–separation laws for progressive failure of bonded scarf repair of composite panel.* Composite Structures, 2011. **93**(4): p. 1239-1245.

[47] T. Matsuo, M. Kan, K. Furukawa, T. Sumiyama, H. Enomoto, and K. Sakaguchi, *Numerical modeling and analysis for axial compressive crushing of randomly oriented thermoplastic composite tubes based on the out-of-plane damage mechanism.* Composite Structures, 2017. **181**: p. 368-378.

[48] M. Meng, H.R. Le, M.J. Rizvi, and S.M. Grove, *3D FEA modelling of laminated composites in bending and their failure mechanisms.* Composite Structures, 2015. **119**: p. 693-708.

[49] O.T. Topac, B. Gozluklu, E. Gurses, and D. Coker, *Experimental and computational study of the damage process in CFRP composite beams under low-velocity impact.* Composites Part A: Applied Science and Manufacturing, 2017. **92**: p. 167-182.

[50] J. Zhang and X. Zhang, *Simulating low-velocity impact induced delamination in composites by a quasi-static load model with surface-based cohesive contact.* Composite Structures, 2015. **125**: p. 51-57.

[51] M. Yamashita and I. Yamamoto, *Bending collapse behaviour of hat-shaped tubular structure strengthened with CFRP sheet.* Advances in Materials and Processing Technologies, 2016. **2**(4): p. 461-470.

[52] H.C. Kim, D.K. Shin, and J.J. Lee, *Characteristics of aluminum/CFRP short square hollow section beam under transverse quasi-static loading.* Composites Part B: Engineering, 2013. **51**: p. 345-358.

[53] S.Y. Kim, J.W. Jeong, J.Y. Kim, H.C. Kim, D.K. Shin, K.C. Shin, and J.J. Lee, *Energy absorption characteristics of aluminium/CFRP hybrid beam under impact loading.* International Journal of Crashworthiness, 2016. **22**(2): p. 190-201.

[54] D.K. Shin, H.C. Kim, and J.J. Lee, *Numerical analysis of the damage behavior of an aluminum/CFRP hybrid beam under three point bending.* Composites Part B: Engineering, 2014. **56**: p. 397-407.

[55] T. Ohori, T. Hayashi, and J. Takahashi. *Fea using design optimization technique for an application of carbon fiber reinforced thermoplastics to automobile body structure*. in *The 20th International Conference on Composite Materials*. 2015. Copenhagen, Denmark.

[56] K. Ikeya, M. Shimoda, and J.X. Shi, *Multi-objective free-form optimization for shape and thickness of shell structures with composite materials.* Composite Structures, 2016. **135**: p. 262-275.

[57] J. Bös, *Numerical optimization of the thickness distribution of three-dimensional structures with respect to their structural acoustic properties.* Structural and Multidisciplinary Optimization, 2006. **32**(1): p. 12-30.

[58] D.H. Kim, D.H. Choi, and H.S. Kim, *Design optimization of a carbon fiber reinforced composite automotive lower arm.* Composites Part B: Engineering, 2014. **58**: p. 400-407.

[59] X. Zhu, R. He, X. Lu, X. Ling, L. Zhu, and B. Liu, *A optimization technique for the composite strut using genetic algorithms.* Materials & Design 2015. **65**: p. 482-488.

[60] J.G. Cho, J.S. Koo, and H.S. Jung, *A lightweight design approach for an EMU carbody using a material selection method and size optimization.* Journal of Mechanical Science and Technology, 2016. **30**(2): p. 673-681.

[61] X. Cui, S. Wang, and S.J. Hu, *A method for optimal design of automotive body assembly using multi-material construction.* Materials & Design, 2008. **29**(2): p. 381-387.

[62] M.N. Velea, P. Wennhage, and D. Zenkert, *Multi-objective optimisation of vehicle bodies made of FRP sandwich structures.* Composite Structures, 2014. **111**: p. 75-84.

[63] M. Kalantari, C. Dong, and I.J. Davies, *Multi-objective analysis for optimal and robust design of unidirectional glass/carbon fibre reinforced hybrid epoxy composites under flexural loading.* Composites Part B: Engineering, 2016. **84**: p. 130-139.

[64] M. Kalantari, C. Dong, and I.J. Davies, *Multi-objective robust optimisation of unidirectional carbon/glass fibre reinforced hybrid composites under flexural loading.* Composite Structures, 2016. **138**: p. 264-275.

[65] L. Burns, A. Mouritz, D. Pook, and S. Feih, *Strengthening of composite T-joints using novel ply design approaches.* Composites Part B: Engineering, 2016. **88**: p. 73-84.

[66] F.R.S. da Cunha, T. Wille, R. Degenhardt, M. Sinapius, F.C. de Araujo, and R. Zimmermann, *A robustness-based design strategy for composite structures.* Aircraft Engineering and Aerospace Technology, 2014. **86**(4): p. 274-U36.

[67] H.K. Ibrahim, *Design optimization of vehicle structures for crashworthiness improvement*. 2009, Concordia University

[68] F.X. Irisarri, F. Laurin, F.H. Leroy, and J.F. Maire, *Computational strategy for multiobjective optimization of composite stiffened panels.* Composite Structures, 2011. **93**(3): p. 1158-1167.

[69] L.P. Chaves and J. Cunha, *Design of carbon fiber reinforcement of concrete slabs using topology optimization.* Construction and Building Materials, 2014. **73**: p. 688-698.

[70] A.R. Rishikesh and G. Nandakumar, *Design optimization and analysis of fiber reinforced composite cylindrical shell structure.* International Journal of Engineering Research & Technology, 2014. **3**(10).

[71] Y. Mo, D. Ge, and B. He, *Experiment and optimization of the hat-stringer-stiffened composite panels under axial compression.* Composites Part B: Engineering, 2016. **84**: p. 285-293.

[72] R.H. Lopez, M.A. Luersen, and E.S. Cursi, *Optimization of laminated composites considering different failure criteria.* Composites Part B: Engineering, 2009. **40**(8): p. 731-740.

[73] J. Takahashi and T. Ishikawa. *Next challenge in CFRTP for mass production automotive application*. in *35th SAMPE Europe International Technical Conference & Forum (SEICO 14)*. 2014. Paris, France.

[74] J. Takahashi and T. Ishikawa. *Current japanese activity in CFRTP for automotive application*. in *13th Japanese-European Symposium on Composite Materials*. 2013. Nantes, France.

[75] J. Takahashi and T. Ishikawa. *Current japanese activity in CFRTP for industrial application*. in *Composite Week @ Leuven and TexComp-11 Conference*. 2013. Leuven, Belgium.

[76] Y. Wan and J. Takahashi, *Tensile properties and aspect ratio simulation of transversely isotropic discontinuous carbon fiber reinforced thermoplastics.* Composites Science and Technology, 2016. **137**: p. 167-176.

[77] Y. Nakashima, S. Yamashita, X. Zhang, H. Suganuma, and J. Takahashi, *Analytical modelling of the behaviour and scatter of the flexural modulus of randomly oriented carbon fibre strand thermoplastic composites.* Composite Structures, 2017. **178**: p. 217-224.

[78] Y. Wan and J. Takahashi. *Effect of tape lengths and impregnation conditions on mechanical properties of carbon fiber tape reinforced thermoplastics*. in *Proceedings of 12th International Conference on Textile Composites*. 2015.

[79] Y. Wan, T. Goto, T. Matsuo, J. Takahashi, and I. Ohsawa. *Investigation about fracture mode and strength in curved section of carbon fiber reinforced polypropylene*. in *19th international conference on composite materials*. 2013.

[80] S. Yamashita, K. Hashimoto, H. Suganuma, and J. Takahashi, *Experimental characterization of the tensile failure mode of ultra-thin chopped carbon fiber tape-reinforced thermoplastics.* Journal of Reinforced Plastics and Composites, 2016. **35**(18): p. 1342-1352.

[81] S. Yamashita, Y. Nakashima, J. Takahashi, K. Kawabe, and T. Murakami, *Volume resistivity of ultra-thin chopped carbon fiber tape reinforced thermoplastics.* Composites Part A: Applied Science and Manufacturing, 2016. **90**: p. 598-605.

[82] H. Suganuma, S. Yamashita, X. Zhang, K. Hashimoto, I. Ohsawa, and J. Takahashi. *Influence of dispersion method to dispersibility and mechanical properties of ultra-thin*

carbon fiber tape reinforced thermoplastics. in *20th international conference on composite materials*. 2015. Copenhagen, Danmark.

[83] M. Akamatsu, T. Matsuo, T. Ohori, X. Zhang, and J. Takahashi. *Finite element simulation of the delamination propagation of L-shaped CFRTP specimen*. in *16th European conference on composite materials*. 2014. Seville, Spain.

[84] M. Akamatsu, T. Ohori, T. Hayashi, and J. Takahashi. *Investigation of the delamination behabior on carbon fiber tape reinforced thermoplastics*. in *20th International Conference on Composite Materials*. 2015. Copenhagen, Danmark.

[85] T. Ohori, T. Matsuo, K. Furukawa, and J. Takahashi. *Finite element analysis of CFRTP hollow beam under flexural load for an application to vehicle body structure*. in *16th European Conference on Composite Materials*. 2014. Seville, Spain.

[86] J.S. Association, *Testing methods for interlaminar fracture toughness of carbon fibre reinforced plastics.* JIS K, 1993. **7086**.

[87] L.A. Carlsson and J.W. Gillespie, *Chapter 4 - Mode-II Interlaminar Fracture of Composites*, in *Composite Materials Series*, K. Friedrich, Editor. 1989, Elsevier. p. 113-157.

[88] A. Turon, P.P. Camanho, J. Costa, and J. Renart, *Accurate simulation of delamination growth under mixed-mode loading using cohesive elements: Definition of interlaminar strengths and elastic stiffness.* Composite Structures, 2010. **92**(8): p. 1857-1864.

[89] K. Allaer, I. De Baere, S. Jacques, W. Van Paepegem, and J. Degrieck. *Experimental assesment of infrared welded bonds using lapshear, double cantilever beam and end notch flexure tests for a carbon fabric reinforced thermoplastic*. in *15th International Conference on Experimental Mechanics*. 2012. Porto, Portugal.

[90] A. Turon, C.G. Dávila, P.P. Camanho, and J. Costa, *An engineering solution for mesh size effects in the simulation of delamination using cohesive zone models.* Engineering Fracture Mechanics, 2007. **74**(10): p. 1665-1682.

[91] D. Simulia, *ABAQUS 6.11 analysis user's manual.* Abaqus, 2011. **6**: p. 22.2.

[92] Z. Fan, M.H. Santare, and S.G. Advani, *Interlaminar shear strength of glass fiber reinforced epoxy composites enhanced with multi-walled carbon nanotubes.* Composites Part A: Applied Science and Manufacturing, 2008. **39**(3): p. 540-554.

[93] K. Tanaka, *Interfacial and interlaminar shear strength of carbon fiber reinforced polycarbonates made with unidirectional sheets: Advances in manufacture and characterisation*. 2015: WIT Transactions on State-of-the-art in Science and Engineering. 131-139.

[94] A. Standard, *D6415/D6415M, 2006. Standard test method for measuring the curved beam strength of a fiber–reinforced polymer–matrix composite. ASTM International, West Conshohocken PA, 2006, DOI: 10.1520/D6415_D6415M*.

[95] J.S. Charrier, F. Laurin, N. Carrere, and S. Mahdi, *Determination of the out-of-plane tensile strength using four-point bending tests on laminated L-angle specimens with different stacking sequences and total thicknesses.* Composites Part A: Applied Science and Manufacturing, 2016. **81**: p. 243-253.

[96] W.C. Jackson and P.G. Ifju, *Through-the-thickness tensile strength of textile composites*, in *Composite Materials: Testing and Design: Twelfth Volume*. 1996, ASTM International.

[97] B. Xiao, Q. Guo, I. Ohsawa, M. Fujita, and J. Takahashi. *Manufacture and performance evaluation of hat-stiffened structure made by chopped carbon fiber tape reinforced thermoplastics*. in *Proceedings of the 18th European Conference on Composite Materials*. 2018. Athens, Greece.

[98] Q. Guo, B. Xiao, I. Ohsawa, M. Fujita, and J. Takahashi. *Numerical analysis and optimization of CFRTP hat-stiffened structure*. in *Proceedings of the 18th European Conference on Composite Materials*. 2018. Athens, Greece.

[99] B. Xiao, *Energy absorption of CFRTP hat-shaped hollow beam under bending load*. 2018, The University of Tokyo.

[100] A. Hyperworks, *Hyperworks 14.0 RADIOSS reference guide.* Altair engineering, 2014.

[101] Z. Hashin, *Failure Criteria for Unidirectional Fiber Composites.* Journal of Applied Mechanics 1980. **47**(2): p. 329-334.

[102] X. Lyu, *Dynamic and viscoelastic behavior of discontinuous carbon fiber reinforced thermoplastics*. 2016, The University of Tokyo.

[103] N.F. Dow and I.J. Gruntfest, *Determination of most needed potentially possible improvements in materials for ballistic and space vehicles.* General Electric Company, Air Force Contract AF, 1960. **4**(647): p. 269.

[104] J.O. Hallquist, *LS-DYNA Keyword User's Manual, Version 971*, in *Livermore Software Technology Corporation*. 2007.

[105] M. Andersson and P. Liedberg, *Crash behavior of composite structure. A CAE benchmarking study*. 2014, Chalmers University of Technology.

[106] P. Chatla, *LS-Dyna for Crashworthiness of Composite Structures*. 2012, University of Cincinnati.

[107] P. Feraboli, B. Wade, F. Deleo, M. Rassaian, M. Higgins, and A. Byar, *LS-DYNA MAT54 modeling of the axial crushing of a composite tape sinusoidal specimen.* Composites Part A: Applied Science and Manufacturing, 2011. **42**(11): p. 1809-1825.

[108] M. Schatz, E. Wehrle, and H. Baier. *Structural design optimization of lightweight structures considering material selection and sizing*. in *The 4th International Conference on Engineering Optimization*. 2014. Lisbon, Portuga.

[109] M. Huber, D. Neufeld, J. Chung, H. Baier, and K. Behdinan, *Data Mining based mutation function for engineering problems with mixed continuous-discrete design variables.* Structural and Multidisciplinary Optimization, 2010. **41**(4): p. 589-604.

[110] O. Exler and K. Schittkowski, *A trust region SQP algorithm for mixed-integer nonlinear programming.* Optimization Letters, 2007. **1**(3): p. 269-280.

List of Publications

(1) Journal Papers

〔Peer-reviewed〕

(1-1) **Qitao Guo** and Yunbo Zhou. "Optimal Design of Pallet Transporter steering linkage with multi-objective decision-making", Mechanical Engineering& Automation, 2014, Vol. 2, No. 2, 40-42.

(1-2) Xianhui Wang, Lei She, **Qitao Guo**, Ran Wei and Yali Zheng. "Multi-objective optimization for new honeycomb sandwich structure on blast-resistant response", Vehicle & Power Technology, 2014, Vol. 4, No. 1, 25-30.

(1-3) Yunbo Zhou, **Qitao Guo**, Lei She, Xianhui Wang and Ran Wei. "Simulation of vehicle cabin protection based on LBE method", Transaction of Beijing Institute of Technology, 2016, Vol. 36, No. 3, 237-241.

(1-4) **Qitao Guo**, Yunbo Zhou, Xianhui Wang, Lei She and Ran Wei. "Numerical simulations and experimental analysis of a vehicle cabin and its occupants subjected to a mine blast", Proceedings of The Institution of Mechanical Engineers Part D: Journal of Automobile Engineering, 2016, Vol. 230, No. 5, 623-631.

〔Peer-reviewed　Under review〕

(1-5) **Qitao Guo**, Isamu Ohsawa and Jun Takahashi. "Experimental and Numerical investigation of Mode I and Mode II interlaminar behavior of ultra-thin chopped carbon fiber tape reinforced thermoplastics", Arabian Journal for Science and Engineering . (Under review)

(1-6) **Qitao Guo**, Isamu Ohsawa and Jun Takahashi. "L-shaped structures made from ultra-thin chopped carbon fiber tape reinforced thermoplastics: delamination behavior and optimization", Advanced Composite Materials. (Need revision)

(2) International Conference Proceeding

〔peer-reviewed　○: Presenter〕

(2-1) ○Ran Wei, Xianhui Wang, Lei She, **Qitao Guo**, Li Wang. "Crashworthiness optimization of a Car Based on FEA Simulation and Experimental Study", Proceedings of the 5th International Conference on Mechanical Engineering and Mechanics, Yangzhou, China, (August 2014).

(2-2) ○**Qitao Guo**, Yunbo Zhou, Lei She, Xianhui Wang, Ran Wei. "Low-speed Collision simulation and analysis of the composite front bumper", Off-road technology branch of SAE-China, Wenzhou, China, (October 2014).

(2-3) ○Lei She, Xianhui Wang, Ran Wei, **Qitao Guo**, Xu Wu. "Research and Simulation on the Air-blast Resistance Performance of Vehicle Tires and Suspension System", Off-road technology branch of SAE-China, Wenzhou, China, (October 2014).

(2-4) ○**Qitao Guo**, Zaoyang Li, Toshiro Ohori and Jun Takahashi. "Design optimization of CFRP rectangular box subjected to arbitrary loadings", 17th European Conference on Composite Materials (ECCM17), Munich, Germany, (June 2016).

(2-5) ○**Qitao Guo**, Bohan Xiao, Ye Zhang, Bijan Spitzlei, Isamu Ohsawa and Jun Takahashi. "Numerical and experimental study of the Mode I interlaminar failure of chopped carbon fiber tape reinforced thermoplastics", 21th International Conference on Composite Materials (ICCM21), Xi'an, China, (August 2017).

(2-6) ○**Qitao Guo**, Isamu Ohsawa and Jun Takahashi. "Design Optimization of CFRTP Hat-shaped hollow beam", 42nd Symposium on Japan Society of Composite Materials (JSCM42), Sendai, Japan, (September 2017).

(2-7) ○**Qitao Guo**, Bohan Xiao, Isamu Ohsawa, Michinobu Fujita and Jun Takahashi. "Numerical analysis and optimization of CFRTP hat-shaped hollow beam", 18th European Conference on Composite Materials (ECCM18), Athens, Greece, (June 2018).

(2-8) ○Bohan Xiao, **Qitao Guo**, Isamu Ohsawa, Michinobu Fujita and Jun Takahashi. "Manufacture and performance evaluation of hat-shaped hollow beam made by chopped carbon fiber tape reinforced thermoplastics", 18th European Conference on Composite Materials (ECCM18), Athens, Greece, (June 2018).

(3) Awards

(3-1)「Outstanding Bridge Award(Second Prize)」,「Best Stiffness Award」. Student Bridge Contest of 14th Japan International SAMPE Symposium & Exhibition (JISSE-14), Kanazawa, Japan, (December 2015).

Acknowledgements

Part of this study was conducted as Japanese METI project "the Future Pioneering Projects/ Innovative Structural Materials Project" since 2013fy. Authors would like to express sincere appreciation to the project members who have provided valuable information and useful discussions.

First of all, I would like to express the deepest appreciation to my supervisor, Professor Jun Takahashi, who gave me the chance to study at the University of Tokyo. It has been an honor to do researches in Takahashi Laboratory. I appreciate all his continuous contributions of time, ideas, and funding for my researches. Without his guidance and persistent help, this dissertation would not have been possible.

I am also grateful to Dr. Isamu Ohsawa, Dr. Yi Wan, Mr. Michinobu Fujita, Mr. Bohan Xiao and other laboratory members for their patience and support in overcoming numerous obstacles I have been facing through my research. Each of the members has provided me with extensive personal and professional guidance and taught me a great deal about both scientific research and life in general.

I also wish to thank some of my friends. We were not only able to support each other by deliberating over our problems and findings but also happily by talking about things other than just our papers.

Lastly, I owe my loving thanks to my parents, without their support, patience, and understanding not only in these three years but through all my life, it would have been impossible for me to finish this work. Most importantly, I wish to thank my loving wife, Yuan Yuan, who provides unending inspiration and support.

Qitao Guo

The University of Tokyo

August 2018